

DEVELOPMENT OF A TRUE MULTICOMPONENT
FILM DIFFUSION CONTROLLED MIXED-BED
ION-EXCHANGE MODEL AND
EXPANDED TO INCLUDE
RADIOACTIVE ISOTOPES

By

YI JIA

Bachelor of Science

Tsinghua University

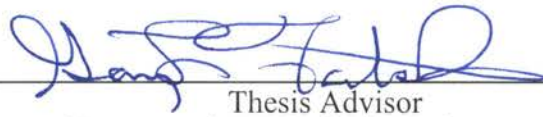
Beijing, China

1998

Submitted to the Faculty of the
Graduate College of the
Oklahoma State University
in partial fulfillment of
the requirements for
the Degree of
DOCTOR OF PHILOSOPHY
December, 2004

DEVELOPMENT OF A TRUE MULTICOMPONENT
FILM DIFFUSION CONTROLLED MIXED-BED
ION-EXCHANGE MODEL AND
EXPANDED TO INCLUDE
RADIOACTIVE ISOTOPES

Dissertation Approved:



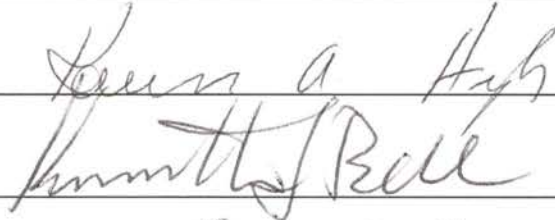
Thesis Advisor



Auel H. Johannes



B



Kenneth Bell



Dean of the Graduate College

Dean of the Graduate College

ACKNOWLEDGMENTS

This work is focused on the applications of mixed bed ion exchange processes in the nuclear and semiconductor industries. To optimize mixed bed ion exchange process requires a better understanding of multicomponent ion exchange dynamics. To achieve this objective, this work proposes a generalized multicomponent mixed-bed ion exchange model that can handle an arbitrary number of species with any valence, especially multivalent dissociative species. Emphasis has been placed on a feasible and stable algorithm for solving the model.

I wish to express my deepest appreciation to my major advisor Dr. Gary L. Foutch for his helpfulness, patience, and flexibility throughout my doctoral programs. His guidance, creativity and insight in ion exchange area have been very valuable for my study. In addition to his technical competence; his character, honor, and integrity have served as a model for me. My sincere appreciation extends to my committee members Dr. Ken Bell, Dr. Arland Johannes, Dr. Karen High, and Dr. Bruce J. Ackerson for their helpful suggestions and insights while serving on my advisory committee.

Particular thanks go to Dr. Dennis Hussey for his suggestions and previous work with the mixed-bed ion-exchange model. Special gratitude is extended to our industrial sponsors; most notably Barry Widman of Knoll's Atomic Power Laboratory and Chris Bates of British Energy. Their financial support and enthusiasm for applying the model to their particular applications was invaluable for evaluation.

I would also like to give my special appreciation to my wife, Li Li, for her strong encouragement during times of difficulty, her love, and understanding throughout all my life with her. Thanks also go to my parents and brother for their support and encouragement.

Financial assistance from the School of Chemical Engineering, the members of the Ultrapure Water Consortium, and the Electrical Power Research Institute is greatly appreciated.

The assistance and advice of the faculty and staff of the School of Chemical Engineering is also gratefully appreciated.

TABLE OF CONTENTS

| Chapter | Page |
|---|------|
| I. INTRODUCTION | 1 |
| Background of This Study | 1 |
| Ultrapure water | |
| Mixed-Bed Ion Exchange | 1 |
| Mixed-bed ion exchange in ultrapure water applications | 3 |
| Scope and Objectives | 10 |
| II. LITERATURE REVIEW | 13 |
| Introduction | 13 |
| Literature review | 13 |
| Strong electrolyte ion exchange modeling | 13 |
| Weak electrolyte ion exchange modeling | 15 |
| Multi-component MBIE modeling | 17 |
| Model Equations | 19 |
| Summary | 25 |
| III. NUMERICAL INTEGRATION OF THE MIXED-BED ION EXCHANGE MODEL | 26 |
| Introduction | 26 |
| Dimensionless variable definitions | 26 |
| Integration limits and increments | 34 |
| Single time-distance node calculation | 35 |
| Solve interfacial concentration separately from ion flux | 36 |
| Solve interfacial concentration with ion flux simultaneously | 40 |
| Numerical method | 43 |
| Programming environment | 46 |
| IV. RESULTS AND VALIDATION | 48 |
| Introduction | 48 |
| Model criteria validation | 48 |
| Parametric analysis to stability and effectiveness of the model | 59 |
| Surry NPS Condensate Polishers Bed Simulation case | 64 |
| KAPL Multi column operation | 79 |

| Chapter | Page |
|--|------|
| V. THE ADDITION OF RADIOACTIVE SPECIES | 84 |
| Introduction | 84 |
| Model equations | 85 |
| Results and validation | 86 |
| Conclusion | 92 |
| VI. CONCLUSIONS AND RECOMMENDATIONS | 93 |
| Conclusions | 93 |
| Recommendations | 95 |
| Future work | 96 |
| APPENDIX A. EQUILIBRIUM RELATIONSHIPS | 103 |
| APPENDIX B. THE EFFLUENT CONCENTRATION PROFILES | 110 |
| APPENDIX C. COLUMN MATERIAL BALANCE | 130 |
| APPENDIX D. APPROXIMATION OF TWO-BED APPROXIMATION OF AN UNEVEN RESIN BED | 138 |
| APPENDIX E. FLUX EXPRESSIONS AND PARTICLE RATE | 140 |

LIST OF FIGURES

| Figure | Page |
|---|------|
| Figure I-1 Skeleton schematic of a BWR nuclear power plant | 6 |
| Figure I-2 Skeleton schematic for a Pressurized Water Reactor nuclear power plant | 7 |
| Figure I-1 Simplified configuration for a semiconductor UPW system | 10 |
| Figure III-1 Flowchart for ionic flux calculation | 36 |
| Figure III-2 Flowchart for solving the interfacial concentration separately | 39 |
| Figure III-3 Flowchart for Solve interfacial concentration with ion flux simultaneously | 43 |
| Figure IV-1. Mass balance error as related to distance step-size (time step-size at 0.01) | 50 |
| Figure IV-2. Mass balance error as related to time step-size (distance step-size at 0.01) | 50 |
| Figure IV-3 Cations effluent profiles for KAPL Lithium column | 53 |
| Figure IV-4. A BWR strong cation effluent history | 55 |
| Figure IV-5. A BWR carbonate effluent history | 55 |
| Figure IV-6, Lithium loading surface for KAPL Lithium column | 57 |
| Figure IV-7 Lithium exchange rate surface. | 57 |
| Figure IV-8 Lithium solution ratio surface. | 58 |
| Figure IV-9 A Lithium Cation breakthrough profile with different time and distance steps | 61 |
| Figure IV-10 Type I Weak Cation breakthrough for Surry A column | 68 |

| Figure | Page |
|--|------|
| Figure IV-11 Cation loading profile for Surry A at a 1 ppb ETA end point if no additional ETA adsorption occurred. | 70 |
| Figure IV-12 Cation loading profile for Surry A at a 1 ppb ETA endpoint (30% adsorption). | 71 |
| Figure IV-13 Type I weak cation (ETA and ammonia) breakthrough history for Surry A column with 30% ETA adsorption | 72 |
| Figure IV-14 Initial effect on Surry column | 76 |
| Figure IV-15 Resin surface several days after the stage in Figure IV-14 | 76 |
| Figure IV-16 Two column approximation diagram of the Surry ion exchange column | 77 |
| Figure IV-17 Strong cation effluent profile for KAPL Multi-column | 81 |
| Figure IV-18 Ammonia effluent profile for KAPL Multi-column | 81 |
| Figure IV-19 Strong cation ions profiles for KAPL Multi-column after 180 days. | 82 |
| Figure V-1 Na-24 with influent concentration of 0.8ppb after 1 day | 88 |
| Figure V-2 Na-24 with influent concentration of 0.8ppb after 2 days | 89 |
| Figure V-3 Na-24 with influent concentration of 0.8ppb after 3 days | 89 |
| Figure V-4 Co-59 (stable) and Ni-58 (stable) loading profiles | 91 |
| Figure V-5 Co-59 (stable) and Co-58 loading profiles | 91 |
| Figure V-6 Co-59 (stable) and Co-60 (Y axis use logarithmic scale) loading profiles | 92 |

NOMENCLATURE

| | |
|----------|--|
| a_s | Specific surface area of resin bead (m^2/m^3), $a_s d_p = 6$ for spherical particles |
| A_i | Calculated parameter in Franzreb's expressions |
| B_i | Calculated parameter in Franzreb's expressions |
| C_i^f | Feed concentration of species i (eq/L) |
| C_T^f | Total ionic concentration in the feed (eq/mL) |
| C_T | Total ionic concentration of the solution (eq/L) |
| C_i^T | Total constituent solution concentration for species 'i' (mol/L) |
| C_H | Hydrogen ion concentration (eq/L) |
| C_{OH} | Hydroxyl ion concentration (eq/L) |
| C_i^b | Bulk concentration of ionic species 'i' (eq/L) |
| C_i^* | Interfacial solution concentration of ionic species 'i' (eq/L) |
| C_i^* | Interfacial solution concentration of ionic species 'i' (eq/L) |
| C_i^m | Solution concentration of molecular species 'i' (mol/L) |
| C_T^* | Total interfacial concentration (eq/L) |
| C_T^b | Total bulk ionic concentration (eq/L) |

| | |
|------------------|---|
| $d_{p,i}$ | Resin bead diameter for constituent 'i' (cm) |
| D_i | Diffusivity of ionic species 'i' (cm^2/s) |
| D_e | Effective diffusivity (cm^2/s) |
| D_i^* | Diffusivity of molecular species (cm^2/s) 'i' |
| F | Faraday's constant (coulombs/mole) |
| FAR | Volume fraction of anion resin |
| FCR | Volume fraction of cation resin |
| H_d | Dimensionless column height |
| J_i^m | Molecular species flux of constituent 'i' ($\text{meq}/(\text{s}\cdot\text{cm}^2)$) |
| K_{H}^i | Selectivity of cation species 'i' with respect to hydrogen |
| k_i | Mass transfer coefficient of constituent 'i' (cm/s) |
| k_e | Effective mass transfer coefficient (cm/s) |
| k_i^m | Mass transfer coefficient of molecular species 'i' (cm/s) |
| k_w | Dissociation constant of water (mol^2/L) |
| L | Bed height (cm) |
| N_S | Number of theoretical slices |
| N_i | $-\frac{z_i}{z_Y}$, ratio of charge to mean coion valence |
| P | Calculated parameter in Franzreb's expressions |
| q_i^T | Total constituent resin concentration for species 'i' (mol/L) |
| q_i^e | Equilibrium capacity of species 'i' (mol/L) |

| | |
|--------------|--|
| q_i^m | Molecular species capacity for constituent 'i' (eq/L) |
| Q_i | Total ion exchange resin capacity, 'i' for cations, 'j' for anions (meq/mL) |
| R | Ideal gas constant (J/mol K) |
| R_i^T | Total exchange rate of constituent 'i' |
| R_B^R | Boron fixation rate |
| Re | Particle Reynolds number |
| r | Film radius (m) |
| Sc | Schmidt number |
| t | Time (s) |
| u | Velocity (cm/s) |
| u_s | Superficial velocity (cm/s) |
| x_i | Ratio of bulk solution concentration to feed concentration of species 'i' C_i/C_i^f |
| X_i | Bulk solution equivalent fraction of ion 'i' C_i/C_T |
| X_i^* | Interfacial equivalent fraction of ionic species 'i' |
| X_i^b | Bulk equivalent fraction of ionic species 'i' |
| y_i | Ratio of bulk solution capacity to equilibrium capacity of constituent 'i' q_i/q_i^e |
| Y_i | Dimensionless equivalent fraction of ionic species 'i' q_i/Q_i |
| Y_i^e | Equilibrium equivalent fraction of ionic species 'i' |
| Y_i^{init} | Initial resin phase equivalent fraction |
| z | Bed depth (cm) |
| z_i | Valence of ionic species 'i' |

Greek letters

| | |
|--------------------------------|---|
| α | Scaling constant $\frac{C_i^f q_r^T}{C_r^f q_i^T}$ |
| δ | Nernst film thickness (cm) |
| ξ_i | Dimensionless distance for constituent 'i' |
| λ_i | Constant for calculating interfacial concentrations |
| ϕ | Electric potential (J/C) |
| τ_i | Dimensionless time for constituent 'i' |
| τ_r | Dimensionless time for reference constituent 'r' |
| Λ | Ionic equivalent conductivity (S L/mol) |
| $\Delta m_i^{\text{solution}}$ | Change in mass of solution (g) |
| $\Delta m_i^{\text{resin}}$ | Change in mass of resin (g) |

CHAPTER I

INTRODUCTION

Mixed-bed ion-exchange (MBIE) is used extensively in ultrapure water (UPW) processing for the simultaneous removal of the cationic and anionic contaminants in microelectronics, power, food and pharmaceutical industries. Optimizing MBIE performance requires accurate models for multi-component ion exchange kinetics. Truly multi-component models must be able to handle any number of ions, including dissociative species.

Background of This Study

Ultrapure water

Ultrapure water is typically defined as water with dissolved impurity concentrations less than 1 part per billion (ppb, or $\mu\text{g/L}$) with correspondingly low levels of particulate and microbial contaminants (Sadler, 1993), although this definition is relaxed for dissolved oxygen and nitrogen. It also can be defined as water with conductivity less than $0.1 \mu\text{S/cm}$. Ultrapure water is widely used in industries like the pharmaceutical, biotechnological, environmental, nuclear power and semiconductors. For instance, ultrapure water is used as a special chemical in pharmaceutical and biotechnological processes, rinse water in microchip manufacturing, and make-up and condensate polishing water in nuclear power generators.

Mixed-Bed Ion Exchange

Kunin and McGarvey (1951) developed the concept of mixed bed ion exchange (MBIE). Mixed-bed ion exchange is used when highly pure water is desired (Bungay, 1989). A MBIE bed mixes certain ratios of cationic and anionic resins in the same column. By doing this the ionic impurities in water can be reduced simultaneously to very low concentrations (with a conductivity of less than 0.2 $\mu\text{S}/\text{cm}$), and the dissolved silica can also be removed to less than 2 ppb (Arden, 1968).

The mechanism of MBIE is illustrated in these reactions.



The cationic resin in the column offers hydrogen ions (H^+) to exchange with other cations in water, while the anionic resin provides hydroxide ions (OH^-) to exchange with anions. Then the liberated hydrogen and hydroxide ions neutralize in bulk phase. The neutralization reaction decreases the amount of hydrogen and hydroxide ions in the bulk phase, and thus helps the kinetics of the exchange reaction.

A MBIE column can be operated in different cycles, depending on the process objectives. The two common cycles often used in the power industry are the hydrogen cycle (HOH cycle) and amine cycle. In hydrogen cycle, the cationic resin is in the hydrogen form while the anionic resin is in the hydroxyl form. After exchange, the excess hydrogen and hydroxide are consumed by the water equilibrium reaction. For amine cycle, the operation is realized either by adding amines to the feed water or using the

cationic resin in the amine form. Amine cycle is used for corrosion reduction in the condensate polisher, since it results in alkaline effluent water pH. Besides being operated in different cycles, mixed-bed columns can also be operated in series or in combination with other desalination apparatus to achieve the water processing goals.

Mixed beds are used in nuclear power plants to remove ionic contaminants that may potentially corrode the steam generator. The contaminant sources are typically metal oxides from corrosion of the materials of construction and condenser water from condenser tube leakage. The advantages of pure water are two-fold: the absence of any component in an electrochemical reaction prevents the reaction from occurring, and a low conductivity inhibits corrosion reactions by inhibiting the flow of electrons.

Although MBIE is efficient in deionization, it has one drawback – difficult to regenerate. The regeneration of mixed bed requires a series of steps, namely, separation of resin particles by backwashing, individual resin regeneration using strong acids or bases, and remixing of resins by air. Since complete separation of cationic and anionic resins is difficult, the cross contamination of resins during regeneration is inevitable.

Overall, mixed-bed ion exchange has the following major characteristics:

- small space requirements (combining cationic and anionic beds in one unit);
- low operating costs due to smaller amounts of regenerant and water;
(Applebaum, 1968)
- a higher discharge rate of ultrapure water;
- constant readiness for operation;
- a low initial investment; and
- difficulty of regeneration (Arden, 1968)

Mixed-bed ion exchange in ultrapure water applications

Ultrapure water has been widely used in industries. The major applications are used in the electrical power, semiconductor manufacturing, and pharmaceutical industries. The following part describes the functions of ultrapure water in these industries.

Electrical power

Steam cycle water chemistry is critical to the sustained operation of nuclear and fossil-fired power plants. Ultrapure water processing occurs in three major areas of the plant: make-up water production, condensate polishing, and reactor water clean-up. Each of these applications has specific requirements for water quality and uses different technologies to achieve these requirements.

The nuclear industry is far more interested in the production of ultrapure water than fossil-fired electrical generation plants due to the high replacement cost of a nuclear steam generator (exceed 250 million dollars) (Bates, 1999). Many fossil plants had been constructed before a clear economic advantage in favor of condensate polishing for standard electrical power plants, but a recent analysis by the Electrical Power Research Institute (EPRI) has shown the benefits of condensate polishing for fossil plants.

Nuclear power plants use ultrapure water to minimize erosion and corrosion of materials within the steam power cycle. The erosion and corrosion of the materials of construction depend primarily upon the temperature, pH and contaminants present in the water. The Electrical Power Research Institute (EPRI) suggested maximum contaminant concentrations for each steam cycle configuration. The water chemistry is determined by the steam cycle configuration. Two steam cycle configurations are predominant in the

nuclear power plants, the Boiling Water Reactor (BWR) and the Pressurized Water Reactor (PWR).

As shown in Figure I-1, water is circulated through the Reactor Core picking up heat as the water moves past the fuel assemblies. The water eventually is heated enough to convert to steam. Steam separators in the upper part of the reactor remove water from the steam. The steam cycle water is very close to ultrapure, occasionally hydrogen is added to prevent water radiolysis, and also very low levels of zinc may be added to suppress the formation of radioactive Co^{60} on metal surfaces in the reactor. The steam, after passing through the turbines, then condenses in the condenser, which is at a vacuum and is cooled by ocean, sea, lake, or river water. The condensate is then passed through condensate polishers to remove any contaminants that may have been introduced into the steam cycle.

The primary source of contaminants in a BWR plant is the condenser cooling water. The condenser tubes occasionally leak cooling water into the steam cycle, which induces corrosion in the circuit. The greatest concern is the water quality in the reactor, where the contaminants are concentrated to about 100 times the influent value.

For example, a boiler influent concentration of 200 parts per trillion (ppt) sulfate concentrates to 20 ppb sulfate, a significant concentration that can induce corrosion of iron, cobalt and nickel. The major concern is the local concentration of contaminants on the boiling nucleation sites in the reactor core; contaminants concentrate to even higher levels in the pits and scratches and induce pit corrosion.

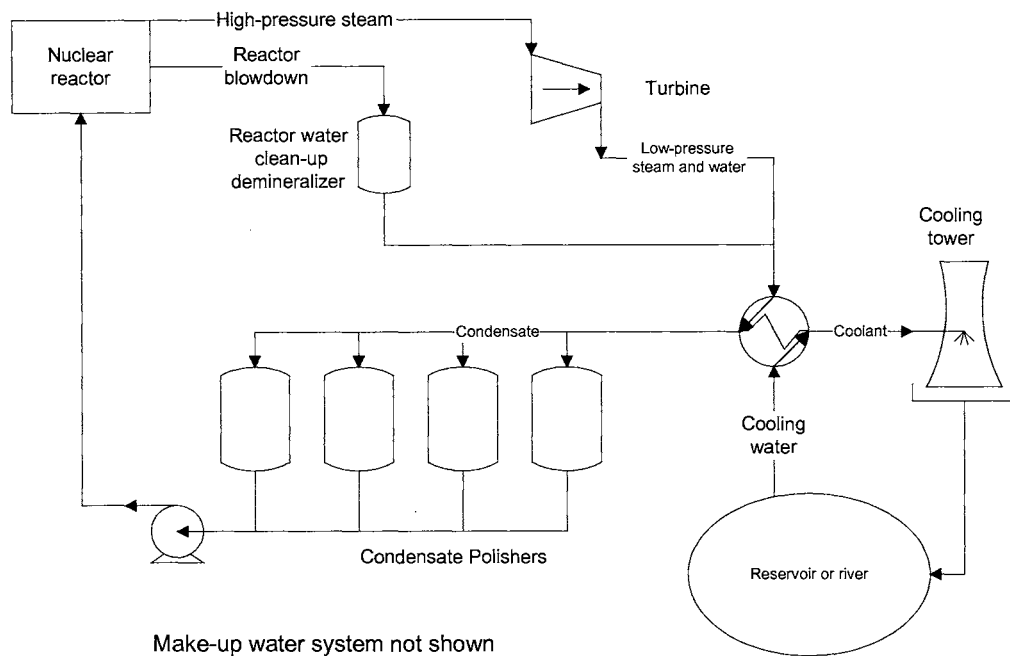


Figure I-1 Skeleton schematic of a BWR nuclear power plant

The reactor blowdown (concentrated water) is typically treated with a mixed-bed demineralizer to prevent excessive concentration in the reactor core, after which it is re-introduced into the steam cycle.

As shown in Figure I-2, the Pressurized Water Reactor (PWR) has 3 separate cooling systems. Only 1 is expected to have radioactivity - the Reactor Coolant System. The primary loop is at very high pressure, approximately 2500 psig, and this maintains the water in its liquid phase as it contacts the reactor. The heated water is passed through a steam generator where it boils the secondary loop water. The secondary steam expands through the turbines where it is condensed and polished in a manner similar to BWR plants. Notice a steam generator blowdown demineralizer is also used after the steam generator.

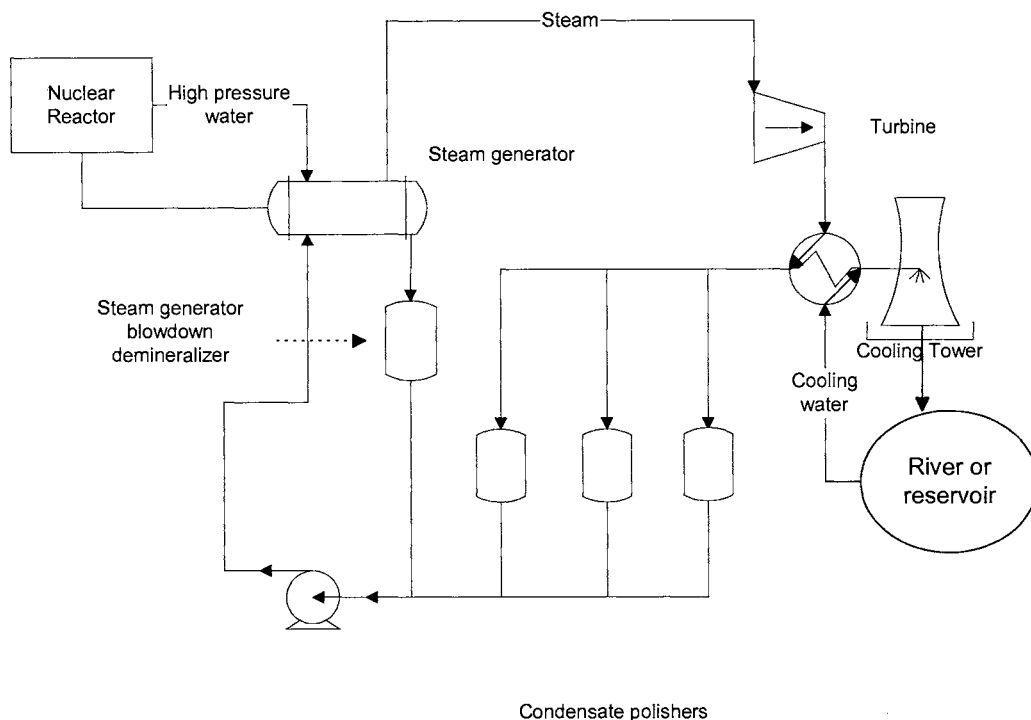


Figure I-2 Skeleton schematic for a Pressurized Water Reactor nuclear power plant

PWR plants generally do not use ultrapure water in either the primary or secondary cycles. The secondary cycle generally has an amine such as ammonia, ethanolamine or hydrazine added to the system directly after the condensate polishers to raise the pH to approximately 9.0. The addition of the amine reduces the hydrogen concentration according to weak base dissociation chemistry, which reduces the corrosion potential between hydrogen ions and the metals of construction.

The condenser is maintained at a vacuum using either vacuum pumps or air ejectors. Cooling of the steam is provided by condenser cooling water pumped through the condenser by circulating water pumps, which take suction from water supplied from the ocean, sea, lake, river, or cooling tower.

Semiconductor manufacturing

Semiconductor chips are manufactured using a complex procedure that chemically imprints a small, rectangular transistor pattern on a circular disk, or wafer. The wafer is typically 150 to 200 mm (6 to 8 inches) in diameter, although 300 mm (12-inch) wafers are currently in development. After processing, the wafer is cut into rectangular 'chips,' which are placed in a housing for attachment of pin-out connections to the silicon. Although the assembly of the chip requires some rinse water, wafer manufacturing consumes much larger quantities of ultrapure water.

The transistors are applied to the silicon wafer using a combination of film deposition, lithography, ion implantation and chemical etching in a sequence that may contain more than 100 steps. During many of these steps, chemicals or residuals are rinsed from the wafer with ultrapure water. Ultrapure water is used in many processing steps, but the major consumer is chemical etching, where acids are washed from the wafer.

Since 1985, the number of transistors on processors has doubled nearly every 18 months. This increase is accomplished, in part, by reducing the transistor line width (or size) from more than 1.0 micron to less than 0.2 microns. As the line width decreases, water purity requirements increase to reduce electrical shorting or physical destruction of the transistors during rinsing.

The water quality standards in the semiconductor industry are far more severe than nuclear applications, and several more units are required to remove all of the contaminants before the water is used for process applications. Figure I-3 is a sample

schematic for a typical semiconductor ultrapure water system, although the configuration is by no means standard.

The system is composed of a make-up water system, a primary ultrapure water loop, and a polish ultrapure water loop. The water quality improves for each sub-system. The make-up loop water typically rejects or adsorbs 99% of the ionic and organic contaminants removed from the source water. The primary loop usually has 18+ MΩ-cm water (the theoretical maximum resistivity of water is 18.25 MΩ-cm at 25 °C), but the water still contains trace amounts of organic chemicals and particles. The polish loop must maintain factory specifications at all times, the contaminant limits are determined by the process but are usually in the single part per trillion range for ionic contaminants, and less than 1 ppb for organic chemicals. Dissolved gas concentrations vary according to the process; some of the processes have no dissolved oxygen constraints, while some processes require less than 1 ppb.

The make-up system is designed to maintain the level of the reverse osmosis product storage tank, while the primary loop is designed to maintain the level of the ultrapure water storage tank.

Pharmaceutical Applications

The primary pharmaceutical applications for ultrapure water processing are Water for Injection (WFI) and manufacturing of medicines. The separation requirements for pharmaceuticals are aimed at eliminating pyrogens (low molecular weight organic molecules – typical of microbial membrane decay) that can cause fevers. In addition,

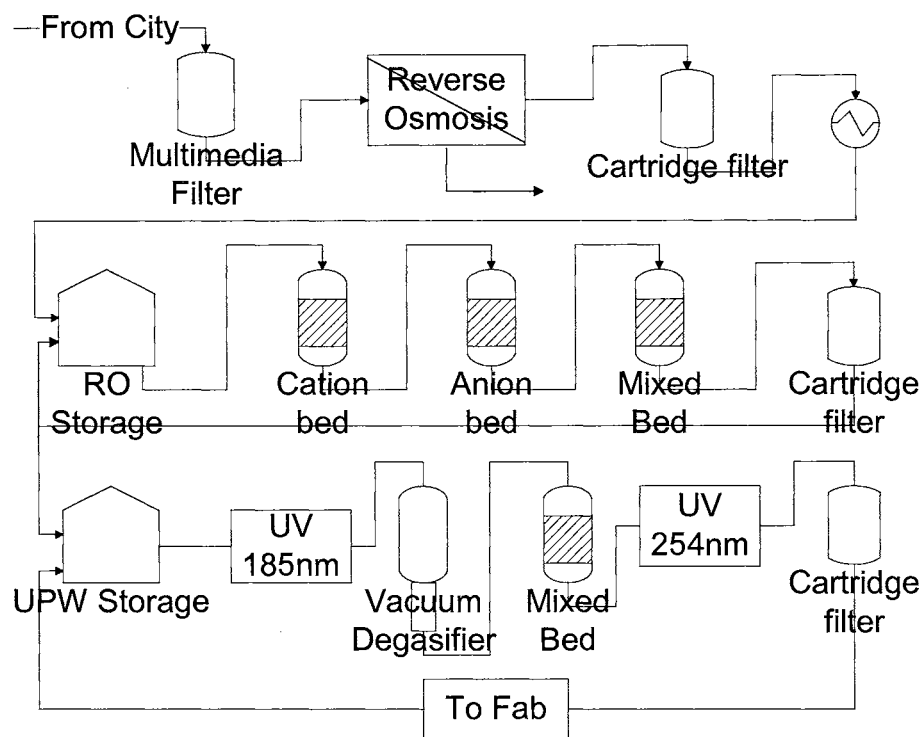


Figure I-3 Simplified configuration for a semiconductor UPW system (Hussey, 2000)

ultrapure water is used extensively as a diluent for dialysis. Patients with kidney failure must undergo dialysis two to three times per week. Waste products in the blood, such as urea, diffuse through hollow fiber membranes into ultrapure water. Cases have been reported where ultrapure water systems have failed, and fluoride is introduced into patients' blood streams, with disastrous results.

The United States Pharmacopoeia (U.S.P.) determines the water purity requirements for the United States pharmaceutical industry. The purity requirements are typically less stringent than those for the semiconductor industry, with exception to microbial contaminants and pyrogens.

Scope and Objectives

This work proposes a generalized multicomponent mixed-bed ion exchange model that can handle an arbitrary number of species with any valence, especially multivalent dissociative species. Primary objectives will be focused on a stable and effective solving strategy. The model intends to have the following attributes, many of which were developed in theory by Sunkavalli (1996), Liu (1998) and Hussey (2000).

- Modeling multicomponent systems to handle an arbitrary number of species (eight strong base cations, eight strong base anions, five single-step dissociative monovalent weak bases, five single step dissociative monovalent weak acids, one each of a two-step dissociative base and acid and one each of a three-step dissociative base and acid so far).
- Strong electrolyte ion exchange with mass transfer rates calculated by an approximation of the Nernst-Planck ionic flux integrated across a thin film.
- Model weak electrolyte ion exchange with mass transfer rates calculated by either Nernst-Planck film diffusion only, or a combination of Nernst-Planck and Fickian film diffusion if possible.
- Maintain solution phase bulk neutralization for complex ionic species and resin/solution reaction equilibrium for ionic species throughout the duration of the simulation.
- Develop new solving strategy and algorithm to improve the stability and effectiveness of the model.
- Predict the effects of fouling on the effluent quality and bed performance for both the cation or anion resins; Predict the effects of cation resin desulfonation on the effluent

water quality; Predict the effects of resin heels, or layers of cation or anion resin at the top or the bottom of the mixed bed.

- Predict radioactive isotopes distribution in mixed bed.

This chapter has introduced ultrapure water, mixed bed ion exchange, ultrapure water applications in industry and the objectives of this work.

In Chapter 2, a literature review including the history of the modeling efforts of the ultrapure water research group at Oklahoma State University is presented; the development of the analytical model algorithm is discussed. Chapter 3 discusses the numerical solving strategies and algorithm of the analytical model. Chapter 4 presents results and validation of the model. Chapter 5 presents the addition of radioactive isotopes to MBIE model. Chapter 6 offers some conclusions and recommendations for future work in mixed bed ion exchange modeling.

CHAPTER II

LITERATURE REVIEW

Introduction

MBIE (mixed bed ion exchange) has been widely used in water deionization for several decades, especially for the production of ultra-pure water in the nuclear, pharmaceutical, paper and semiconductor industries. To optimize the MBIE process requires better models and understanding of multicomponent ion exchange kinetics. Two theories can describe multicomponent ion exchange, equilibrium and rate. Equilibrium theory assumes that a local equilibrium exists between the resin and bulk phases and that mass transfer resistance between phases or within the resin beads is negligible. Local equilibrium is not accurate at extremely low concentrations or at high flow rates. Rate theory, which is based on the rate of ionic diffusion to the exchange site, is more appropriate at these low concentrations. In this work, MBIE model is based on rate theory.

Literature review

Strong electrolyte ion exchange modeling

Caddell and Moison (1954) first conducted a theoretical study of MBIE. They investigated the variables that influence the breakthrough of mixed-bed, and developed

an empirical relationship between leakage and capacity. Kunin (1960) further conducted an experimental study on the kinetics of mixed-bed deionization. They investigated the effects of influent concentration, flow rate, bed depth, and temperature on bed performance and concluded that the ion exchange rate was controlled by a liquid-film mass transfer mechanism at low concentrations. This is one of the important assumptions of MBIE model.

Much research has been done on liquid-side mass transfer in binary ion exchange systems. Schlögl and Helfferich (1957) were the first to apply the Nernst-Planck (N-P) equation to describe the fluxes of ionic species. They studied the kinetics of a binary system. Their results show that the electric field, caused by the difference of the diffusivities, has a significant effect on the ion exchange rate.

Kataoka et al. (1987) studied the film-diffusion controlled liquid-side mass transfer in a ternary system. Flux expressions for the ions with equal valences and ions with different valences were developed separately. The numerical solution of their model matched reasonably well with the experimental results. However, the model cannot be used in a system with more than three species.

Haub and Foutch (1984) first modeled rate-limited mixed-bed ion exchange at ultrapure water concentrations. They developed a model for hydrogen cycle MBIE at ultra-low concentrations with the dissociation of water considered. The major advantages of this model were the consideration of separate material balances for each resin and the inclusion of water dissociation effects. The model was limited to only binary monovalent systems such as $\text{Na}^+ - \text{Cl}^-$ at 25 °C.

Divekar et al. (1987) extended Haub and Foutch's model to incorporate

temperature effects. They studied the correlations of physical properties such as diffusivity, viscosity, and dissociation constant as a function of temperature for certain species and implemented it in the model. Unfortunately, the temperature dependence of selectivities was not available due to lack of experimental data.

Zecchini (1990, 1991) extended the above models to simulate a ternary system of monovalent ions with amines. Pondugula (1994) extended the model to divalent ternary systems. Also, the effect of desulfonation of the cation resin on column performance was included in the current OSU MBIE model.

Weak electrolyte ion exchange modeling

The ion exchange of weak electrolytes is different from strong electrolytes because the concentration distributions are pH dependent; therefore the uptake of weak electrolytes into the ion exchange resin depends on the pH of the solution.

Samuelson (1963) studied the ion exchange with weak electrolytes. He treated the sorption of weak electrolytes, especially the molecular form, as nonionic adsorption. Helfferich (1962) also studied the sorption of weak electrolytes. He concluded that the total moles of weak electrolytes adsorbed into resin could exceed the ion-exchange capacity of the resin, which is different from what was observed for strong electrolyte systems.

Jansen et al. (1996b, 1997) studied the effects of pH, solution concentration and dissociation equilibrium on column dynamics of weak electrolyte ion exchange. They found that changing either pH or concentration, while keeping the other variable constant, leads to considerable fluctuations of effluent concentration and pH, respectively. They

thought these phenomena are caused mainly by the uptake of molecular form electrolytes. They concluded that the exchange of counterions and sorption of neutral species are the two major factors determining the ion exchange behavior of weak electrolytes.

Bulusu (1994) extended the OSU model to handle 3 cations and 5 anions with dissociative carbonates. The ionic flux expression developed by Franzreb et al. (1993) was incorporated in the model, which allowed the modeling of arbitrary valence systems. In addition, Bulusu modeled the effects of resin heels. Bulusu's model was the prototype of OSU's multicomponent MBIE model. Sunkavalli (1996) developed a more generalized multicomponent MBIE model based on Bulusu's work. The number of strong electrolytes was expanded to 8 cations and 8 anions, and preliminary attempts to model carbonate were made.

Hussey (1996) extended the mass-action reaction equilibrium expressions to calculate the interfacial solution equivalent fractions for ionic species regardless of the form of the resin. A pseudo-ion concept was introduced as reference to guarantee the solution of the mass action equation system, which was necessary for the stability of calculation of the interfacial concentrations. Now the algorithm was applied in Sunkavalli's (1996) multicomponent model.

Liu (1999) added significant contributions to the OSU multicomponent model, the water chemistry was expanded to include five single-step weak dissociative bases, five single-step weak dissociative acids, one each of a two-step dissociative acid or base, one each of a three-step dissociative acid or base and also included silica exchange. The model trends appeared reasonable except for the effluent concentrations of the weak electrolyte species. The column material balance had errors with respect to both strong

and weak electrolyte mass transfer.

To summarize the above work, no model can handle mixed-bed ion exchange with arbitrary number of dissociative species. In addition, such systems are industrially significant for ultrapure water processing. Therefore, a model that can handle multicomponent mixed-bed ion exchange with arbitrary number of species and arbitrary valency, especially multivalent dissociative species, is required.

Another major problem of current MBIE model is the solving strategy. The current simulator separates the ion flux solving process into two major parts, interfacial concentration and flux-ion. Iteration is used to determine the interfacial concentration. This iteration process is very CPU time consuming. Also it may lead to errors for bed saturation calculations or operation at higher concentrations. Hussey (2000) was aware of this problem. He made an attempt for a case with phosphate using MathCad, but was not successful.

Multi-component MBIE modeling

Equilibrium models assume that local equilibrium exists between the resin and bulk phases, and mass transfer resistance between two phases is neglected. The general solution approach to predict the effluent ionic concentrations is to solve the material balance equations along with the equilibrium relationship for several slices down the column. Rate theory does not assume local equilibrium, but calculates the rate of interfacial mass transfer. These rate expressions are combined with a column material balance and an equilibrium relationship within the bulk water and the resin-liquid interface to predict the effluent concentrations. The rate model includes four parts:

- Equilibrium at solution and resin surface,

- Mass transfer from bulk solution to resin phase,
- Bulk phase neutralization, and
- Column material balance,

Specifically, the Nernst-Planck equation is used to determine the ionic flux since it incorporates electric potential effects (Newman, 1973). Meanwhile, Fick's law is used to describe the flux of nonionic forms for weak electrolytes. The interfacial concentrations, used as boundary conditions in partial differential mass transfer rate equations, are determined from the selectivity expression (for ionic form), or from dissociation equilibrium (for molecular form) separately. To account for the bulk phase neutralization, the dissociation equilibria of weak electrolytes and water dissociation equilibrium are incorporated in the charge balance. Based on these efforts, the effluent concentrations can be determined by solving the column material balance equations along with the rate expressions numerically. The specific model assumptions are:

- Ion exchange is film-diffusion controlled.
- Ion-exchange resins prefer ions with higher valence. Between ions with the same valence, the ion with higher selectivity is preferred.
- Ionic forms of species are exchanged with resin as counterions.
- The transport of nonionic (molecular) forms of species has two mechanisms – protonation to resin exchange site and molecular adsorption within the resin matrix.
- The protonation of nonionic forms is assumed to occur on the exchange-resin site, which consumes some of the ion exchange capacity.

- An additional adsorption mechanism for nonionic organic molecules is included. This is a purely physical adsorption process that does not use ion exchange capacity.
- For weak electrolytes, if the concentrations of the molecular form C_{Mol} is greater than that of the ionic form C_{Ion} , the mass transfer rate of nonionic species is enhanced by a factor (Jansen, 1996) [22], $\text{Log}\left(\frac{D_{Mol} C_{Mol}}{D_{Ion} C_{Ion}}\right)$, so that the actual mass transfer rate is $(1 + \text{Log}\left(\frac{D_{Mol} C_{Mol}}{D_{Ion} C_{Ion}}\right))$, where D_{Mol} and D_{Ion} are the diffusivities of molecular and ionic forms.
- The overall mass transfer rate for weak electrolytes is the addition of both ionic and molecular transfer rates.

Model Equations

Ion exchange is a diffusion process involving charged species. The Nernst-Planck equation is used to describe the ionic diffusion flux, which is

$$J_i = -D_i \left[\frac{\partial C_i}{\partial r} + \frac{Z_i C_i F}{RT} \frac{\partial \phi}{\partial r} \right] \quad (\text{II.1})$$

where the first term denotes the mass transfer rate due to the concentration gradient; the second term represents the effect of the electric potential gradient.

However, for the nonionic (molecular) forms of weak electrolytes, Fick's second law is employed to describe the mass transfer flux

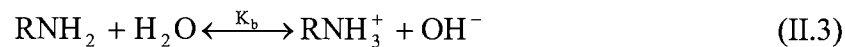
$$J_{Mol} = -D_{Mol} \frac{dC_{Mol}}{dz} \quad (\text{II.2})$$

Dissociation Equilibrium

To generalize the model for multicomponent dissociative systems, three types of common dissociative species have been considered; namely, Type I; Type II; and Type III dissociation species. Their dissociation characteristics are expressed in the following generalized equilibrium equations. We expect that the model should handle any species with similar dissociation chemistry.

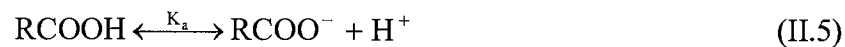
Type I dissociative species -- Monovalent amine (e.g. ammonia) and carboxylic acid (e.g. acetic acid) are typical examples of Type I cationic and anionic species. These species have only one-step dissociation equilibrium, that is,

For monovalent amines



$$K_b = \frac{[\text{RNH}_3^+][\text{OH}^-]}{[\text{RNH}_2]} \quad (\text{II.4})$$

For organic acids



$$K_a = \frac{[\text{RCOO}^-][\text{H}^+]}{[\text{RCOOH}]} \quad (\text{II.6})$$

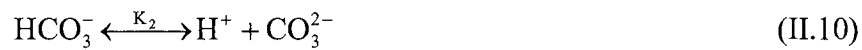
Eq (II.4) and Eq (II.6) have the same form. Therefore, they can be combined into a generalized equation, that is

$$K = \frac{[\text{TypeI_Ion}][\text{Dum_Ion}]}{[\text{TypeI_Mole}]} \quad (\text{II.7})$$

Where, Dum_Ion represents either H^+ or OH^- depending on whether the Type I species is acid or base.

Type II dissociative species -- Type II species have the characteristics of two step dissociation. Diprotic acid – carbonate is an example of Type II dissociative species.

Divalent amines that dissociate in two steps are other examples of Type II dissociative cationic species. The dissociation equilibrium of carbonates can be expressed as



$$K_1 = \frac{[\text{H}^+][\text{HCO}_3^-]}{[\text{H}_2\text{CO}_3]} \quad (\text{II.11})$$

$$K_2 = \frac{[\text{H}^+][\text{CO}_3^{2-}]}{[\text{HCO}_3^-]} \quad (\text{II.12})$$

Hence, the dissociation equilibrium for Type II dissociative species can be generalized by the following dissociation equations

$$K_1 = \frac{[\text{TypeII_MonoIon}][\text{Dum_Ion}]}{[\text{TypeII_Mole}]} \quad (\text{II.13})$$

$$K_2 = \frac{[\text{TypeII_DiIon}][\text{Dum_Ion}]}{[\text{TypeII_MonoIon}]} \quad (\text{II.14})$$

With Eq (II.13) and (II.14) implemented in the computer code, the model can handle any weak electrolytes having the same dissociation equilibrium.

Type III dissociative species -- Type III species have the characteristics of three-step dissociation, which can be described in similar ways as Type II and Type I species.

In general, the dissociation equilibrium of Type III species can be represented by

$$K_1 = \frac{[\text{Dum_Ion}][\text{TypeIII_MonoIon}]}{[\text{TypeIII_Mole}]} \quad (\text{II.15})$$

$$K_2 = \frac{[\text{Dum_Ion}][\text{TypeIII_DiIon}]}{[\text{TypeIII_MonoIon}]} \quad (\text{II.16})$$

$$K_3 = \frac{[\text{Dum_Ion}][\text{TypeIII_TriIon}]}{[\text{TypeIII_DiIon}]} \quad (\text{II.17})$$

By implementing Eq (II.15) through (II.17) into the charge balance equation, any weak electrolytes with Type III dissociation equilibrium should be handled by this model.

Details equation can be found in APPENDIX A.

Interfacial Concentration

Interfacial concentrations for each species are required to calculate the ionic fluxes or the exchange rates. In this model, the interfacial concentrations of ions are determined by ion exchange equilibrium (local equilibrium is assumed at the solid-liquid interface). Specifically, the selectivity expression, which is based on the mass action law, is employed to calculate the interfacial concentrations.

Generally, for the exchange of species A with B, the selectivity is defined as

$$K_A^B = \left(\frac{q_B}{C_B^*} \right)^{Z_A} \left(\frac{C_A^*}{q_A} \right)^{Z_B} \quad (\text{II.18})$$

The above equation can be rewritten in terms of equivalent fractions, total resin capacity and total interfacial concentration as

$$K_A^B = \left(\frac{Y_B}{X_B^*} \right)^{Z_A} \left(\frac{X_A^*}{Y_A} \right)^{Z_B} Q^{(Z_A - Z_B)} C_T^{*(Z_B - Z_A)} \quad (\text{II.19})$$

Generalizing the above equation for any ion i , we have

$$X_i^* = Y_i (K_A^i)^{-1/Z_A} \left(\frac{X_A^*}{Y_A} \right)^{Z_i/Z_A} \left(\frac{Q}{C_T^*} \right)^{1 - Z_i/Z_A} \quad (\text{II.20})$$

In general, for n counterions in the bulk liquid replacing ion A in the resin, we can write n such expressions. However, given the resin loading, resin capacity and total interfacial concentration, we will have $n+1$ unknown interfacial fractions. The extra equation needed to completely specify the system is obtained from a material balance at the solid-film interface (summation relationship), which is

$$\sum_{i=1}^{n+1} X_i^* = 1.0 \quad (\text{II.21})$$

From Eq (II.20), it is evident that for an arbitrary valence case, the ion exchange equilibrium depends on the resin capacity Q and total interfacial concentration C_T^* . Therefore iteration is required to determine the interfacial concentrations. However, before we can determine these individual interfacial concentrations, we need to have an expression for the total interfacial concentration, C_T^* . This is discussed in the following section.

Flux Expression

The flux expression of ions is developed based on the method proposed by Franzreb et al. (1993). The Nernst-Planck equation is the basis of the derivation. The first term on the right hand side of Equation (II.1) is the concentration gradient and the second term is the electric potential. The electric potential term in the Nernst-Planck equation is eliminated using the assumption of no net coion flux in the film. With the introduction of total equivalent concentration, C_T , the electric potential term can be written as

$$\frac{d\phi}{dr} = -\frac{RT}{Z_Y F C_T} \frac{dC_T}{dr} \quad (\text{II.22})$$

where Z_Y is the mean coion valence, which is defined as:

$$Z_Y = \frac{\sum_{j=1}^m Z_j^2 C_j}{\sum_{j=1}^m Z_j C_j} \quad (\text{II.23})$$

Substituting of Eq (II.28) into Eq (II.1) and assuming a pseudo steady state exchange, we have

$$J_i = -D_i \left(\frac{dC_i}{dr} - \frac{C_i Z_i}{C_T Z_Y} \frac{dC_T}{dr} \right) \quad (\text{II.24})$$

After a series of mathematical manipulations, the final form of the flux expression is:

$$J_i = \frac{D_i}{\delta} \left(\left(1 - \frac{N_i}{P} \right) (C_i^* - C_i^0) + N_i A_i \left(1 + \frac{1}{P} \right) (C_T^* - C_T^0) \right) \quad (\text{II.25})$$

where
$$N_i = -\frac{Z_i}{Z_Y} \quad (\text{II.26})$$

$$P = \frac{\sum_{i=1}^n N_i D_i (X_i^* - X_i^0)}{\sum_{i=1}^n D_i (X_i^* - X_i^0)} \quad (\text{II.27})$$

$$C_T^* = \left(\frac{\sum_{i=1}^n (1 + N_i) D_i X_i^0}{\sum_{i=1}^n (1 + N_i) D_i X_i^*} \right)^{\frac{1}{P+1}} C_T^0 \quad (\text{II.28})$$

Mixed bed ion exchange column material balance equations

The mixed bed ion exchange column material balance is developed with theory analogous to adsorption modeling. The fundamental equations of the column material

balance are written below for a single cation species and a single anion species in a cylindrical packed bed assuming no radial or axial dispersion. The subscripts ‘i’ and ‘j’ are used to represent ion/counter-ion systems, for this discussion the subscripts ‘i’ and ‘j’ refer to a cation and anion constituent, respectively.

$$\frac{\partial C_i^T}{\partial t} + \frac{u}{\varepsilon} \frac{\partial C_i^T}{\partial z} + (\text{FCR}) \frac{1-\varepsilon}{\varepsilon} \frac{\partial q_i^T}{\partial t} = 0 \quad (\text{II.29})$$

$$\frac{\partial C_j^T}{\partial t} + \frac{u}{\varepsilon} \frac{\partial C_j^T}{\partial z} + (\text{FAR}) \frac{1-\varepsilon}{\varepsilon} \frac{\partial q_j^T}{\partial t} = 0 \quad (\text{II.30})$$

where C_i^T and C_j^T are the total constituent solution concentrations, and q_i^T and q_j^T are the total constituent resin concentrations. The constants FCR and FAR are the volume fractions of cation resin and anion resin, respectively, allowing the use of the total bed volume for capacity calculations.

The total constituent concentration is a term from Matthias Franzreb (2000) representing the total concentration of a weak electrolyte. The species of a weak electrolyte is defined as the molecular form that is not a protonation/hydrolysis product.

Summary

Since Haub and Foutch (1986a, b) modeled mixed-bed ion-exchange, others have extended the model development. A brief history of modeling efforts of the Ultrapure Water research group at Oklahoma State University was illustrated. Major model equations, which include the dissociation equilibrium, the bulk neutralization of water, reaction equilibrium in resin interfacial, flux expression and column material balance, were presented.

CHAPTER III

NUMERICAL INTEGRATION OF THE MIXED-BED ION EXCHANGE

MODEL

Introduction

This chapter discusses the numerical solving procedure of the analytical equations of the mixed bed column system and discusses the numerical methods and approximations that were required to implement the analytical mathematics into a computer program. Also the dimensionless time-distance node definition and calculation is discussed.

Every calculation has an associated error, and at times the error may propagate throughout the run and significantly affect the results. It is the nature of numerical computing. This requires more attention on numerical method to solve the correct analytical equations. In this chapter, two solving strategies including the related numerical method are presented and discussed.

Dimensionless variable definitions

In order to solve the model numerically, first step should be dimensionless of equations. OSU UPW group has used two definitions of dimensionless variables system. In this work the author uses the dimensionless variables by using ratios instead of solution fractions for constituent mass accounting. The ratios of interest are the solution

concentration of the constituent to the total feed concentration of that species, and the ratio of the resin concentration of the individual species to the final equilibrium loading of the species at the given influent concentration.

The total solution concentration of a constituent species is defined as the following,

$$C_i^T = \sum_{k=1}^n C_{ik} + C_i^* \quad (\text{III.1})$$

where C_{ik} is the concentration of the ionic species of a constituent molecule in mol/l, 'k' is the index of the ionic sub-species, 'n' is the total number of ionic species of a constituent, C_i^* is the molecular species concentration, and C_i^f is the total constituent feed concentration. The total concentration reduces to ionic concentration for a strong electrolyte because 'n' is unity and the molecular concentration is zero.

For weak electrolyte species, the constituent solution ratios are defined as

$$x_i = \frac{\sum_{k=1}^n C_{ik} + C_i^*}{C_i^f} = \frac{C_i^T}{C_i^f} \quad (\text{III.2})$$

Total constituent capacity is the term in resin phase. The total constituent capacity combines the individual ionic capacities of a dissociative species, as well as any molecular species in the resin matrix that does not use exchange capacity. The quantity is required for the material balance and is defined as,

$$q_i^T = \sum_{k=1}^n q_{ik} + q_i^* \quad (\text{III.3})$$

The constituent resin ratios are defined in terms of the total constituent capacity, q_i^T , and the equilibrium constituent capacity q_i^e . The equilibrium constituent capacity is

found by solving the mass-action equilibrium expressions for the resin loadings at a given feed concentration and multiplying the loadings by the total capacity.

$$y_i = \frac{q_i^T}{q_i^e} = \frac{\sum_{k=1}^n q_{ik}}{q_i^e} \quad (\text{III.4})$$

The lowercase ‘x’ and ‘y’ refer to the ratio of the total solution or resin phase concentration of a particular species, and the uppercase ‘X’ and ‘Y’ refer to the equivalent fraction of an ion with respect to the total number of ions in the solution and resin.

The column material balance is now changed into following form based on the constituent solution concentrations and constituent resin capacities.

$$\frac{\partial C_i^T}{\partial t} + \frac{u}{\varepsilon} \frac{\partial C_i^T}{\partial z} + (\text{FCR}) \frac{1-\varepsilon}{\varepsilon} \frac{\partial q_i^T}{\partial t} = 0 \quad (\text{III.5})$$

$$\frac{\partial C_j^T}{\partial t} + \frac{u}{\varepsilon} \frac{\partial C_j^T}{\partial z} + (\text{FAR}) \frac{1-\varepsilon}{\varepsilon} \frac{\partial q_j^T}{\partial t} = 0 \quad (\text{III.6})$$

Then dividing the both sides by $\frac{C_i^T q_i^e}{q_i^e}$ and $\frac{C_j^T q_j^e}{q_j^e}$ yields the following system of

equations with dimensionless concentrations and capacities varying with dimensional time and length.

$$\frac{\partial x_i}{\partial t} + \frac{u}{\varepsilon} \frac{\partial x_i}{\partial z} + (\text{FCR}) \frac{1-\varepsilon}{\varepsilon} \frac{\partial y_i}{\partial t} = 0 \quad (\text{III.7})$$

$$\frac{\partial x_j}{\partial t} + \frac{u}{\varepsilon} \frac{\partial x_j}{\partial z} + (\text{FAR}) \frac{1-\varepsilon}{\varepsilon} \frac{\partial y_j}{\partial t} = 0 \quad (\text{III.8})$$

One of the advantages is that when time approaches infinity; the final value of 'x_i' and 'y_i' provides a defined final value boundary condition for the model. It also helps to speed the numerical integration of the model.

The time and distance variation of the constituent ratio share the common initial conditions, the feed concentration of the constituents, C_i^f and C_j^f. The dimensionless time and distance variables shown below in Equations (III.9) and (III.10) are similar to the variable chosen by Kataoka (1973), but the time variable uses the influent concentration and final equilibrium capacity of the particular species. The dimensionless variables for constituent 'i' are defined below

$$\tau_i = \frac{k_i C_i^f}{q_i^e \varepsilon} \left(t - \frac{z\varepsilon}{u_s} \right) \quad (III.9)$$

$$\xi_i = \frac{k_i (1 - \varepsilon) z}{d_{p,i} u_s} \quad (III.10)$$

By changing the coordinate from time and length to dimensionless time and length and applying the chain rule, the third order differential equations are reduced to second order differential equations. The derivation is presented in Appendix C, resulting in the following equation set for cations and anions.

$$\frac{\partial x_i}{\partial \xi_i} + \text{FCR} \cdot \frac{\partial y_i}{\partial \tau_i} = 0 \quad (III.11)$$

$$\frac{\partial x_j}{\partial \xi_j} + \text{FAR} \cdot \frac{\partial y_j}{\partial \tau_j} = 0 \quad (III.11)$$

For a single species, there is only one species feed concentration and equilibrium capacity, and the dimensionless time and distance variables can be calculated directly to real time and distance by applying the method of separation of variables. However, for

each ionic species to be integrated along the same real time and distance axis, appropriate constants must be applied to scale each constituent to a reference constituent. Selection of the reference constituent may need further study. There may be an optimizing method to select optimum reference constituent which will benefit the calculations. But based on the numerical integration of the equation set shows the species with the largest dimensionless time have the largest rates. The constituent with the largest rate is most likely to over-predict the change in resin capacity ratio as the resin loading nears equilibrium if the time integration increment is too large. So in this work, the constituent with the largest dimensionless time ion is chosen as the reference constituent

Another consideration for using the constituent with the largest τ as the reference is that the dimensionless distance variable is directly related to the dimensionless time variable by means of the mass transfer coefficient, bed length, and fluid velocity. The dimensionless distance is not sensitive to influent concentration and equilibrium capacity.

The derivation of integration variables from $\partial\tau_i$ and $\partial\xi_i$ to the reference constituent integration increments, $\partial\tau_r$ and $\partial\xi_r$, is in Appendix C. The result is the following sets of equations.

$$\frac{\partial x_i}{\partial \xi_r} + \text{FCR} \cdot \frac{C_r^f q_i^e}{C_i^f q_r^e} \frac{\partial y_i}{\partial \tau_r} = 0 \quad (\text{III.13})$$

$$\frac{\partial x_j}{\partial \xi_r} + \text{FAR} \cdot \frac{C_r^f q_j^e}{C_j^f q_r^e} \frac{\partial y_j}{\partial \tau_r} = 0 \quad (\text{III.14})$$

Note Equations (III.13) and (III.14) reduce to Equations (III.11) and (III.12) when constituent 'i' or 'j' is the reference constituent.

The initial conditions for integration are as follows,

$$x_i = 1 \text{ at } t = 0$$

$$y_i = \frac{Y_i^{\text{init}}}{y_i^e} \text{ at } t = 0$$

$$R_i^T = R_i^T (t = 0, z = 0)$$

The term Y_i^{init} is the initial resin phase equivalent loading fraction at $t = 0$ and $z = 0$.

A single element of this partial differential equation set is integrated by applying separation of variables. This technique recognizes that the differentials must equal to a constant at each time and space coordinate. The two differentials are equated by subtracting one term from both sides of the equation. In this case, the constant is directly proportional to the constituent mass transfer rate, R_i^T .

$$\frac{\partial x_i}{\partial \xi_r} = -\text{FCR} \cdot \frac{C_r^f q_i^e}{C_i^f q_r^e} \frac{\partial y_i}{\partial \tau_r} = R_i^T (\tau, \xi) \quad (\text{III.15})$$

Analytical solutions for this differential equation exist when R_i^T is constant, but it is not constant in MBIE systems and the rates vary with time and distance because solution concentrations, pH and resin loadings change. This forces simultaneous numerical integration first in the length direction to calculate the solution ratio profiles, then in the time direction to calculate the changes in the constituent capacity profiles. An algebraic definition of R_i^T is required that varies according to Nernst-Planck and Fickian diffusion principles when equations are varied with distance and time. The column material balance is calculated based on the rate expressions developed for the particular system.

Current rate expressions for ion exchange rate calculations have incorporated the multicomponent ionic flux expressions developed by Franzreb (1993) with temperature dependence, solution chemistry and reaction equilibrium. The effects of molecular species transfer into the resin have also been considered. The development of the exchange rates is discussed in the Appendices.

The mass transfer can be written for an arbitrary dissociative species by combining the ionic and molecular fluxes for integration along the distance. The ionic and molecular fluxes, J_{ik} and J_i^* , are defined as follows. For cations,

$$\frac{\partial x_i}{\partial \xi_r} = R_i^T = \frac{6(\text{FCR})}{C_i^f} \frac{d_{p,r}}{d_{p,i}} \left[\sum_{k=1}^n \left(\frac{J_{ik}}{k_e} \right) \frac{k_e}{k_r} + \frac{J_i^m}{k_r} \right] \quad (\text{III.16})$$

where J_{ik} represents the individual ionic fluxes of constituent 'i,' J_i^m is the molecular flux of species 'i,' and k_e is the effective mass transfer coefficient calculated from the effective diffusivity in the flux expressions.

The solution constituent ratios in Equation (III.16) can be converted to absolute concentrations by multiplying the respective reference values. A separate dissociation equilibrium routine calculates the resulting ionic concentrations. The equations may be integrated by using one of several numerical methods, but for this work, Gear's backward difference method has been shown to be reliable (Zecchini 1991). The procedure is optimal because it requires only one function evaluation of R_i^T per distance increment.

The loading profiles are changed by relating the differential $\partial y_i / \partial \tau_r$ and R_i^T to the loading profile Y_i . Note y_i is the ratio of species 'i' capacity to its equilibrium capacity, while Y_i is the fraction of the total capacity. These quantities are related as

$$Y_i = y_i \frac{q_i^e}{Q_i} = y_i Y_i^e \quad (\text{III.17})$$

Differentiating Equation (III.17) with respect to y_i yields

$$\frac{dY_i}{dy_i} = Y_i^e \quad (\text{III.18})$$

The differential is then used in the chain rule to relate the total rate to the change in resin equivalent fraction as below in Equation (III.19). The details are given in Appendix C, the final form is

$$\frac{dY_i}{d\tau_r} = Y_i^e \frac{C_r^f}{q_r^e} \frac{q_i^e}{C_i^f} R_i^T \quad (\text{III.19})$$

The numerical integration of these differential equations requires dividing the bed length into time-distance nodes. The algorithm requires extending the vector equations to matrix equations, where the concentrations of each time and space node are determined from the previous distance and time slices.

Integration limits and increments

The first step to construct numerical algorithm for the model equation is to define the integration limits and increments. The numerical integration of the equations is accomplished by determining the integration limits τ_{\max} and H_d , dividing the time and distance into a node, and determining the initial conditions and boundary conditions for the solution phase and resin phase.

The number of distance elements is calculated by dividing the dimensionless column height by the distance step-size,

$$N_S = \frac{H_d}{\Delta\xi_r} \quad (\text{III.20})$$

where the dimensionless column height is from

$$H_d = \frac{k_r(1-\varepsilon)L}{u_s d_{p,r}} \quad (\text{III.21})$$

The maximum dimensionless time is usually a user defined parameter. The number of dimensionless time elements is from Equations (III.22) and (III.23).

$$N_T = \frac{\tau_{\max}}{\Delta\tau} \quad (\text{III.22})$$

$$\tau_{\max} = \frac{k_r C_r^f t_{\text{user}}}{d_{p,r} q_r^e} \quad (\text{III.23})$$

Single time-distance node calculation

Two solving strategies for single time-distance node calculation are presented and discussed here. The first is solving interfacial concentration separately from ion flux. The second solves interfacial concentration with ion flux simultaneously. Theoretically, the first solving strategy is an approximate solution for the model. This approach decouples the equilibrium equations from the charge balance on the surface of the resin, as well as from the flux equations. This algorithm solves the flux expressions by iteratively calculating the total interfacial concentration using the equilibrium relationships. The starting point is that the total interfacial concentration equals the bulk interfacial concentration. This strategy works well for initial breakthrough, which dominates most

ultrapure water cases. Also this strategy is more straightforward to program. But the iteration is CPU time consuming. It may lead to errors for bed saturation calculations or operation at higher concentrations such as brackish water softener regeneration.

Solving interfacial concentration separately from ion flux

The total interfacial concentration (C_T^*) and the individual interfacial equivalent fractions (X_i^*) are relevant by Equations (II.20) and (II.28). Thus, an iterative solution has to be used to determine these quantities and subsequently the ionic fluxes.

The solution procedure for ionic fluxes is

1. Assume $C_T^* = C_T^o$.
2. Calculate X_i^* 's using Equations (II.20) and (II.21).
3. Calculate C_T^* using Equation (II.28).
4. If the difference between new and old C_T^* exceeds the chosen tolerance, repeat steps 2 and 3.
5. Calculate the ionic fluxes using Equation (II.25).

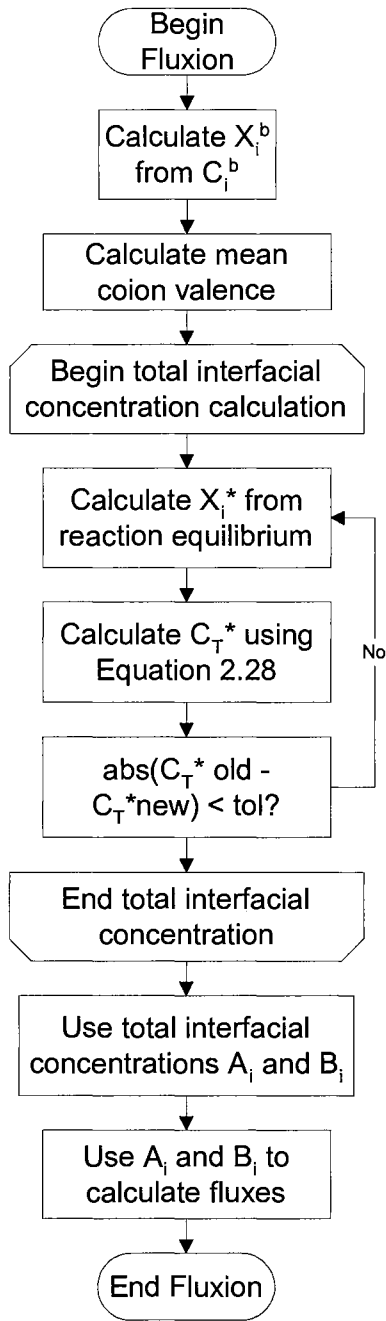


Figure III-1 Flowchart for ionic flux calculation

The overall effective diffusivity defined as:

$$D_e = \frac{\sum_{i=1}^n |J_i \delta|}{\sum_{i=1}^n |C_i^* - C_i^o|} \quad (\text{III.24})$$

The film thickness in Equation (II.24) can be eliminated using the relation

$$\delta = D_e / K \quad (\text{III.25})$$

where K is a mass transfer coefficient calculated from the correlation developed by Dwivedi and Upadhyay (1977) [2], which is

$$\text{Sh} = \text{Sc}^{\frac{1}{3}} \text{Re} \left[\frac{0.765}{(\epsilon \text{Re})^{0.82}} + \frac{0.365}{(\epsilon \text{Re})^{0.386}} \right] \quad (\text{III.26})$$

Alternatively, the mass transfer coefficient can be provided directly from experiments.

Rates calculation

The rate of exchange is related to the flux of species 'i' by

$$\frac{\partial q_i}{\partial t} = -J_i a_s \quad (\text{III.27})$$

where J_i is the flux of species i. For weak electrolytes, J_i is the summation of both ionic and nonionic forms, that is $J_i = J_{\text{Ionic}} + J_{\text{Mol}}$

However, the resin phase concentration q_i can be represented as:

$$q_i = y_i Q \quad (\text{III.28})$$

where y_i is the fraction of resin phase concentration, and Q is the resin capacity.

Substituting Eq (III.28) into Eq (III.27), yields

$$\frac{dy_i}{dt} = \frac{-J_i a_s}{Q} \quad (\text{III.29})$$

The rate at a specific time and distance is found from the following equation.

$$R_i^T = -k_e \left(\frac{J_i^T}{k_e} \right) \left(\frac{6d_{p,r}}{C_i^f k_r d_{p,i}} \right) (FR) \quad (III.30)$$

Therefore, the rate of ions loading into resin can be determined by Eq (III.29). Once the individual ionic fluxes are known, the material balance can be calculated.

After nondimensionalization of the model equation, we get a set of partial differential equations of the form;

$$\frac{\partial x_i}{\partial \xi_r} = -\alpha \frac{\partial y_i}{\partial \tau_r} = R_i^T (\tau_r, \xi_r) \quad (III.31)$$

where α_i is a constant defined by,

$$\alpha_i = (FR) \frac{q_r^e C_i^f}{q_i^e C_r^f} \quad (III.32)$$

With the initial time and space boundary conditions and integration limits, Equation (III.31) can be separated into two ordinary difference equations.

$$\Delta x_i = R_i^T \Delta \xi_r \quad (III.33)$$

$$\Delta y_i = -\frac{R_i^T}{\alpha_i} \Delta \tau_r \quad (III.34)$$

Equations (III.33) and (III.34) can be integrated using ordinary differential equation solvers given the value of the rate is known. The first-order Euler's method and fourth-order Gear's method (Gear, 1971) are chosen to solve the resin and bulk phase fractions in this work.

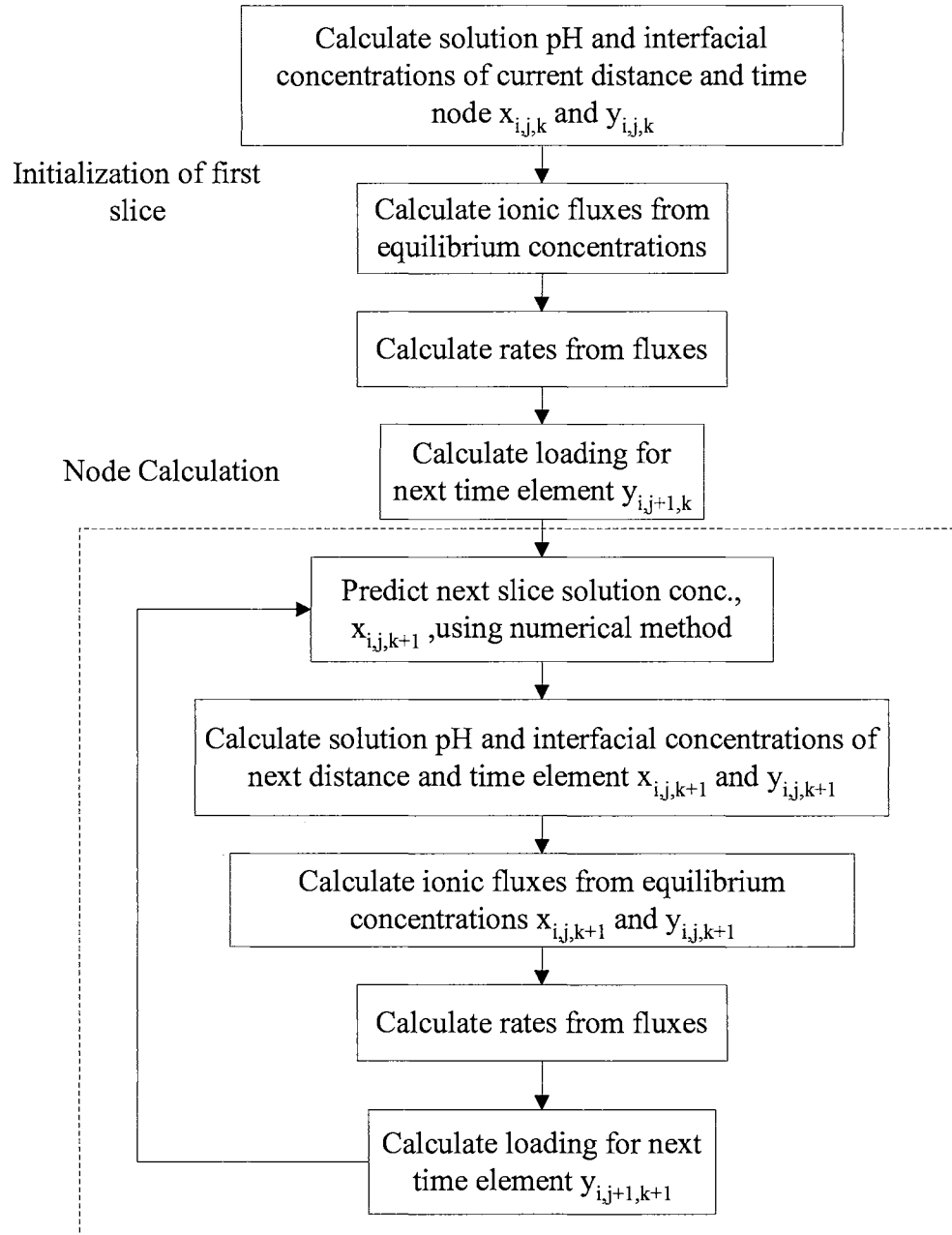


Figure III-2 Flowchart for solving the interfacial concentration separately

Figure III-2 shows a brief flowchart of the node calculation by solving the interfacial concentration separately.

Solve interfacial concentration with ion flux simultaneously

To address this limitation, a second strategy is developed.

The main concept for this alternative strategy is that interfacial concentration, equilibrium equations and flux expressions are solved simultaneously. The solving procedure is:

1. Define the total species from an input file.
2. List all equations and variables, which include equilibrium equations, flux equations, charge balance, water dissociation, and mass balance equations for the weak electrolytes. The variables will be all of the ionic concentrations.
3. Convert variables and equations to a standard form for a multivariable solver. All equilibrium expressions need to be linearized by taking base 10 logarithms. All variables are written in their logarithm form, but these are then used in exponential form in mass balance equations. For example: Assign an X array to all of the variables, i.e. $X(1) = C_{Na}$, $X(2) = C_{Cl}$, etc.; then the original equilibrium equations $K_{ba} = Q_a * C_b / (Q_b * C_a)$ become:
$$f(C_b) = \log_{10}(K_{ba}) - \log_{10}(Q_a) + \log_{10}(C_b) - \log_{10}(Q_b) - \log_{10}(C_a)$$
4. Set all starting values (the initial value for the first step) from results of previous step.
5. Solve the system equations with an appropriate multivariable solver.

There are numerous multivariable solvers available for this system of equations based on different algorithms. Newton's (a built-in algorithm for IMSL libraries) and Simplex methods are considered for this model. Simplex works better for more complex and stiff problems, which is common for multicomponent MBIE model. Alternative multi-variable algorithms may also improve the solution.

Standardize the equations for multivariable solvers

Before we can solve the system of equations, we need to standardize them. Here the equations include: reaction equilibrium equations, flux equations, charge balance, dissociation of water, and the necessary mass balance equations for the weak electrolytes. The variables will be all of the ionic concentrations, loadings are constant.

First of all, every equation needs to be re-arranged, For example: equilibrium expressions in general form:

$$K_A^B = \left(\frac{q_B}{C_B^*} \right)^{Z_A} \left(\frac{C_A^*}{q_A} \right)^{Z_B} \quad (\text{III.35})$$

Or in terms of equivalent fractions

$$K_A^B = \left(\frac{Y_B}{X_B^*} \right)^{Z_A} \left(\frac{X_A^*}{Y_A} \right)^{Z_B} Q^{(Z_A-Z_B)} C_T^{*(Z_B-Z_A)} \quad (\text{III.36})$$

It can be re-written in to:

$$f(X_B^*) = K_A^B - \left(\frac{Y_B}{X_B^*} \right)^{Z_A} \left(\frac{X_A^*}{Y_A} \right)^{Z_B} Q^{(Z_A-Z_B)} C_T^{*(Z_B-Z_A)} \quad (\text{III.37})$$

Now it can be linearized by taking the base 10 logarithm of all terms in the equation. So it becomes:

$$f(X_B^*) = \log(K_A^B) - Z_A (\log(Y_B) - \log(X_B^*)) - Z_B ((\log(X_A^*) - \log(Y_A)) - \log(Q^{(Z_A-Z_B)} C_T^{*(Z_B-Z_A)})) \quad (\text{III.38})$$

After this step, assign an X array to all of the variables and solving all the standardized equations for zero. Note that the result we get here is not in terms of

equivalent fractions or concentration. The variables are in terms of the logarithm, only the exponential of the variables can be used in calculation for mass balance equations. One of the major advantages of this method is that you can use much more starting values for the rate calculation than the first method. This will save a lot iteration time, thus improve the effectiveness of the solving process.

Numerical method

There are numerous multivariable solvers available for this system of equations based on different algorithms.

DNEQBF (a built-in algorithm for IMSL libraries) is the double precision adaptation of Broyden's method, which is a modified multivariable Newton's method that applies a numerical estimation of the Jacobian matrix for the updating formula. Simplex methods are also considered for this model. Simplex works better for stiff problems, which is common for multicomponent MBIE model. Several revised Simplex methods are considered, which included:

- The Revised Simplex Method
- The Bartels-Golub Method
- The Sparse Bartels-Golub Method
- The Forrest-Tomlin Method
- Reid's Method

Forrest-Tomlin Method or Reid's Method produced fewer non-zero data entries. Sparse Bartels-Golub Method performs fewer floating-point operations. Since floating-point calculations require the most CPU time in simulation, this advantage would become

a significant speed advantage in a compiled environment. Alternative multi-variable algorithms may also improve the solution.

Start value: Previous slice value or extrapolation of recently calculated result.

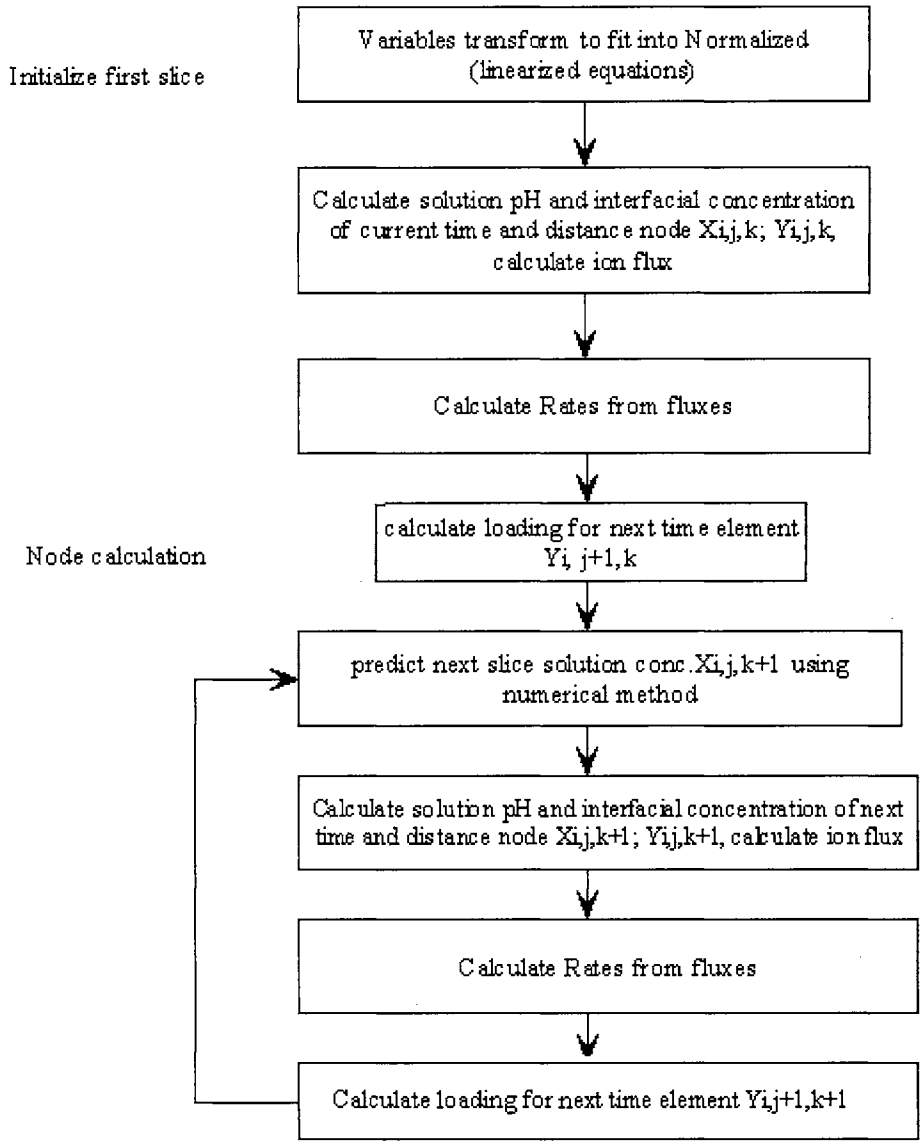


Figure III-3 Flowchart for Solving interfacial concentration with ion flux simultaneously

Prediction of the next slice solution ratio

Equation (III.33) is the solution ratio differential equation written for integration using the Euler's method. Expanding for integration,

$$x_{i,j,k+1} = x_{i,j,k} + R_{i,j,k}^T \Delta \xi_r \quad (\text{III.39})$$

Euler's method is an effective approximation for simple functions, but the error term is second order with respect to the step-size h , written as $O(h^2)$, and higher accuracy is obtained only with smaller step-sizes. The mixed-bed equation system is stiff; the variables do not change in same level of speed, because variables change with different time scales (Gerald, 1992). Higher order accuracy is required for stiff systems, otherwise the calculation becomes unstable.

The fourth-order Runge-Kutta method of numerical integration is popular, it has a fifth order local error, $O(h^5)$, and a global fourth order accuracy, $O(h^4)$. But the application to the mixed-bed system is difficult. It requires four function evaluations per calculation node, and the future values of the rate function are not available as a function of τ and ξ . The rate evaluations require an Euler's method prediction of the solution ratio, which may introduce more local error to the method and also require a lot of computational time.

Several multi-step methods integration methods such as Milne's, Adams-Moulton, and Gear's method have fourth-order accuracy. Of the multi-step methods studied, the Gear's backward difference method was chosen because it requires only one function evaluation per integration step, and only requires the current value of the rate (typically the 'k' index) and the current and three previous values of the solution ratio. The updating formula is below.

$$x_{i,j,k+1} = -\frac{12}{25} \Delta \xi (\text{FR}) R_{i,j,k} - \frac{C_1}{25} \quad (\text{III.40})$$

where

$$C_1 = 3x_{i,j,k-3} - 16x_{i,j,k-2} + 36x_{i,j,k-1} - 48x_{i,j,k} \quad (\text{III.41})$$

Gear's method is initiated with three Eulers integration steps.

Milne's method was not chosen because of unreliable stability while integrating stiff equation systems. The Adams-Moulton method was not chosen because it requires an estimation of the $k+1$ rate function, which may increase error and run-time.

Gear's method has a high order accuracy, $O(h^4)$, and it is reliable in stiff systems. The primary disadvantage of Gear's method is the difficulty in implementing a variable step-size. Variable step-sizes are desired for run-time optimization. The integration increments required for Gear's method are spaced equally distant, which causes difficulties when changing the size of the increment. Varying the step-size for a multi-step method requires an interpolation of the previous values when going to a smaller step size, or averages the range of previous values when going to a larger step size.

The variable step-size must be active when the rates are significantly non-zero in order to be effective. Liu (1998) attempted to use a small step-size for the first three slices past the Euler integration. The algorithm was not implemented correctly, because it did not activate with the exchange zone of the bed. The distance elements that were reduced remained at the top of the bed. Variable step-sizes were not used in this work, but they may be useful for future model optimization.

The solution ratio is created each time slice with only the top slice concentration as the boundary condition, i.e. the values of $x_{i,j,k}$ are only used in the working time slice, and the previous time slice values do not need to be stored. This reduces computer memory considerably, and the variables arrays are declared as $x_{i,k}$ in the computer program.

Programming environment

The algorithm is programmed in FORTRAN 95 with the Compaq Visual Fortran Version 6.5 compiler. The author has discussed with Dr. Hussey, a major contributor of previous version of this program, about the possible programming tools for this model. The major reason that we are using the Visual Fortran is because most of the previous code was in FORTRAN. It can be easily migrated to current environment. Also the New Fortran has some advanced features that make it competitive to C or C++. These features include:

Dynamically allocated arrays

FORTRAN 90 array formulas—Array formula syntax is very flexible. It also allows direct assignment statements of an array to a constant or another array of common dimensions. Array sizes are no longer static. All profile variables are declared as ALLOCATABLE, the number of slices determines the array sizes.

F90 has derived type variables; all real variables are double precision, which means they are eight byte numbers that calculate values to 16 significant digits.

Code readability—FORTRAN 77, though functional, is limited to 72 characters before a continuation character on the sixth column is required. F90 allows 132 characters, and the continuation character is an ampersand at any location on the line, and another ampersand at the beginning of the next line.

The program is built as a QuickWin application, which allows the program to access the swap file in 32-bit Windows operating systems. The usage memory depends on the number of ionic species and the number of calculation slices. The author notes

that if the program is regularly accessing the swap file, which is the cache file for hard drive, the model run-time is greatly increased. Excessive swap file access can be monitored by Windows task manager.

CHAPTER IV

RESULTS AND VALIDATION

Introduction

The previous chapters developed the analytical model for mixed bed ion exchange column and numerical algorithms necessary to solve the model. In this chapter, the results and analysis of the model efforts are presented. Several industry operating cases are discussed and validated with limited industry data. Following topics are presented:

- Model criteria validation
- A parametric analysis to stability and effectiveness of the model
- A case study for Surry NPS condensate polishers. The model is benchmarked to service data.
- The model is evaluated with KAPL's case.

Model criteria validation

Every calculation has an associated error, and at times the error may propagate throughout the run and significantly affect the results. It is a nature of numerical computing. It is also quite possible to 'correctly' enter the necessary equations into a computer program and generate incorrect results. A detailed discussion of the sources of error for the model is described in Chapter III; there are some established criteria to define proper model function.

The criteria based on the model that the results must meet include specifically:

- The column material balance must be maintained
- Ions must elute chromatographically through the bed as a function of time according to valence, selectivity, and diffusivity criteria.
- Smooth solution concentration, resin loading and mass transfer rate profiles without discontinuity or oscillation.
- Infinite run time show effluent concentrations gradually approaching influent concentrations, and resin loadings approaching those predicted by mass action equilibrium with the feed.

Column material balance

The external column material balance algorithm described in previous chapter is one of the most important criteria for the model. It has been monitored throughout all simulations. Generally the mass balance has been satisfied for all of the constituent types in a normal finished simulation. A lithium-sodium-ammonia-chloride system from KAPL is used to demonstrate the dependency of mass balance error to step-sizes. The input parameters and water constituents can be found in Table IV-1 and Table IV-2. Figure IV-1 and Figure IV-2 below shows bar charts of both cation and anion mass balances with respect to time step-size and distance step-size for this system.

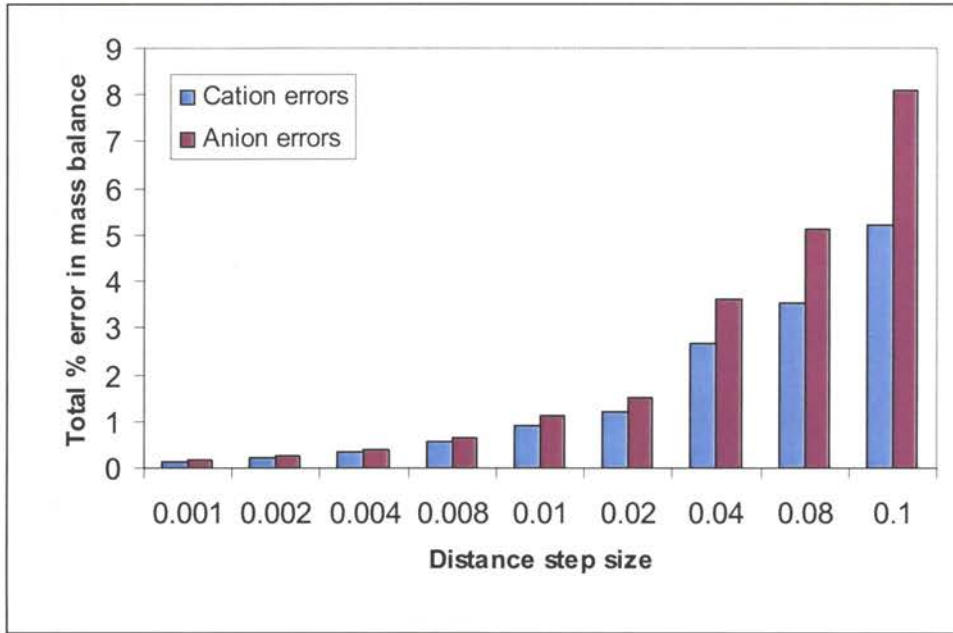


Figure IV-1. Mass balance error as related to distance step-size (time step-size at 0.01)

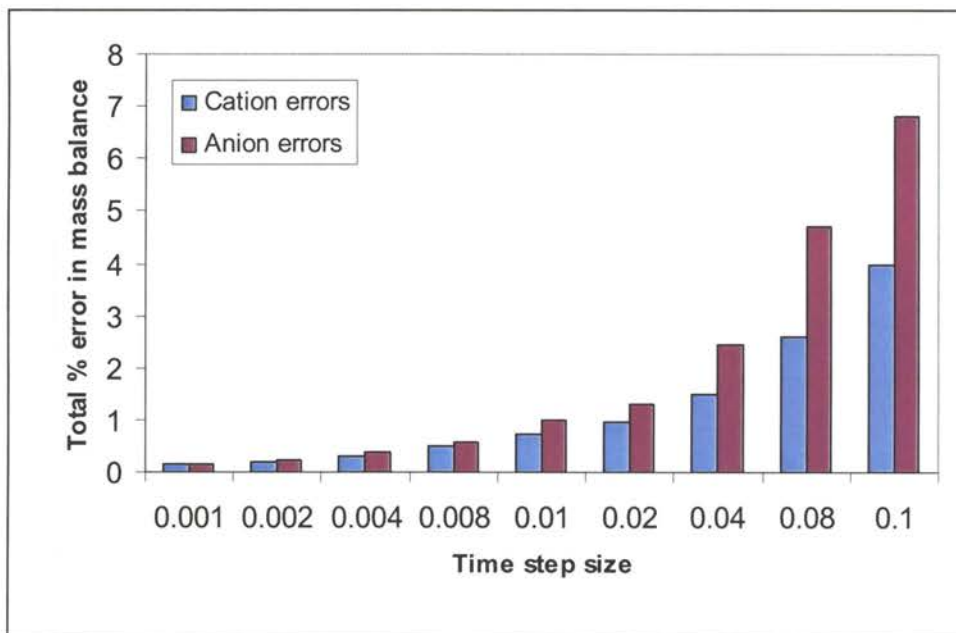


Figure IV-2. Mass balance error as related to time step-size (distance step-size at 0.01)

From the charts, it is clear that the smaller the distance and time step-size, the smaller the total mass balance error. Also the mass balance error is more sensitive to

distance step-size than time step-size from the result. In this case, the cations have smaller mass balance errors than anions. This is not always the case in other runs. It's not affected by any model parameters.

There's always a trade off between step-size and run time. It will be discussed in details in stability analysis later. In general, a bigger size step means less run time. But too big step-size will lead to big truncation error, which will crash the program or give meaningless results because of the big errors. Small step-size does not always lead to better results because the longer run time will involve more round off errors. For the current program, the author thinks 0.01 by 0.01 would be a good step-size to start with for most cases.

Table IV-1 Bed geometry and service parameters for KAPL Lithium column

| Parameter | Value |
|--|----------|
| Bed diameter (feet) | 0.125 |
| Total bed depth (feet) | 9 |
| Flow rate (gpm) | 0.16 |
| Anion resin heel depth (inches) | No |
| Volume fraction of cation resin (non-heel section) | 0.4 |
| Volume fraction of anion resin (in non-heel section) | 0.6 |
| Void fraction | 0.35 |
| Temperature (°C) | 25.0 |
| Cation resin: | |
| Bead diameter (mm) | 0.6258 |
| Capacity (meq/ml) | 1.92.27 |
| Form | Hydrogen |
| Anion resin: | |
| Bead diameter (mm) | 0.5559 |
| Capacity (meq/ml) | 1.1514 |
| Form | Hydroxyl |
| Desulfonation | No |
| Fouling | No |

Table IV-2 Influent concentration and initial loadings for KAPL Lithium column

| Ion | Influent concentration (ppb) | initial resin loading |
|-----------------|---------------------------------|-----------------------|
| Cl ⁻ | 0.001 | 0.0001 |
| Na ⁺ | 0.001 | 0.0001 |
| Li ⁺ | 6.3 | 0.0001 |
| NH ₃ | 21000 | 0.99 |

Effluent concentrations

Effluent concentrations should gradually approach the influent concentrations in infinite run time. This has been verified in almost all cases. But when effluent concentrations are close to a very low level, for example ppt, the calculation error could be noticeable. It is also hard to compare with experimental data since it is hard to measure at that level of concentration. For most UPW application, the effluent profile meets the criteria very well.

Figure IV-3 shows the cations breakthrough profile for the KAPL lithium column case which is discussed in previous part. It shows on the figure that lithium settles near 6.3 ppb which is the influent concentration. For sodium, since the influent is about 1 ppt, the effluent finally settles close to 0 on the figure.

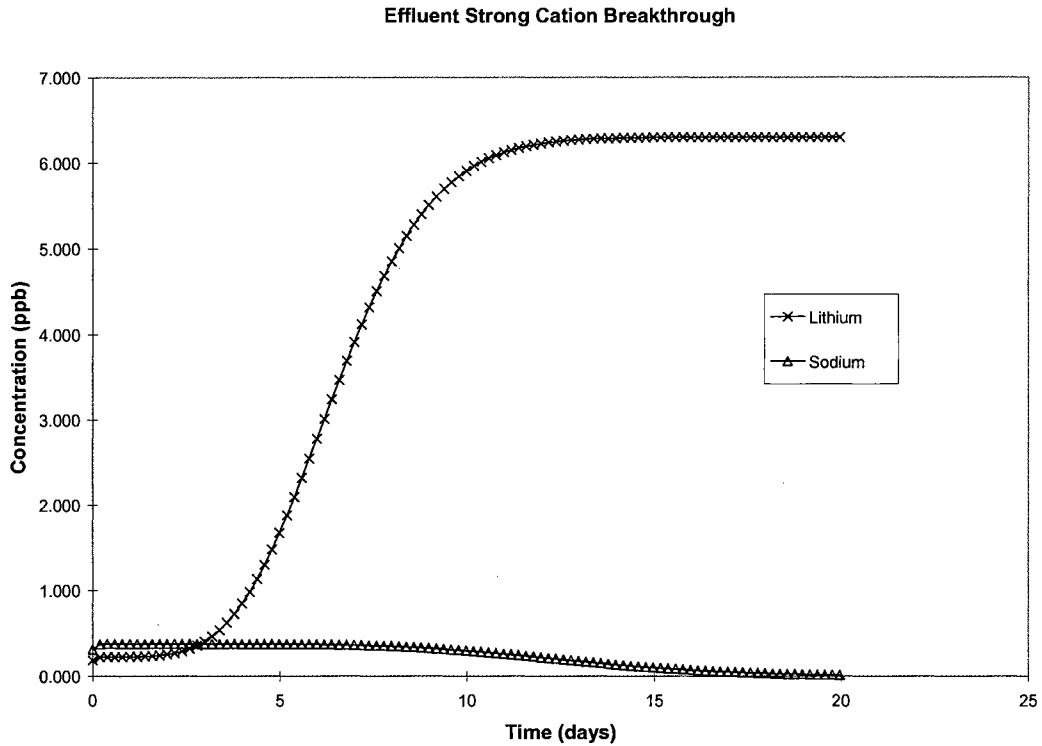


Figure IV-3 Cations effluent profiles for KAPL Lithium column

A Boiling Water Reactor (BWR) case has also been used to test the effluent concentration profile of the model. The bed geometry, resin parameters and feed water constituents are listed in Table IV-3, 4

Table IV-3. Bed geometry and service parameters for BWR polishers

| <i>Parameter</i> | <i>Value</i> |
|---|--------------|
| Bed diameter (feet) | 10.8 |
| Total bed depth (feet) | 3 |
| Flow rate (gpm) | 4800 |
| Volume fraction of cation resin (in non-heel section) | 0.38 |
| Volume fraction of anion resin (in non-heel section) | 0.62 |
| Void fraction | 0.35 |
| Temperature (°C) | 60 |
| Cation resin: | |
| Bead diameter (mm) | 0.63 |
| Capacity (meq/ml) | 2.0 |
| Form | Hydrogen |

| | |
|--------------------|----------|
| Anion resin: | |
| Bead diameter (mm) | 0.525 |
| Capacity (meq/ml) | 1.1 |
| Form | Hydroxyl |
| Desulfonation | Yes |
| Fouling | No |
| Feed pH | 7 |

Table IV-4. BWR Feed water constituents

Cations:

Anions:

| Ion | Feed Concentration | Initial Resin loading | Ion | Feed Concentration | Initial Resin loading |
|------------------|--------------------|-----------------------|--------------------------------|--------------------|-----------------------|
| Ca ⁺² | 0.95ppb | 0 | Cl ⁻ | 0.73 ppb | |
| Mg ⁺² | 0.21ppb | 0 | SO ₄ ⁻² | 1.07 ppb | |
| Na ⁺ | 0.43ppb | 0.0001 | NO ₃ ⁻ | 0.21 ppb | |
| K ⁺ | 0.11ppb | 0 | H ₂ CO ₃ | 4.01ppb | |

Figure IV-4 shows the cation concentrations of the BWR bed under normal operation for a full service run. Observe the initial breakthrough of the contaminants. Sodium effluent concentration is approximately 0.005 ppb. This is primarily due to equilibrium leakage as the initial loading of sodium is 0.1%. Calcium and magnesium do not break during the run. Potassium is assumed to have a zero initial loading, and its diffusivity is high enough ($1.9 \times 10^{-5} \text{ cm}^2/\text{s}$) to allow it to exchange to virtual completion. Sodium breaks through to 0.1 ppb at approximately 500 days. Sodium concentration gradually settles close to the influent concentration, this also holds for potassium from the figure.

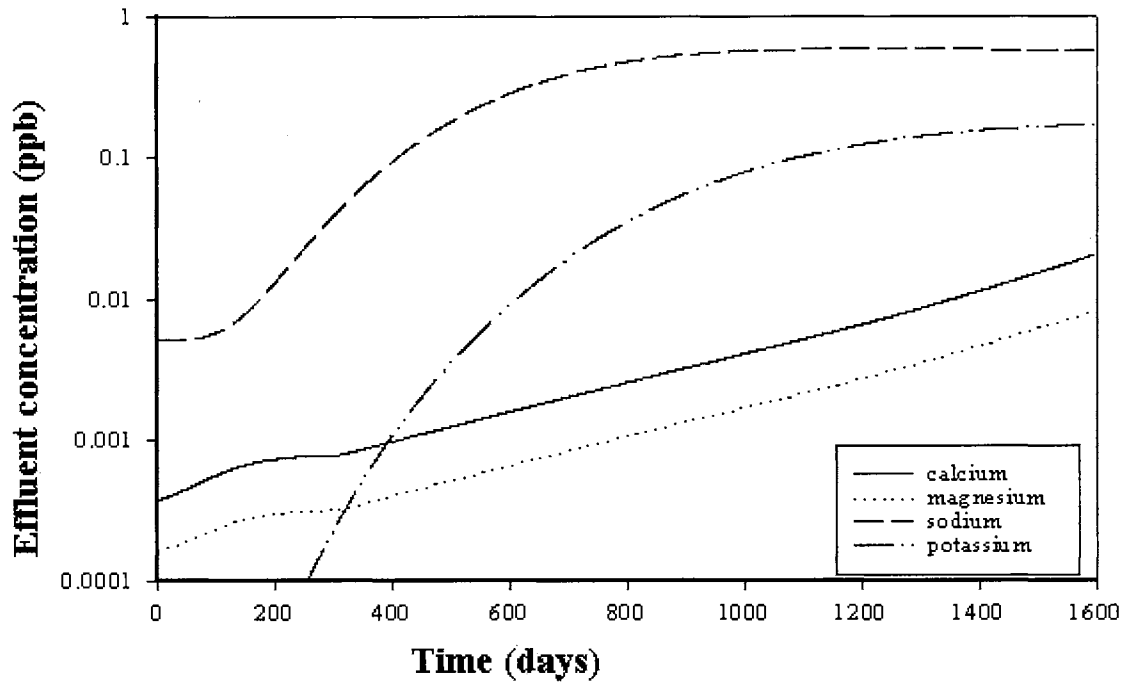


Figure IV-4. A BWR strong cation effluent history

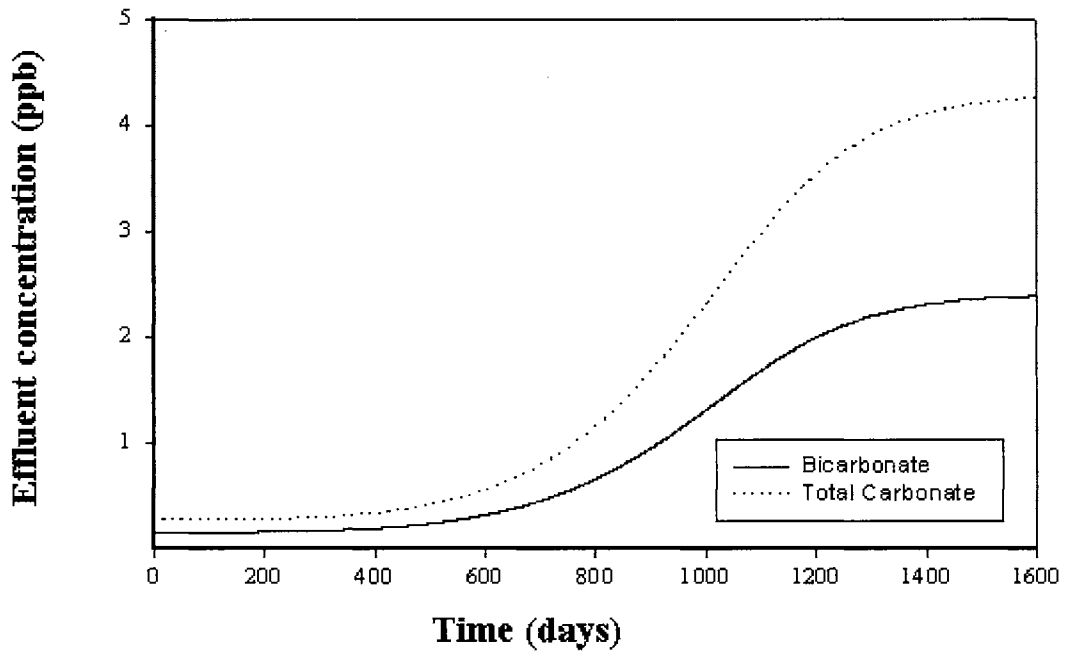


Figure IV-5. A BWR carbonate effluent history

The strong electrolyte anions (sulfate, chloride and nitrate) did not break through to detectable levels during the simulation, but Figure IV-5 shows carbonate breaks through at approximately 500 days operation. It also meets the model criteria as the effluent concentration approaches influent concentration after break.

Loading, solution and rate surfaces

A successful run should also generate smooth loading surface without discontinuity or oscillation. During each dimensionless time and distance increment calculation, the solution fraction, resin equivalent fraction and exchange rate are calculated and exported. The simulator stability is most affected by the rate profiles. If the distance step-size is too large, the rate profiles are the first variable to develop oscillations and discontinuities caused by overestimation of the solution ratio. Profile variables are generated at each time element. These profiles are exported and the constituent data are used to form surfaces describing the solution, resin, and exchange rate.

Figure IV-6 is the loading surface for lithium in KAPL lithium column case. Consider times slightly above zero. The loading of lithium near the top of the bed (distance is equal to zero) is at the highest point for that particular time, and then decays to almost zero near the end of the bed.

As time increases, the lithium loading at the top of the bed increases until it approaches $2.83e-3$ at approximately 3 days, where it remains constant at a plateau as time reaches infinity. Eventually the bottom of the bed has a loading of $2.83e-3$ when time reaches approximately 15 days. The plateau is an indicator that there are no ions displacing lithium for this given system.

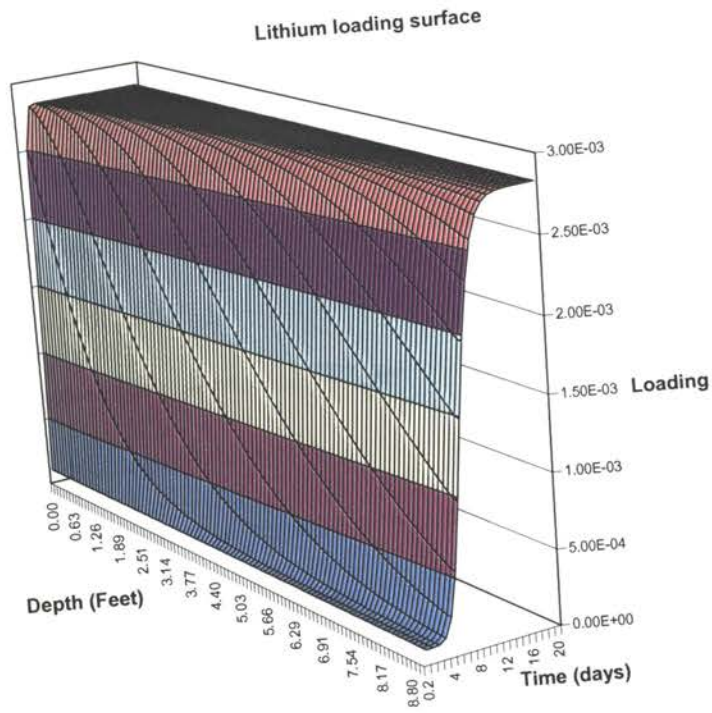


Figure IV-6, Lithium loading surface for KAPL Lithium column

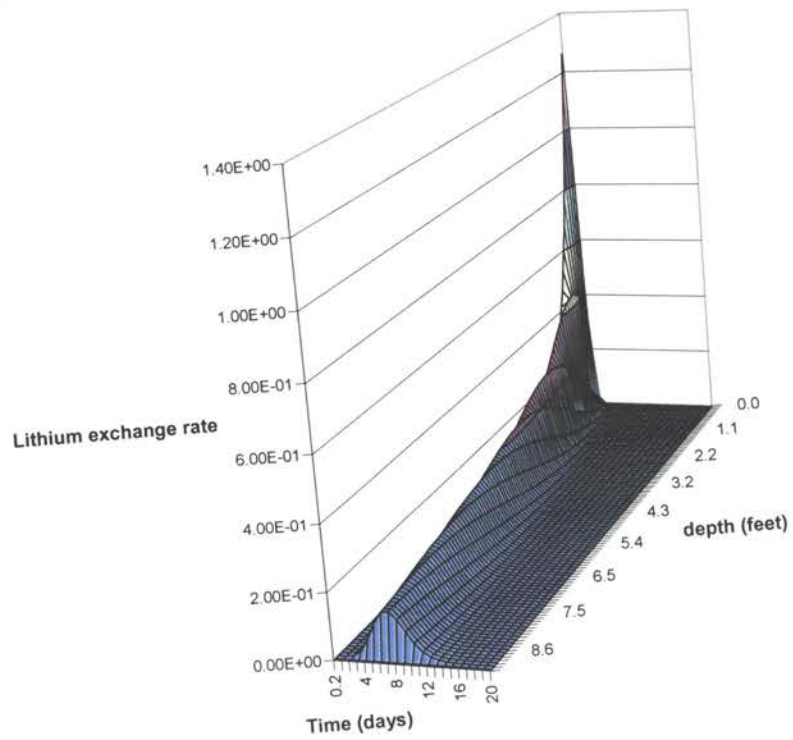


Figure IV-7 Lithium exchange rate surface.

The rate surfaces are more complex than the loading profiles. The values may be positive or negative, and they are not bounded between 0.0 and 1.0. Multicomponent rate surfaces may have several peaks and valleys for each species. Figure IV-7 is a rate surface for KAPL lithium column. Starting the initial time at zero, the lithium rate is positive (ions entering the resin) at the top of the bed, and falls off sharply as the bed length increases. This corresponds with the physical situation because most of the contaminant is exchanged at the top of the bed. The surface is smooth. There is no discontinuity nor oscillation.

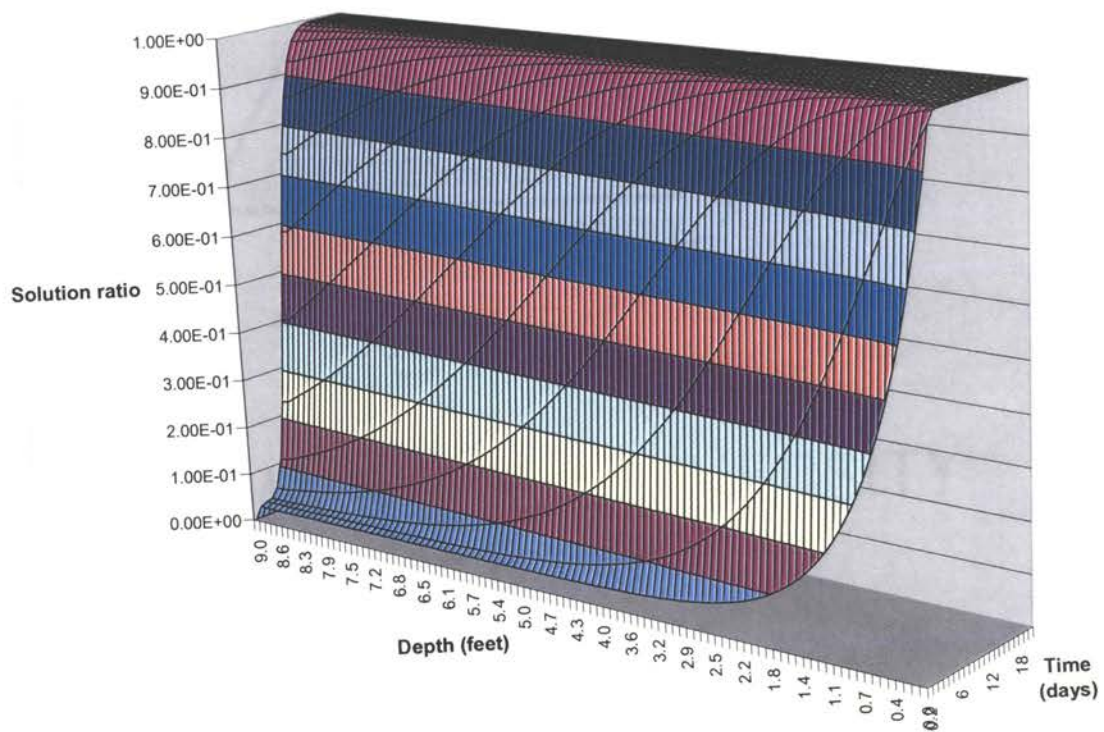


Figure IV-8 Lithium solution ratio surface.

The solution ratio surface for the KAPL lithium column is presented in Figure IV-8. The solution ratio value approaches to a value of unity along with operation time but

decreases with bed depth. The profiles are smooth, which satisfies the criterion established in Chapter III.

Parametric analysis to stability and effectiveness of the model

Solving strategy and algorithm is an important topic during the development of OSU MBIE simulator. It has been discussed early as in Noh's work (1992). As mentioned before, solving a rate-type model is a highly computational task. How to reduce the CPU runtime is one of the priorities for practical model usability. Increasing the dimensionless time and distance step is an effective way to reduce runtime since it reduces the total number of grids calculated. However, larger time and distance steps increase the accumulative calculation error. When error exceeds the criteria of the model (for instance, the column material balance), the program will stop.

In Chapter III new solving strategies are developed in order to improve the stability and effectiveness of the simulator. The new simulator is benchmarked extensively against the older version with various cases. Some of the results will be presented and discussed in this section.

The KAPL lithium column case is also used to evaluate the two solving strategies. This test focused on effectiveness and robustness of the two algorithms. This is not an easy case to run adequately because a high concentration (21000 ppb) of ammonia and a low concentration (6.3 ppb) of lithium are applied simultaneously to the same rate calculation. However, the total material balance error was observed to be less than 5% even for big step size run. All input parameters and feeding water constituents can be

found in Table IV-1, 2. The following table shows the runtime and mass balance errors comparison of two solving methods.

The dimensionless time step ranges from 0.001 to 0.5, while distance step size is from 0.001 to 0.1.

Table IV-5 Runtime result for KAPL lithium case with different τ and ξ combinations

| Solve interfacial concentration separately | | | |
|--|-------|-------------|-----------------------------|
| τ | ξ | Runtime (h) | Comment |
| 0.015 | 0.1 | Failed | Mass balance error |
| 0.015 | 0.007 | 15.33 | |
| 0.15 | 0.07 | 0.20 | Mass balance error >10% |
| 0.15 | 0.1 | Failed | Mass balance error |
| 0.2 | 0.1 | Failed | Mass balance error |
| 0.5 | 0.1 | Failed | Mass balance error |
| 0.1 | 0.01 | 1.475 | Mass balance error <5% |
| 0.005 | 0.005 | 55.45 | |
| 0.001 | 0.001 | 1260* | |
| Solve interfacial concentration with ion flux simultaneously | | | |
| τ | ξ | Runtime (h) | Comment |
| 0.015 | 0.2 | Failed | Negative bulk concentration |
| 0.015 | 0.1 | 0.83 | |
| 0.015 | 0.007 | 12.33 | |
| 0.15 | 0.07 | 0.15 | |
| 0.15 | 0.1 | 0.0875 | |
| 0.2 | 0.1 | 0.075 | |
| 0.5 | 0.1 | 0.0333 | Mass balance error <5% |
| 0.1 | 0.01 | 1.25 | |
| 0.001 | 0.001 | 1030* | |

* Runtime based an estimation of proportional finishing time. This case simulates an operation of 20 days.

The results show that the second solving strategy is capable of handling much bigger time and distance steps compared to the first method. This leads to a dramatic decrease of runtime without significant error costs. From the table, the biggest time and distance steps for the older version of simulator is 0.1X0.01. At this step size, the mass balance error will be less than 5%. While for the new algorithm, the mass balance error

will be less than 5% even when step size is as high as 0.5×0.1 . A step size of 0.2×0.1 is recommended for the second strategies to achieve reasonable simulation results and maintain reasonable runtime.

Another result from the table is that the program is not equally sensitive to time and distance step size. For both new and old versions, it seems that the program can tolerate bigger time step size but is very sensitive to distance step size. This does match the result in Hussey's work (1999). He found that the mass balance error is not sensitive to time step size.

Both methods have not observed the instability in breakthrough curve when τ and ξ are extremely small (0.0005×0.005) reported in previous work (Noh, 1992). But under such small step size combination, the runtime will be much longer and the accuracy will not be improved effectively.

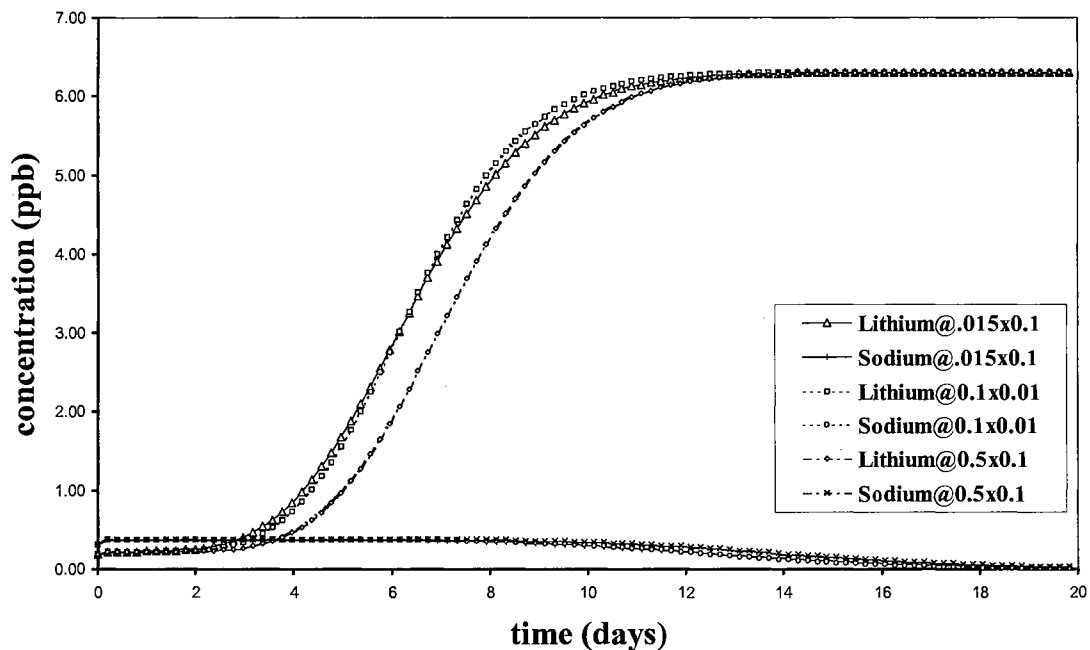


Figure IV-9 A Lithium Cation breakthrough profile with different time and distance steps

Figure IV-9 shows the cation breakthrough history for a lithium case solved by the simultaneous method. Three step size combinations of results are presented on Figure IV-9. Other breakthrough trends are included in APPENDIX B. Basically all breakthrough profiles are very close to each other. The lithium curves with smaller time and distance step break through earlier. The lithium curve@0.5x0.1 is the only one significantly different from the other curves. These results are promising in that at some moderate time and distance step the solution is no longer sensitive to and is relatively independent of, the mathematical solution variables. It indicates that less accurate (to some degree) results can be achieved for some extremely long runtime simulations by tuning the time and distance step to the maximum value than the simulator can tolerate. The better simulation results always can be achieved by decreasing the step sizes.

Another simulation result is for a regenerated mixed bed ion exchange column from Dow Chemical Company. The feed water includes 5 cations and 3 anions. The input data are listed in Table IV-6, 7.

Table IV-6. Bed geometry and service parameters (Dow)

| <i>Parameter</i> | <i>Value</i> |
|---|--------------|
| Bed diameter (feet) | 8 |
| Total bed depth (feet) | 5 |
| Flow rate (gpm) | 2000 |
| Volume fraction of cation resin (in non-heel section) | 0.66 |
| Volume fraction of anion resin (in non-heel section) | 0.34 |
| Void fraction | 0.35 |
| Temperature (F) | 150 |
| Cation resin: Dow 650-C | |
| Bead diameter (mm) | 0.65 |
| Capacity (meq/ml) | 2.0 |
| Form | Hydrogen |
| Anion resin: Dow 550 A | |
| Bead diameter (mm) | 0.55 |

| | |
|-------------------|----------|
| Capacity (meq/ml) | 1.1 |
| Form | Hydroxyl |
| Desulfonation | No |
| Fouling | No |
| Feed pH | 7.5 |

Table IV-7. Feed water constituents (Dow)

Cations:

Anions:

| Ion | Feed Concentration | Initial Resin loading | Ion | Feed Concentration | Initial Resin loading |
|-----------------|--------------------|-----------------------|-------------------------------|--------------------|-----------------------|
| Na ⁺ | 270ppb | 0.05 | Cl ⁻ | 50 ppb | 0.03 |
| NH ₃ | 25ppb | 0.01 | SO ₄ ⁻² | 45 ppb | 0.05 |
| K | 68ppb | 0.01 | carbonate | 780 ppb | 0.05 |
| Mg | 5 ppb | 0.005 | | | |
| Ca | 15 ppb | 0.001 | | | |

The ammonia and carbonate in the feed water will significantly slow down the simulation process because of the dissociative equilibrium calculation involved. The following table shows the runtime and mass balance errors comparison of two solving methods. The dimensionless time step ranges from 0.001 to 0.2, while distance step size is from 0.001 to 0.1.

The Results in Table IV-8 show that the biggest step size for the old version simulator to run the case successfully is 0.01X0.01. A step size 0.005X0.005 is recommended for better accuracy. For the new simulator, the maximum of step size can go up to 0.1X0.05 for this case with a mass balance error of about 7%. A step size of 0.01X0.01 will give a result with less than 1% error. The effluent concentration profiles (0.01X0.01) are in APPENDIX B (Figure B2-B5).

For same step size, the new simulator runs average about 19-25% faster than the old version. And the new solving algorithm also gets better accuracy when compared with old version at same step size.

Table IV-8 Runtime result for Dow case with different τ and ξ combinations

| Solve interfacial concentration separately | | | |
|--|-------|---------------|---|
| τ | ξ | Runtime (h) | Comment |
| 0.001 | 0.1 | Failed | Mass balance error |
| 0.001 | 0.005 | 236* | Mass balance error <3% |
| | | | Mass balance error <5% |
| 0.01 | 0.01 | 11.8 | |
| 0.01 | 0.05 | Stop at 45% | Mass balance error exceeds |
| 0.1 | 0.05 | Failed | Mass balance error |
| 0.2 | 0.1 | Failed | Mass balance error |
| 0.1 | 0.01 | Failed at 29% | Mass balance error exceeds |
| 0.005 | 0.005 | 46.45 | Mass balance error < 1% |
| 0.001 | 0.001 | 1190* | |
| Solve interfacial concentration with ion flux simultaneously | | | |
| τ | ξ | Runtime (h) | Comment |
| 0.001 | 0.1 | Failed | Mass balance error exceeds |
| 0.001 | 0.005 | 192.5* | |
| | | | Mass balance error < 1% (anion 1.3%, cation 0.5%) |
| 0.01 | 0.01 | 9.615 | |
| 0.01 | 0.05 | 2.1 | Mass balance error <3% |
| 0.1 | 0.05 | 0.25 | Mass balance error <7% |
| 0.2 | 0.1 | failed | Mass balance error exceeds |
| 0.1 | 0.01 | 1 | Mass balance error <5% |
| 0.005 | 0.005 | 38.25 | |
| 0.001 | 0.001 | 988* | |

* Runtime based an estimation of proportional finishing time. This case simulates an operation of 10 days.

Note: All above simulation results is calculated on DELL Dimension 8600 desktop computer with configuration of single 1.7 GHz CPU, 256 MB Rambus RDRAM under windows XP OS with SP1.

Surry NPS Condensate Polishers Bed Simulation case

Surry (Virginia) condensate polishers are not achieving sufficient cationic exchanger capacity utilization compared to other plants like millstones. MBIE simulator

was used as part of the tools to predict break time and define the maximum potential bed utilization for the operation of these polishers.

An important component of any analysis that proposes equipment modification is to define what the changes can give you theoretically. For the case of ion exchange there is a limit of the maximum bed utilization possible for a defined effluent concentration. For an amine operated in the hydrogen cycle the amine will exhaust most of the ion exchange capacity until breakthrough. Since the breakthrough end-point concentration for UPW applications are low, the amine loading profile needs to be as steep as possible to maximize the cationic utilization.

The input parameters and water constituents are listed in Table IV-9, 10. Basically all 3 Surry's columns have same diameter but use different cation and anion resin. The resin property is also listed in table IV-11. Millstone column data is listed in Table IV-12, 13.

Table IV-9. Bed geometry and service parameters for Surry PWR polishers

| <i>Parameter</i> | <i>Value</i> |
|---|--|
| Bed diameter (feet) | 8 |
| Total bed depth (feet) | 4 |
| Flow rate (gpm) | 2580 |
| Volume fraction of cation resin (in non-heel section) | 0.575 |
| Volume fraction of anion resin (in non-heel section) | 0.425 |
| Void fraction | 0.35 |
| Temperature (F) | 100 |
| Cation resin: Surry A column Surry B column Surry C column | Dow 650 Amberjet 1600 H Dow 650 HXC |
| Anion resin: Surry A column Surry B column Surry C column | Dow 550 Amberjet 9000 OH Dow MP-725 OH |

| | |
|---------------|------|
| Desulfonation | No |
| Fouling | No |
| Feed pH | 9.28 |

Table IV-10. Surry PWR Feed water constituents

Cations:

Anions:

| Ion | Feed Concentration | Initial Resin loading | Ion | Feed Concentration | Initial Resin loading |
|-----------------|--------------------|-----------------------|-------------------------------|--------------------|-----------------------|
| Na ⁺ | 0.05ppb | 0 | Cl ⁻ | 0.10 ppb | |
| NH ₃ | 100ppb | 0 | SO ₄ ⁻² | 1.10 ppb | |
| ETA | 1700ppb | 0 | Acetate | 5 ppb | |

Table IV-11 Resin Data

| Resin | Crosslinkage | Capacity(meq/ml) | Diameter (cm) |
|-----------------------|--------------|-------------------------|---------------|
| Dowex Monosphere 650 | 10 | 2.1 (2.3 for millstone) | 0.0625 |
| Amberjet 1600 H | 10 | 2.47 | 0.0676 |
| Dow 650 HXC | 10 | 2.39 | 0.0668 |
| Dowex Monosphere 550A | Type 1 | 1.1 | 0.059 |
| Amberjet 9000 OH | Type 1 | 0.82 | 0.0667 |
| Dow MP-725 OH | Type 1 | 0.95 | 0.07 |

Table IV-12. Bed geometry and service parameters for Millstone polishers

| <i>Parameter</i> | <i>Value</i> |
|---|--------------|
| Bed diameter (feet) | 8 |
| Total bed depth (feet) | 4 |
| Flow rate (gpm) | 2850 |
| Volume fraction of cation resin (in non-heel section) | 0.40 |
| Volume fraction of anion resin (in non-heel section) | 0.60 |
| Void fraction | 0.35 |
| Temperature (F) | 100 |
| Cation resin: Dow 650-C | |
| Bead diameter (mm) | 0.65 |
| Capacity (meq/ml) | 2.0 |
| Form | Hydrogen |
| Anion resin: Dow 550 A | |
| Bead diameter (mm) | 0.55 |
| Capacity (meq/ml) | 1.3 |
| Form | Hydroxyl |
| Desulfonation | No |
| Fouling | No |
| Feed pH | 9.0-9.3 |

Table IV-13. Millstone PWR Feed water constituents

| Cations: | | | Anions: | | |
|-----------------|--------------------|-----------------------|-------------------------------|--------------------|-----------------------|
| Ion | Feed Concentration | Initial Resin loading | Ion | Feed Concentration | Initial Resin loading |
| Na ⁺ | 0.01ppb | 0 | Cl ⁻ | 0.10 ppb | |
| NH ₃ | 30ppb | 0 | SO ₄ ⁻² | 1.10 ppb | |
| ETA | 1300ppb | 0 | Acetate | 5 ppb | |
| Hydrazine | 10 ppb | | carbonate | 5 ppb | |
| | | | glycolate oxalate | 10ppb | |

Figure IV-10 shows the Type I weak cation (ETA and ammonia) breakthrough history for Surry A column based on above input. The ETA break time is significantly less than what Surry plant has achieved. The complete breakthrough history Figures for 3 Surry columns and millstone column are included in Appendix B.

They also show the same trend with less service time. The results are summarized in Table IV-14. For all 3 Surry columns, the simulation results show that service time and cation resin capacity utilization are close to plant's data only when ETA break at about 30 ppb. This is higher than the required break concentration.

The initial run results lead to the thought that ion-exchange may not be the only mechanism in this case. We believe that additional molecular form ETA adsorption occurs along with ionic ETA exchange, which is confirmed by an experimental study in a recent EPRI report determined that the additional ETA adsorption capacity for Dow's cation resin. This effect is also confirmed by a single experiment in our laboratories. This is a parameter of MBIE model and can be tuned for specific operating conditions.

Effluent Type I weak Cation Breakthrough

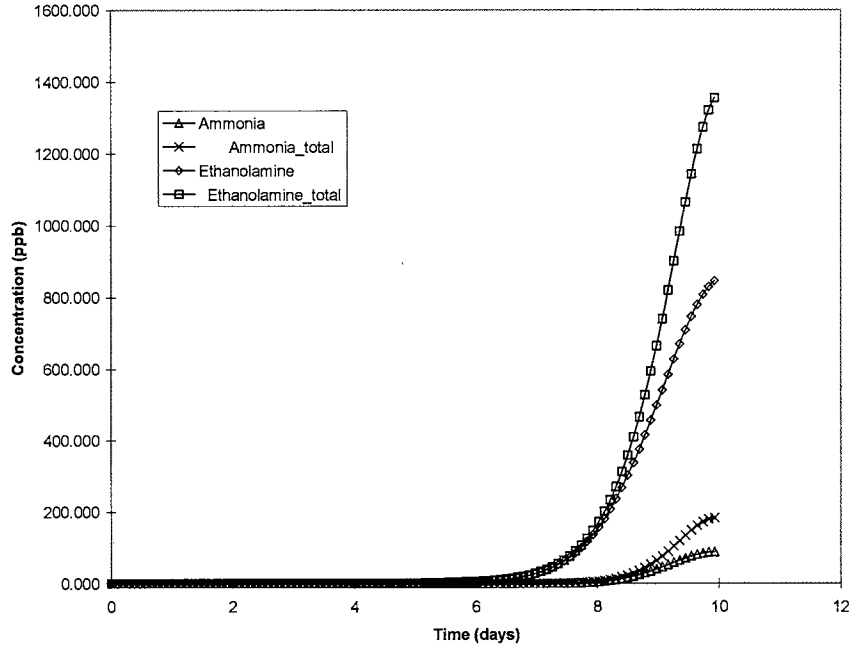


Figure IV-10 Type I Weak Cation breakthrough for Surry A column

Table IV-14 Initial runs result for Surry and Millstone columns

| Surry_A | cation break | | | |
|-----------|--------------|----------|------------------------------|-----------------------------|
| | ETA (ppb) | t (days) | Cation resin utilization (%) | anion resin utilization (%) |
| | 1 | 4.96 | 55.4 | 0.3 |
| | 10 | 6.4 | 71.3 | 0.5 |
| | 30 | 7 | 77.6 | 0.5 |
| | Ammonia | | | |
| | 1 | 7.44 | 82.9 | 0.5 |
| Surry_B | ETA (ppb) | | | |
| | 1 | 5.4 | 48.4 | 0.5 |
| | 30 | 8.3 | 72.2 | 0.8 |
| | Ammonia | | | |
| | 1 | 9 | 81.3 | 0.8 |
| Surry_C | ETA (ppb) | | | |
| | 1 | 5.37 | 50.1 | 0.4 |
| | 30 | 8.1 | 75.5 | 0.6 |
| | Ammonia | | | |
| | 1 | 8.8 | 81.9 | 0.7 |
| Millstone | ETA (ppb) | | | |
| | 30 | 4.74 | 57.8 | 1.8 |
| | Ammonia | | | |
| | 1 | 6.4 | 77.2 | 2.4 |

The Surry and Millstone's data are recalculated with additional ETA adsorption capacity ranging from 30% to 50%. The results show positive improvement for both breakthrough time and the cation resin capacity utilization.

Figures IV-11 and 12 present the loading profiles used to define the maximum theoretical bed utilization for Surry A. The shaded area above and to the right of the "Total" loading curve represents the unused part of the bed (remaining hydrogen fraction). This area over the total area of represents the fraction of unused sites. Without the use of an ETA adsorption term Figure IV-11 shows significantly more unused resin than has been seen in the plant. In addition, with the ion exchange mechanism only, an extended leakage tail precedes the breakthrough curve. Since it is the 1 ppb effluent concentration that dictates run termination, which would result in significantly lower overall bed utilization.

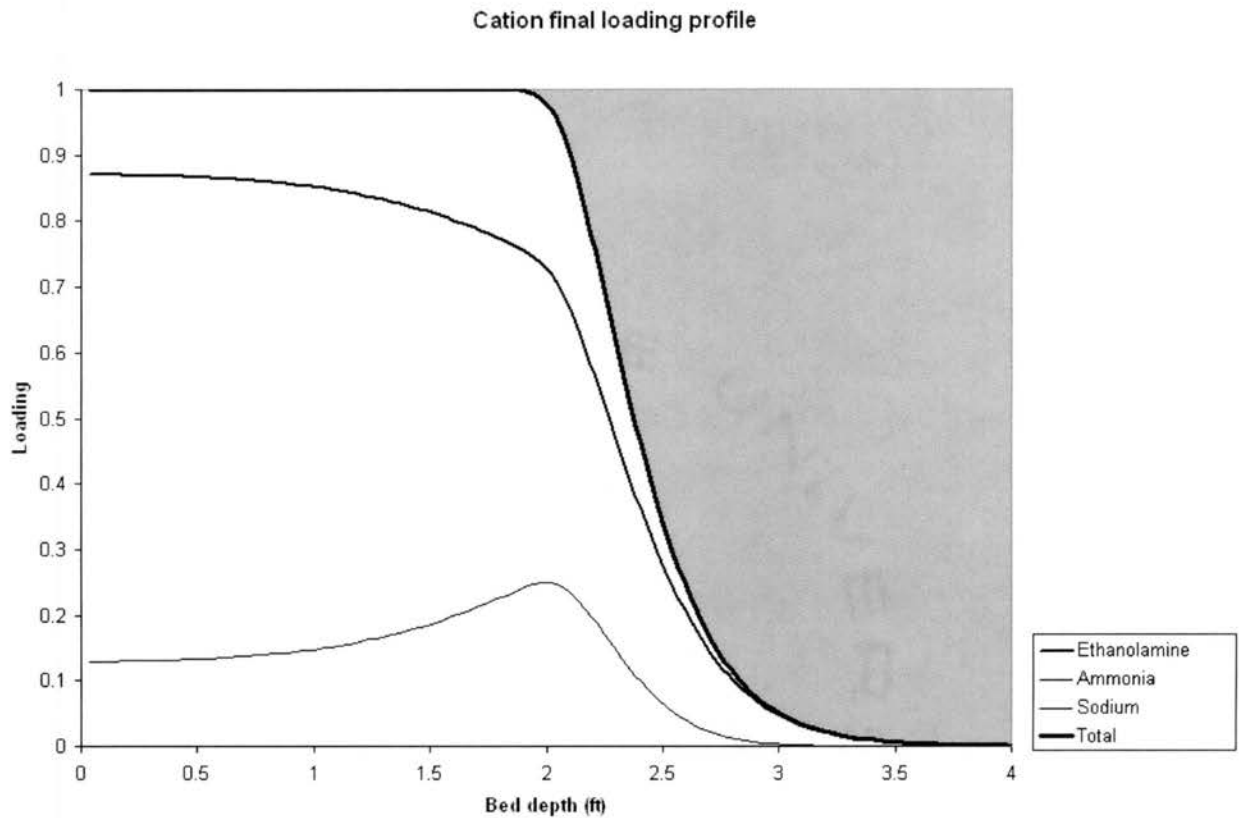


Figure IV-11 Cation loading profile for Surry A at a 1 ppb ETA end point if no additional ETA adsorption occurred.

Figure IV-12 is more representative of the actual bed performance. In this case an additional ETA removal mechanism, adsorption, does occur. Figure IV-12 uses an adsorption capacity that is 30% of the ion exchange capacity. To match specific plant operating this adsorption percentage can be adjusted until run times match prior to doing additional optimization simulations. A key feature of Figure IV-12 shows that the use of adsorption sharpens the breakthrough curve, which means better resin capacity utilization.

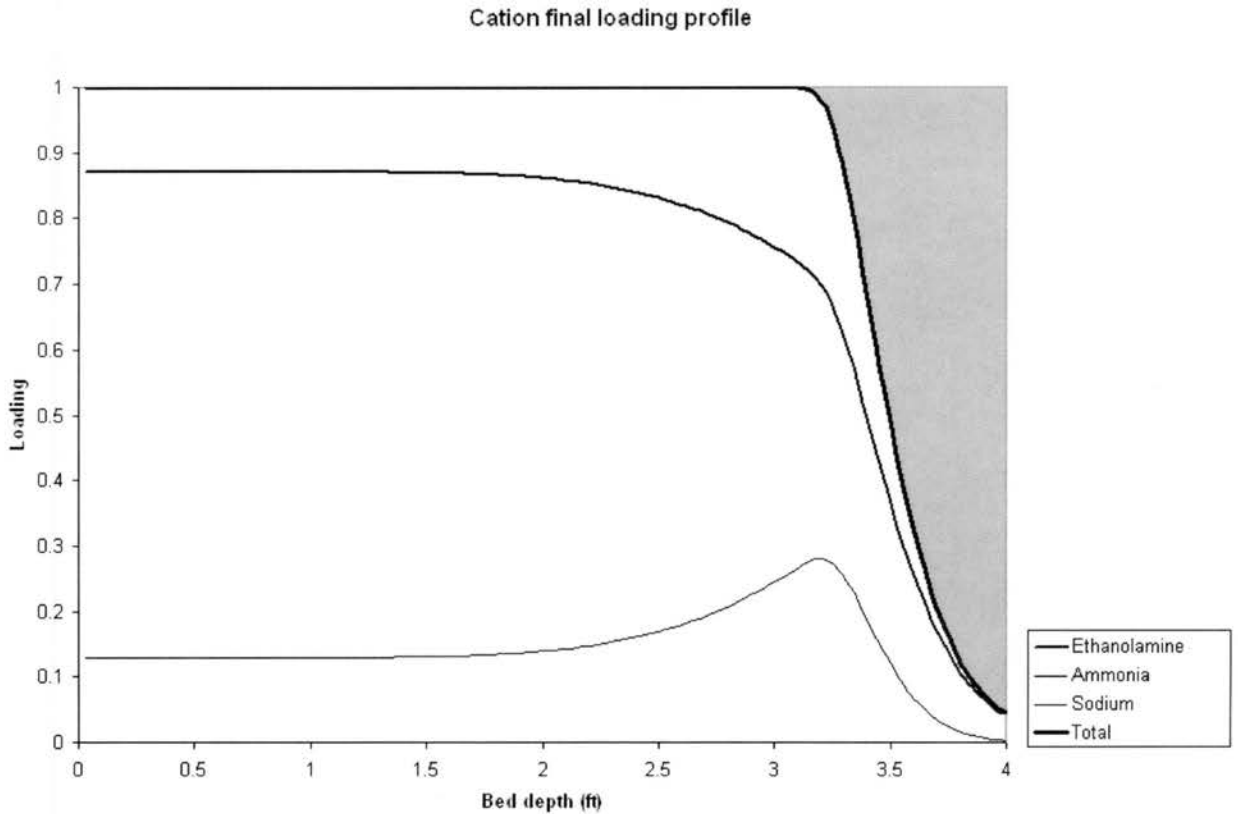


Figure IV-12 Cation loading profile for Surry A at a 1 ppb ETA endpoint (30% adsorption).

Figure IV-13 shows Type I weak cation (ETA and ammonia) breakthrough history for Surry A column with 30% ETA adsorption. Smooth effluent concentration is achieved. The chart shows that ETA breaks to 1 part-per-billion (ppb) at about 8.9 days, while ammonia breaks to 1 ppb at 13 days. Usually at this ETA break, this particular polisher is taken out of service. Complete effluent profiles for Surry and Millstone columns with 30% ETA adsorption are included in APPENDIX B.

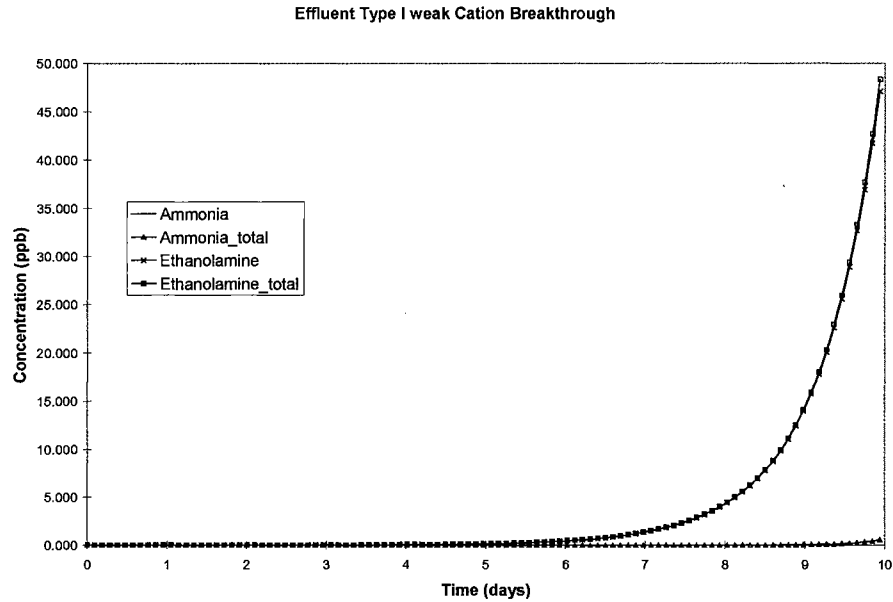


Figure IV-13 Type I weak cation (ETA and ammonia) breakthrough history for Surry A column with 30% ETA adsorption.

For operation, the Surry plant data indicate that they were achieving near 60% cationic utilization, while Millstone was achieving percentages in the upper 80%. The first simulation objective is to define what the maximum utilization is for each specific system. It is likely that expending resources and effort to increase efficiency one or two percent is not cost effective. Table IV-15 presents the results from a series of ion exchange simulations with ETA Adsorption capacity factored in that define the theoretical performance of both the Surry and Millstone polishers.

Several points are of note in Table IV-15. First, ETA – because of its organic structure is not only exchanged with ion exchange resin, but also adsorbs. An experimental study in a recent EPRI report determined that the additional ETA adsorption

capacity for Dow 650/550 mixed bed was approximately 30%. The actual value is likely to be a specific function of the system, particularly temperature and resin variations. Since the run time to a 1.0 ppb ETA break varies significantly with this additional adsorption three cases are presented in Table IV-15 (30, 40 and 50 percent). This adsorption range bounds the number of days operation for Surry. We were expecting run times to 1.0 ppb ETA break near 8 days, so the 40% adsorption values will be discussed here. For example, Surry A could theoretically achieve 89% cationic resin utilization. With the current utilization near 60% there is significant opportunity for improvement in the performance of the Surry polishers. For Millstone the theoretical cationic utilization is slightly higher – calculated at 90% -- and their actual performance of 87-88% indicated that facility is doing very well. Note that the Millstone endpoint is given as 10 ppb ETA rather than 1 ppb. Typically, the better your regeneration efficiency the higher the ETA break concentration you can tolerate. Surry A column is also expected to have a 0.5 ppt sodium effluent concentration at the point of ETA break, while Millstone is predicted to have a 4.5 ppt sodium effluent concentration at a 10 ppb ETA break. These predicted sodium values were not checked against plant operating data. Another point that should be mentioned about the data in Table IV-15 is that no fouling is assumed to occur and the MTC is that calculated for film mass-transfer only based on the bead size and flow conditions.

Table IV-15 Simulation Results for Resin Utilization with ETA adsorption.
(C/A = 57.5:42.5 for Surry, C/A = 40:60 for Millstone)

30% ETA adsorption;

| | ETA break (ppb) | Sodium (ppb) | t (days) | Cat. loading (%) | An. loading (%) |
|------------------|-----------------|--------------|----------|------------------|-----------------|
| Surry_A | 1 | 7e-5 | 7.2 | 84 | 0.7 |
| Surry_B | 1 | 3.8e-5 | 7.8 | 76 | 0.9 |
| Surry_C | 1 | 4.2e-5 | 7.8 | 79 | 0.8 |
| Millstone | 10 | 3e-4 | 6.5 | 84 | 6.3 |

40% ETA adsorption

| | ETA break (ppb) | Sodium (ppb) | t (days) | Cat. loading (%) | An. loading (%) |
|------------------|-----------------|--------------|----------|------------------|-----------------|
| Surry_A | 1 | 5e-4 | 7.7 | 89 | 0.8 |
| Surry_B | 1 | 1e-4 | 8.4 | 83 | 1.0 |
| Surry_C | 1 | 1.45e-4 | 8.4 | 83 | 0.9 |
| Millstone | 10 | 4.5e-3 | 7.4 | 90 | 7.7 |

50% ETA adsorption;

| | ETA break (ppb) | Sodium (ppb) | t (days) | Cat. loading (%) | An. loading (%) |
|------------------|-----------------|--------------|----------|------------------|-----------------|
| Surry_A | 1 | 7e-4 | 8.3 | 93 | 0.9 |
| Surry_B | 1 | 2e-4 | 9.0 | 87 | 1.1 |
| Surry_C | 1 | 2.7e-4 | 8.9 | 88 | 1.0 |
| Millstone | 10 | 8e-3 | 7.9 | 94 | 8.9 |

Several factors would present approaching the theoretical maximums indicated in Table IV-15. These include mal-distribution of the flow, disturbance of a uniform resin surface, fouling, regeneration and rinse-down efficiencies, unidentified spikes in polisher feed concentrations and system temperature (both average and daily cyclic).

While we were defining the theoretical system performance, we also performed several simulations to determine other operating issues. Table IV-16 presents a check that the current cationic to anionic resin ratio is reasonable. This was done by changing the resin mix by 10% to see if bed utilization could be improved. In all cases for Surry the cationic loading efficiency was best at the cation to anion resin ratio used currently in the plant. In Table IV-17 the regeneration efficiency was evaluated for Surry. The only significant change is the leakage of sodium at the 1.0 ppb ETA break. For example, Surry A sodium increases from the theoretical 0.7 ppt to 2.1 ppt with 0.1% initial sodium and 10 ppt with 0.5% initial sodium. This table simply reinforces the need for effective resin separation and / or some means of post regeneration rinsing.

Table IV-16. Results for +/- 10% C/A Ratio. (Based on 30% ETA adsorption)

| | cation: anion | ETA break (ppb) | Na (ppb) | t (days) | Cat. loading % | An. loading % |
|---------|---------------|-----------------|----------|----------|----------------|---------------|
| Surry A | 47.5: 52.5 | 1 | 8.7e-5 | 5.0 | 61 | 0.6 |
| | 57.5:42.5 | 1 | 7e-5 | 7.2 | 84 | 0.7 |
| | 67.5:32.5 | 1 | 5e-5 | 12.6 | 76 | 1.0 |
| Surry B | 47.5: 52.5 | 1 | 6.3e-5 | 5.2 | 57 | 0.7 |
| | 57.5:42.5 | 1 | 3.8e-5 | 7.8 | 76 | 0.9 |
| | 67.5:32.5 | 1 | 3.2e-5 | 14.8 | 72 | 1.4 |
| Surry C | 47.5: 52.5 | 1 | 8.6e-5 | 5.1 | 57 | 0.6 |
| | 57.5:42.5 | 1 | 4.2e-5 | 7.8 | 79 | 0.8 |
| | 67.5:32.5 | 1 | 2.2e-5 | 14.4 | 73 | 1.2 |

Table IV-17. Surry case with 0.1% and 0.5% Na and Cl initial loading

| | ETA (ppb) | Na(ppb) | t (days) | Cat. loading (%) | An. loading (%) |
|---------|-----------|---------|----------|------------------|-----------------|
| Surry_A | | | | | |
| 0.1% | 1 | 2.1e-3 | 8.2 | 89 | 0.9 |
| 0.5% | 1 | 1e-2 | 8 | 89 | 1.3 |
| Surry_B | | | | | |
| 0.1% | 1 | 2.1e-3 | 8.5 | 83 | 1.1 |
| 0.5% | 1 | 1.1e-2 | 8.4 | 83 | 1.4 |
| Surry_C | | | | | |
| 0.1% | 1 | 2.1e-3 | 8.5 | 84 | 1.0 |
| 0.5% | 1 | 1.1e-2 | 8.4 | 84 | 1.3 |

(Based on 40% ETA adsorption)

After defined the theoretical maximum utilization of the columns, the simulator is used to model what is real operation condition at Surry plant. CFD analysis by Swapnil Dhumal and Dr. G Fouch showed that the design of the inlet will result in the flow pattern mal-distribution, which will lead to an uneven surface of the resin beads. This does match the observation in Surry's plant. The following Figures show graphical representation of the resin surface.

Figure IV-14 is the initial effect of the surface. After that resin beads are pushed towards the center of the bed. Figure IV-15 represent the surface condition after several days service. The Figures clearly shows there is serious uneven distribution at the resin surface.

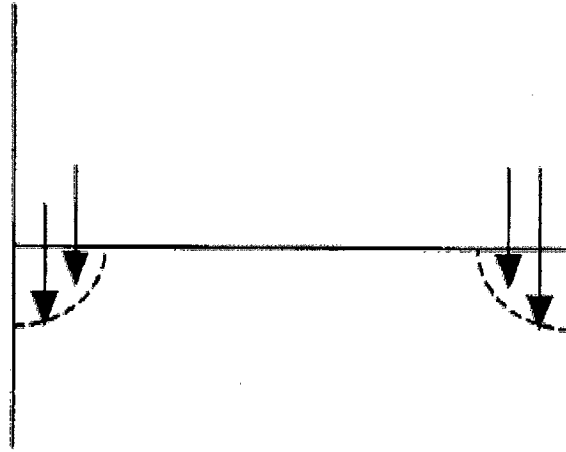


Figure IV-14 Initial effect on Surry column

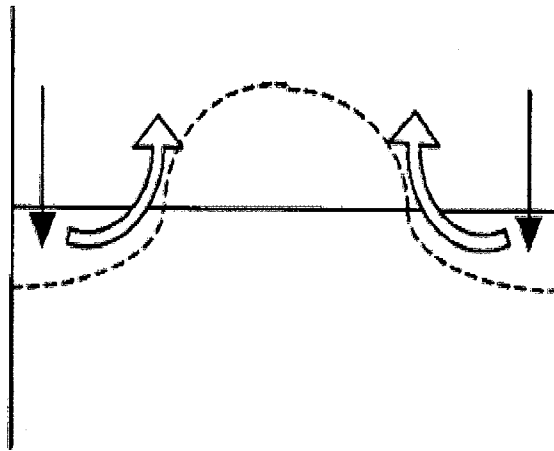


Figure IV-15 Resin surface several days after the stage in Figure IV-14

In order to get simulation result that better represents the real condition in Surry plant. A diagram of column showed in Figure IV-16 is introduced. The column is made up of two individual parts: the longer inner column and the shorter outside column. The total volume should equals to the original bed size.

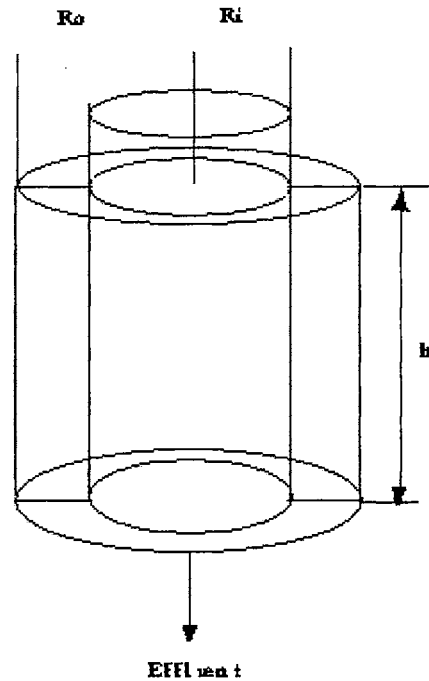


Figure IV-16 Two column approximation diagram of the Surry ion exchange column

The mal-distribution of flow observed by CFX , which is confirmed by a visual observation in the plant, can be approximated with the bed simulation program as two combined beds – each with a different depth and diameter. The required information is that the total water processed and the total volume of resin remains the same. Also, it is assumed that the cation to anion resin ratio does not vary throughout the bed. If you select the geometry of each column (depth and diameter) then the second column bed depth and diameter can be calculated. The detailed methodology for two-bed approximation of an uneven resin bed and calculation procedures can be found in Appendix D. For an example case (Appendix D) we used a 16 inch depth difference between the two beds. The shorter bed will be a path of least resistance for the water

flow so that the flow rate will be greater through this part of the bed. For the case where resin is pushed toward the center the flow will be greater through the bed in the shallow region near the wall. The Ergun equation can calculate the relative flow through each part of the bed. For the example in Appendix D the deeper, central section of the bed allowed 556 gal/min, while the thinner outer region gave a flow rate of 2024 gal/min. These two hypothetical beds are then solved on the computer separately and the results added together to get the total bed performance. The results are summarized in Table IV-18. Table IV-18a lists the separate column conditions approximated for this case. Table IV-18b gives both the total and two bed results. The key results compared to the ideal case listed in Table IV-15 is that the cation resin utilization drops from 89 to 79% and the run time drops from 7.7 to 6.8 days due to the central core of deeper resin. The actual Surry bed performance of only 60% would indicate that the central core is larger. As seen in Table IV-18a, we used a thicker section of approximately $\frac{1}{4}$ the area. As a result, to get to 60% the central core area would need to be greater, closer to $\frac{1}{2}$ the total bed area. Trial and error simulations could give us the actual area affected; however, it is clear that a non-uniform resin bed can result in flow short-circuiting that can dramatically reduce bed performance.

Table IV-18a Two columns model simulation input for Surry

| Column | bed depth (ft) | bed diameter (ft) | Bed Area (ft ²) | flowrate (g/min) |
|--------|----------------|-------------------|-----------------------------|------------------|
| 1 | 5 | 4 | 12.6 | 572.2 |
| 2 | 3.667 | 6.92 | 37.6 | 2007.8 |

calculated from Ergun equation

Pressure drop 50psi

$V_{s1}/V_{s2}=0.85$ (V_s is average superficial velocity)

Table IV-18b Results of a two-column simulation for Surry

| Surry A | | | | |
|----------------|-----------|----------|------------------|-----------------|
| Column | ETA (ppb) | t (days) | Cat. loading (%) | An. loading (%) |
| | | | | |

| | | | | |
|-------|---------|------|------|------|
| total | 1 | 6.76 | 78.8 | 0.76 |
| 2 | 1.47 | 6.76 | 85.4 | 0.81 |
| 1 | 2.27e-3 | 6.76 | 64.5 | 0.67 |

(Based on 40% ETA adsorption)

In this analysis, the simulation results have defined the optimum performance conditions possible at Surry so that the objective for process improvements can be clearly defined. In this case, if changes in the Surry polishers were to achieve 80+ percent utilization of the cationic resin that would be a reasonable and obtainable goal. 90+ percent utilization is not obtainable. Primarily, efforts should focus on improving the bed surface to a more uniform level. Secondly, a more uniform bed by depth will also show improvements in a more uniform cation to anion resin ratio throughout the bed (less separation due to surface mixing). Efforts on uniform mixing of the resins after regeneration and enhancing the regeneration process itself are likely to only give marginal improvements until a uniform bed depth is established.

KAPL Multi column operation

OSU MBIE simulator is used to analyze several KAPL ion exchange columns, which also include the lithium case used in early section this Chapter. All KAPL's applications are featuring a very high concentration (21000 ppb) of ammonia in feed water. It is their interest to see ion exchange behavior under such high ammonia concentration. These are not easy cases to run adequately because the high concentration (21000 ppb) of ammonia and the low concentrations of other contaminants are applied to the same rate calculation simultaneously. But a preliminary simulation shows promising results as the mass balance error is well under 2% for this case.

The input data and feed water constituents are listed in Table IV-19, 20

Table IV-19. Bed geometry and service parameters (KAPL multi column)

| <i>Parameter</i> | <i>Value</i> |
|--|--------------|
| Bed diameter (feet) | 0.083 |
| Total bed depth (feet) | 2.95 |
| Flow rate (gpm) | 0.0317 |
| Volume fraction of cation resin (in non-heel section) | 0.4 |
| Volume fraction of anion resin (in non-heel section) | 0.6 |
| Void fraction | 0.35 |
| Temperature (F) | 77 |
| Cation resin: Ionac c-267 | |
| Bead diameter (mm) | 0.80 |
| Capacity (meq/ml) | 2.27 |
| Anion resin: Dowex ASM-1 | |
| Bead diameter (mm) | 0.59 |
| Capacity (meq/ml) | 1.514 |
| Desulfonation | No |
| Fouling | No |
| Feed pH | 10.15 |

Table IV-20. Feed water constituents (KAPL multi column)

Cations:

Anions:

| Ion | Feed Concentration | Initial Resin loading | Ion | Feed Concentration | Initial Resin loading |
|-----------------|--------------------|-----------------------|-----------------|--------------------|-----------------------|
| Na ⁺ | 0.001 ppb | 0.0001 | Cl ⁻ | 0.001 ppb | 0.0001 |
| NH ₃ | 21000 ppb | 0.99 | | | |
| Fe | 0.80 ppb | 0.0001 | | | |
| Ni | 0.24 ppb | 0.00001 | | | |
| Co | 1.41 ppb | 5e-7 | | | |

Effluent Strong Cation Breakthrough

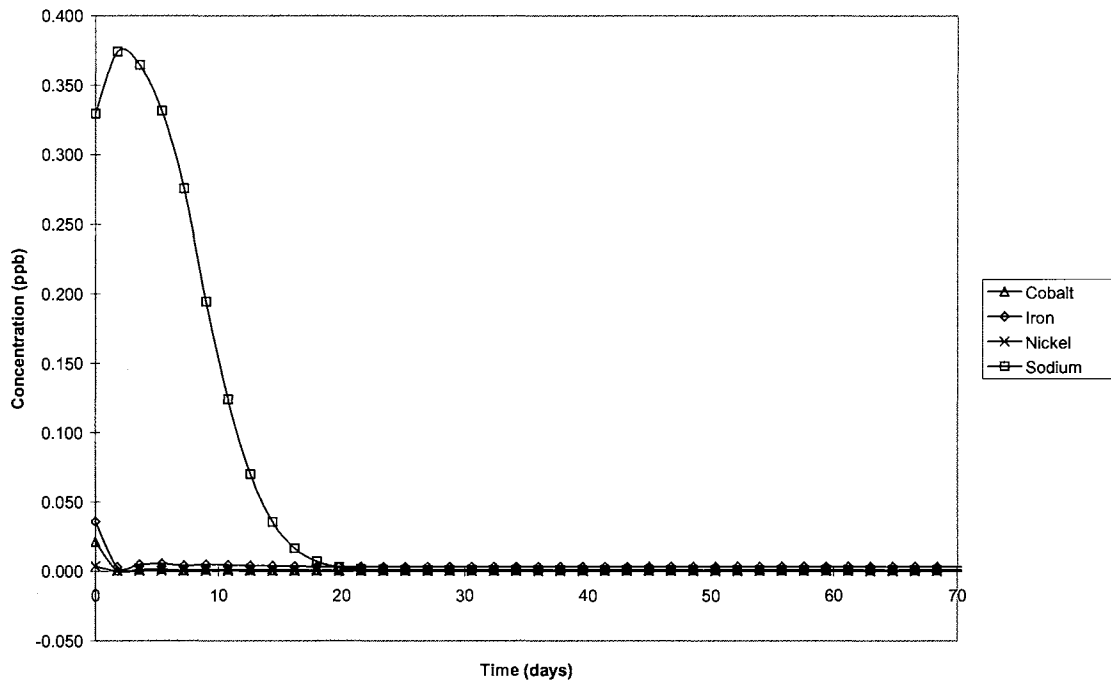


Figure IV-17 Strong cation effluent profile for KAPL Multi-column

Figure IV-17 shows the strong cation effluent history. The simulation simulated for a 180 days operation, there's no breakthrough of any strong cations observed except the early leakage of sodium. This could be caused by the displacing of other contaminants.

Figure IV-18 shows the effluent history of ammonia. Since the column is almost saturated with ammonia, the ammonia breaks very early to its feeding concentration. All results show no discontinuity or oscillation, which satisfied the model criteria.

Effluent Type I weak Cation Breakthrough

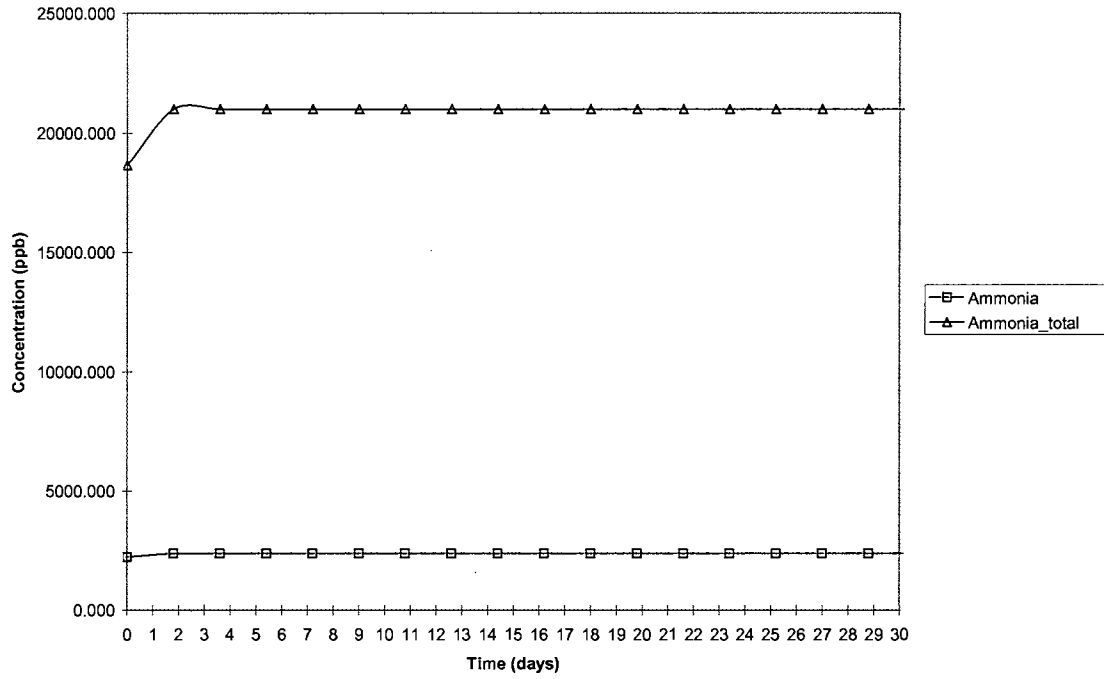


Figure IV-18 Ammonia effluent profile for KAPL Multi-column

Strong Cation loading profiles

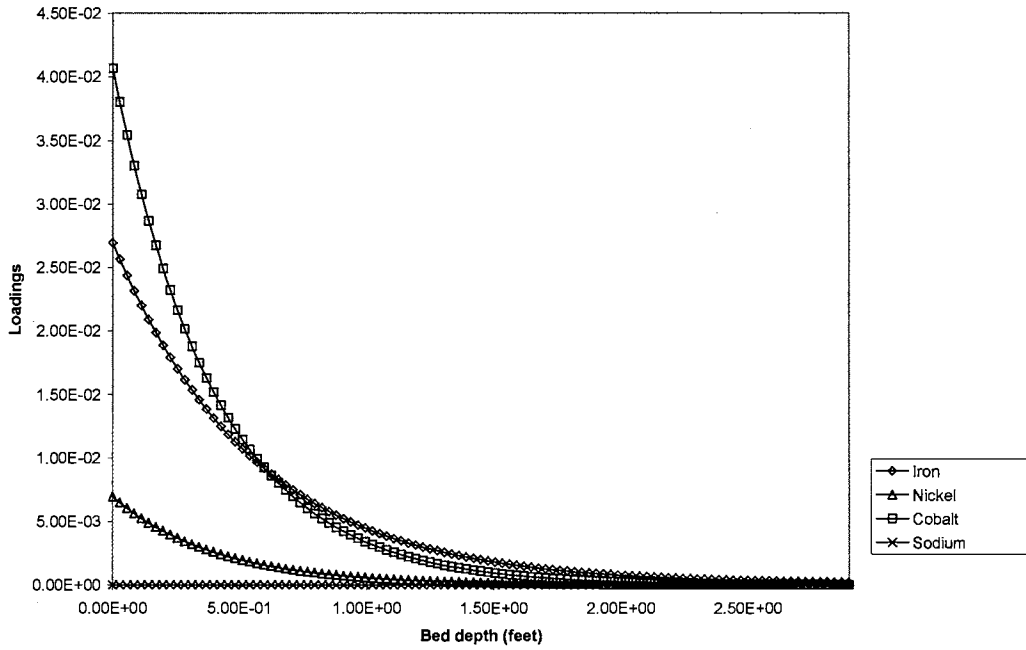


Figure IV-19 Strong cation ions profiles for KAPL Multi-column after 180 days.

Figure IV-19 shows the Strong cations loading profiles along the bed. Smooth solution achieved. This provided very useful preliminary information for the possible radioactivity distribution in the bed because Co and Ni are the major transport media for radioactivity. This will be discussed in Chapter V.

CHAPTER V

THE ADDITION OF RADIOACTIVE SPECIES

Introduction

Radioactivity is always the primary safety concern for any nuclear applications. For a continuously operated mixed bed ion exchange column in nuclear power applications, radioactivity could be transported by various radioactive isotopes. It will be useful to know the radioactivity distribution in this type of ion exchange system. The radioactive isotopes of KAPL's interest include:

- Cobalt-58, $T_{1/2} = 71.8$ days; Co-58 becomes Ni-58 (stable)
- Cobalt-60, $T_{1/2} = 5.27$ years; Co-60 becomes Ni-60 (stable).
- Sodium-24, $T_{1/2} = 15.02$ hours; monovalent cation Na-24 becomes Mg-24 (stable)
- Fluorine-18, $T_{1/2} = 1.83$ hours; monovalent anion F-18 becomes O-18 (stable)

(Above data from: "The Chart of the Nuclides," published by KAPL)

Radioactive isotopes water chemistry is complex because of the possible formation of both cation and anion species from a single constituent, as well as the tendency of metal oxide complexes to form polynuclear aggregate species (Baes et al.

1976). Since current MBIE simulator is capable of calculating the loading profiles of any contaminants in ion exchange column, it should be able to simulate the radio isotope distribution by integrating the radioactive decay reaction into MBIE model equations.

Additional model assumptions:

- Radioactive isotopes have the same property data with non-radioactive isotopes except molecular weight, for example: Co⁶⁰ and Co⁵⁸ should have same selectivity as Co⁵⁹.
- Radioactive decay reaction is the only reaction that radioactive isotopes involved. The reaction to form polynuclear aggregate species is not considered in this model. Based on this simplification, the adsorption of polynuclear aggregate species won't be factored into model.

Model equations

Radioactive decay reaction

The decay half-life ($\gamma_{1/2}$) is related to the decay constant, L as follows:

$$\gamma_{1/2} = \ln(2)/L \quad (V.1)$$

here L has units of reciprocal time.

The decay rate is expressed as a first order reaction

$$\left(\frac{dN}{dt} \right) = -L \cdot N \quad (V.2)$$

This integrates to:

$$Nt = N_0 \cdot \exp(-L \cdot t) \quad (V.3)$$

The decay reaction will change the concentration both in resin phase and bulk fluid. This will change the coefficient in the interfacial concentration calculation. Thus

has impact on the ion flux for the radioactive species. The mass balance equation should include the first order decay reaction.

With decay reaction, the overall column material balance for radioactive species 'r' in an ion exchange column can be expressed as

$$\frac{\partial C_r}{\partial t} + \frac{\mu}{\varepsilon} \frac{\partial C_r}{\partial z} + (FR) \frac{1-\varepsilon}{\varepsilon} \frac{\partial q_r}{\partial t} - (C_r + (FR) \frac{1-\varepsilon}{\varepsilon} q_r) L = 0 \quad (V.4)$$

For the new species generated in decay reaction, column material balance will be:

$$\frac{\partial C_s}{\partial t} + \frac{\mu}{\varepsilon} \frac{\partial C_s}{\partial z} + (FR) \frac{1-\varepsilon}{\varepsilon} \frac{\partial q_s}{\partial t} + (C_r + (FR) \frac{1-\varepsilon}{\varepsilon} q_r) L = 0 \quad (V.5)$$

here C_r and C_s is the total solution concentration of radioactive isotope and its stable isotope. q_r and q_s represent the resin phase.

Results and validation

A preliminary test is performed for the included radioactive isotopes: Cobalt-58, Cobalt-60, Sodium-24 and Fluorine-18. First case is for Sodium-24 in a simple system of strong cation and anion. The input data and water constituents are listed in Table V-1, 2.

Figure V-1, 2, 3 shows the strong cation loading history for this simulation. The figures represent the conditions after 1, 2, 3 days of operation respectively. Figure V-1 shows that after 1 day, at the top of the ion exchange column there's as high as 0.5% Mg-24 loaded, which is decayed from the radioactive Na-24. At about 2 feet from the top, there are equally loaded Mg-24 and Na-24 at about 0.07% level. Near the bottom of the bed, Na-24 loading is getting higher than Mg-24. Since there is no Mg-24 in influent, all the loading is from decay reaction.

Table V-1. Bed geometry and service parameters for Sodium-24

| <i>Parameter</i> | <i>Value</i> |
|--|--------------|
| Bed diameter (feet) | 1 |
| Total bed depth (feet) | 6 |
| Flow rate (gpm) | 0.15 |
| Volume fraction of cation resin (in non-heel section) | 0.60 |
| Volume fraction of anion resin (in non-heel section) | 0.40 |
| Void fraction | 0.35 |
| Temperature (°C) | 30 |
| Cation resin: | |
| Bead diameter (mm) | 0.65 |
| Capacity (meq/ml) | 2.0 |
| Form | Hydrogen |
| Anion resin: | |
| Bead diameter (mm) | 0.55 |
| Capacity (meq/ml) | 1.1 |
| Form | Hydroxyl |
| Desulfonation | No |
| Fouling | No |
| Feed pH | 7 |

Table V-2. Sodium-24 Feed water constituents

Cations:

Anions:

| Ion | Feed Concentration | Initial Resin loading | Ion | Feed Concentration | Initial Resin loading |
|------------------|--------------------|-----------------------|-------------------------------|--------------------|-----------------------|
| Sodium-24 | 0.8ppb | 0 | Cl ⁻ | 0.75 ppb | |
| Mg ⁺² | 0 ppb | 0 | SO ₄ ⁻² | 1.07 ppb | |

This simulation length is 3 days.

Cation loading profile

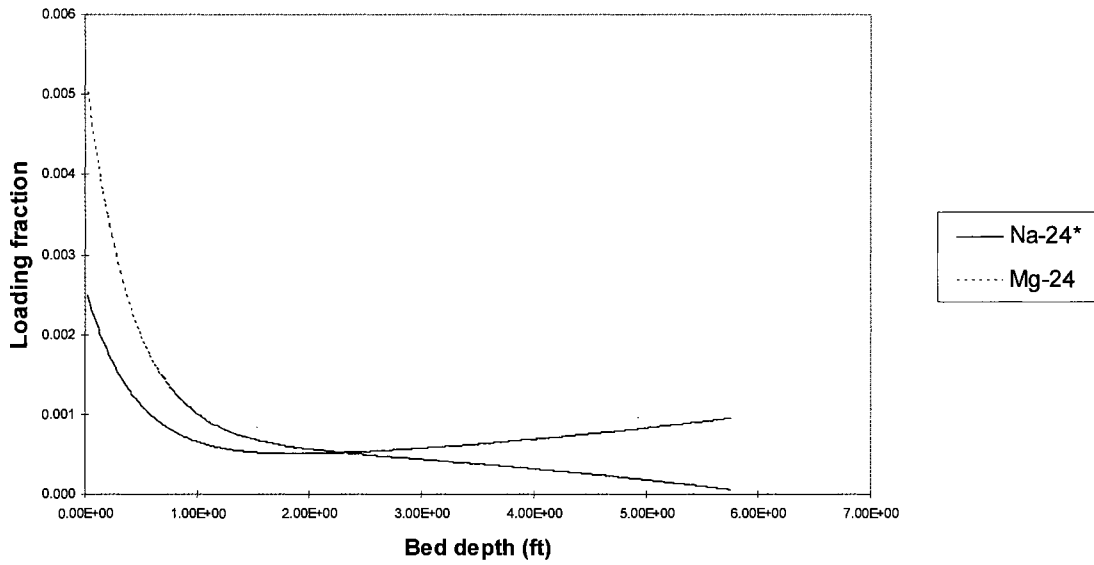


Figure V-1 Na-24 with influent concentration of 0.8ppb after 1 day

Figure V-2, 3 shows the progress of loading profile after 2 and 3 days. Mg-24 loading increased steadily as the more Na-24 has been exchange to resin bed. After 3 days, the Mg-24 loading at the top of the bed reaches 2%. While the loading of Na-24 almost stayed at the same level as the result from 1 day. This shows that Na-24 loading

Cation loading profile

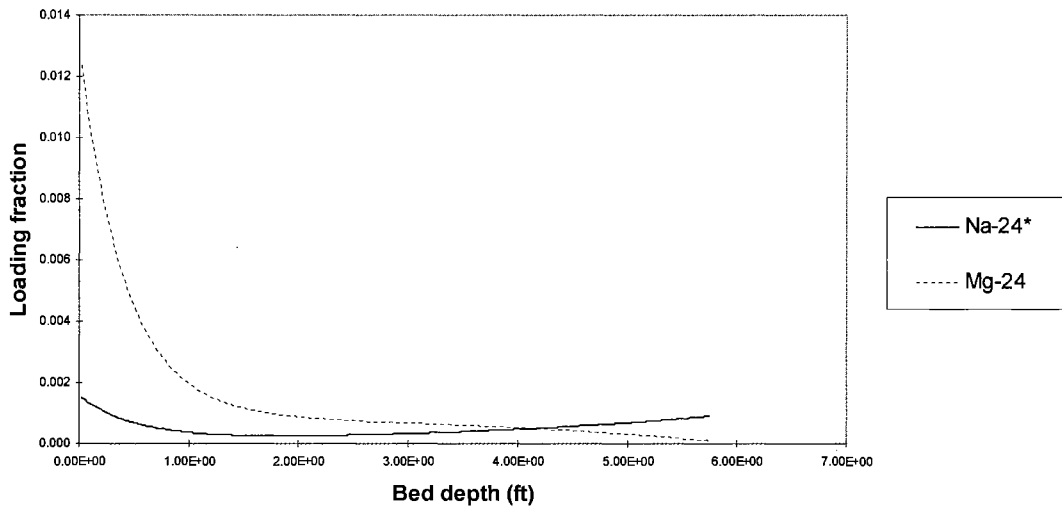


Figure V-2 Na-24 with influent concentration of 0.8ppb after 2 days

Cation loading profile

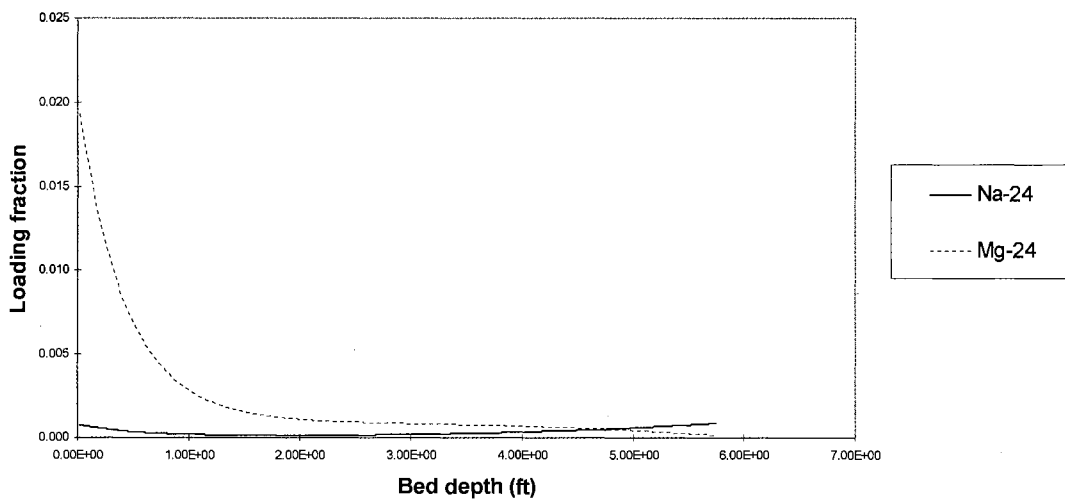


Figure V-3 Na-24 with influent concentration of 0.8ppb after 3 days

concentration is balancing between decay reaction and the ion exchange. As the operation process, the point that Mg-24 and Na-24 have the same loading is moving toward the end of the bed. The loadings show expected trends for these cases; they also match the similar simulation results from KAPL.

The second case is a simulation comparison of same ion exchange column for 30 days. The difference is the feed water. First run feed with Co-59 and Ni-58, which are both stable species. Second run feed with Co-59 and Co-58. Third run feed with Co-59 and Co-60. The input data and feed water constituents are listed in Table V-3, 4.

Table V-3 Bed geometry and service parameters for Cobalt

| Parameter | Value |
|--|----------|
| Bed diameter (feet) | 0.12 |
| Total bed depth (feet) | 4 |
| Flow rate (gpm) | 0.05 |
| Anion resin heel depth (inches) | No |
| Volume fraction of cation resin (non-heel section) | 0.6 |
| Volume fraction of anion resin (in non-heel section) | 0.4 |
| Void fraction | 0.35 |
| Temperature (°C) | 25.0 |
| Cation resin: | |
| Bead diameter (mm) | 0.65 |
| Capacity (meq/ml) | 2 |
| Form | Hydrogen |
| Anion resin: | |
| Bead diameter (mm) | 0.55 |
| Capacity (meq/ml) | 1.1 |
| Form | Hydroxyl |
| Desulfonation | No |
| Fouling | No |

Table V-4. Feed water constituents (Cobalt)

Cations:

Anions:

| Ion | Feed Concentration | Initial Resin loading | Ion | Feed Concentration | Initial Resin loading |
|---------------|--------------------|-----------------------|-----------------|--------------------|-----------------------|
| Co-59 | 1 ppb | 0 | Cl ⁻ | 0.001 ppb | 0 |
| Ni-58 (1 run) | 1 ppb | 0 | | | |
| Co-58 (2 run) | 1 ppb | 0 | | | |
| Co-60 (3 run) | 1 ppb | 0 | | | |

* run for 30 days.

Figure V-4 shows a normal run loading with non-radioactive Co-59 and Ni-58 for 30 days. Ni-58 has a little higher loading than Co-59.

Figure V-5 shows same run with Co-59 and radioactive Co-58 in influent. Based

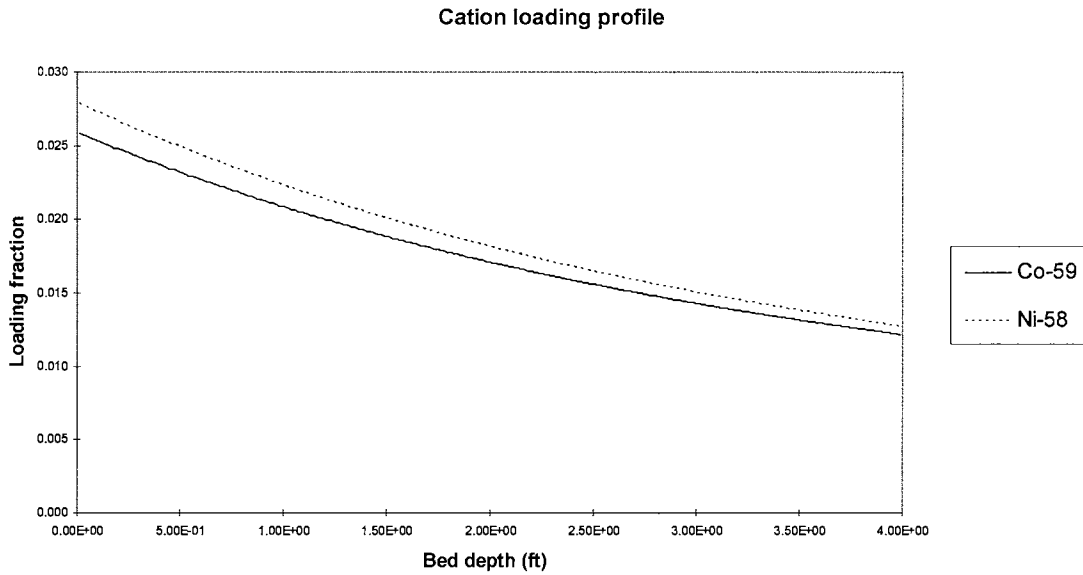


Figure V-4 Co-59 (stable) and Ni-58 (stable) loading profiles

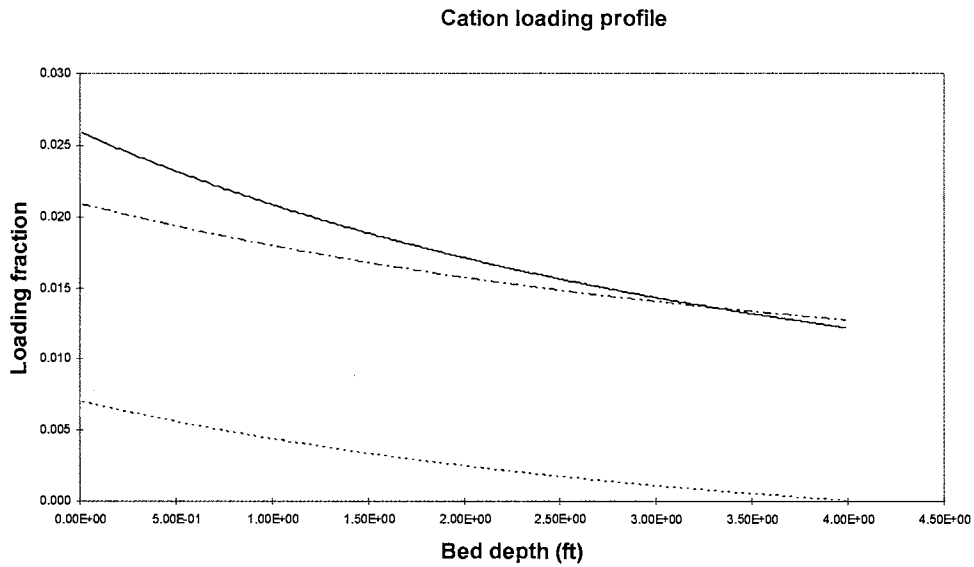


Figure V-5 Co-59 (stable) and Co-58 loading profiles

on model assumption, the two isotopes should have same selectivity. If there is no decay reaction, the two loading should have same profile. However, Co-58's T1/2 is 71.8 days. After 30 days of operation, a noticeable Ni-58 loading profile is shown in Figure V-5, which is the result of decay reaction.

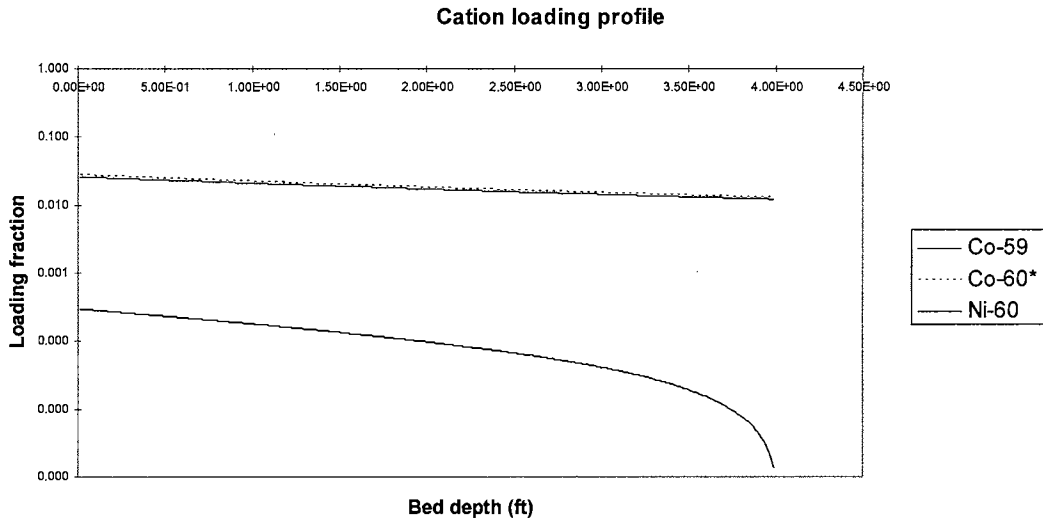


Figure V-6 Co-59 (stable) and Co-60 (Y axis use logarithmic scale) loading profiles

Figure V-6 shows loading profiles for Co-59 and Co-60 run. It shows the similar pattern as figure V-5 as the Co-60 decay reaction generated a Ni-60 loading profile. But Co-60's T1/2 is much longer (5.27 years). The Ni-60 loading is very low and can be observed only when the loading axle is re-scaled to logarithmic scale.

Conclusion

In this Chapter, 4 radioactive isotopes species are successfully integrated into MBIE simulator to calculate the radioactive isotopes loadings in some nuclear applications. The following conclusion can be made based on the results of above preliminary test,

- A New MBIE model has included the target radioactive species (Co-58, Co-60, Na-24, F-18)
- The model is capable of predicting loading profile and breakthrough of these radioactive species, the results show reasonable trends.
- Further validation of the results is needed by comparing with the field data.

CHAPTER VI

CONCLUSIONS AND RECOMMENDATIONS

Conclusions

A generalized mixed bed ion exchange column simulator has been developed. It is capable of handling an arbitrary number of species with any valence, especially multivalent dissociative species. The simulator was derived from fundamental continuity equations and uses correlations and constants to estimate system properties and parameters as a function of time and bed depth. The simulator is based on a rate type model that approximates the film diffusion controlled ion exchange behavior. New solving strategy is established and implemented successfully in the simulator to improve the stability and effectiveness of simulation.

According to the results described in Chapter 4, the following conclusions can be drawn:

1. The model satisfies the following critical criteria
 - The column material balance has been controlled at less 2% for most of the simulation with relatively big time distance step size (0.02X0.01). The mass balance error can be reduced dramatically by reducing step size. Comparison results shows than mass balance errors are more sensitive to distance step size than time step size.

- Infinite run time show effluent concentrations gradually approaching influent concentrations, and resin loadings approaching those predicted by mass action equilibrium with the feed.
- The loading, rate and solution ratio surfaces are continuous without oscillation or discontinuity when the simulation finished successfully with proper time and distance step-size. If the step-size is too big, usually big truncation error will be introduced which leads to discontinuity and finally stop the calculation.
- Ions elute chromatographically through the bed as a function of time according to valence, selectivity, and diffusivity criteria.

2. New solving strategy is implemented successfully to MBIE simulator. It has following advantage over the old version.

- Simulation runs more effective. With same time and distance step-size, new version run average about 19%-25% faster than old version. Simulation result is independent of algorithm when time and distance steps are in certain range.
- Simulator is more robust. New simulator can tolerate much bigger time and distance step-size than the old version. In general, 0.05X0.01 is recommended for new simulator. While old version need a step-size of 0.01X0.005 to achieve equal accuracy. This is useful improvement because a less accurate but less time consuming result can be achieved in a single simulation. The old version would require restart, which will bring the discontinuity.

3. Several radioactive isotopes species are integrated into simulator. The simulator can predict the radioactivity distribution by calculating the loading profile of isotopes. The

results are preliminary but show promise by meeting the model assumption and having reasonable trends.

There is limitation on the simplified assumption that radioactive decay is the only reaction for isotopes. No polynuclear aggregate species are assumed to be formed. This might not hold for complicated cases.

4. Other conclusions and findings

Weak electrolyte exchange has been approximated with ionic fluxes and in general has reasonable results. Molecular adsorption by direct protonation/hydrolysis is also modeled, but the results have not been benchmarked extensively with industry data to validate the parameters.

The model is also deficient in modeling molecular adsorption that does not use ion exchange capacity. In the Surry polisher evaluation calculation, ETA adsorption is calculated by an approximation with a direct protonation model, which does use the ion exchange capacity. Experimental data show that ETA, other amines, organics and particles might not use ion exchange capacity.

The model can export the ionic loading profiles at any time during the simulation, and may be restarted at any flow rate, concentration and loading profiles. This technique allows sequential runs that may be used to model step changes, pulse changes, and eventually real-time data.

Recommendations

Although the model was developed successfully, the following recommendations are required for a better model.

- More complete molecular mass transfer mechanism and data for weak electrolyte species — the current mass transfer rate is calculated mostly using only ionic fluxes. For some cases, Molecular adsorption by direct protonation/hydrolysis can be calculated. However, calculation accuracy of molecular mass transfer that does not use ion exchange capacity can be hindered due to lack of data.
- Complete modeling for the formation and adsorption of polynuclear aggregate species need to be done to improve the accuracy of radioactivity calculation.
- Model benchmarking — The performance of the model needs to be compared to industrial data, preferably with specific ion effluent histories. Additionally, a comparison of the resin exhaustion as a function of time should be performed.

Future work

The model still has a lot of room to improve and there are numerous applications that can utilize this simulator. Some ideas for future projects include:

Multiple beds in parallel—single mixed bed systems have been modeled effectively; however, most systems have several mixed beds in parallel with different regeneration/replacement schedules. It is possible to combine the effluents of different runs to simulate effluent histories.

Multiple beds in series—Most ultrapure water applications often have separate cation exchange bed and anion bed along with the mixed bed. The effluent concentrations from previous units are influent concentrations for downstream units, which are also variables. The current model is able to restart with new concentrations without great distortion of the loading profiles. But continuous variate feeding has never been tried.

Future efforts also include additional chemistry, such as precipitation and solubility relationships; as well as integrating the numerical solution techniques into three dimensional computational fluid dynamics programs.

REFERENCES

- Bulusu, R. Development of a column model to predict multicomponent mixed bed ion exchange breakthrough, MS Thesis(1994), Oklahoma State University, Stillwater, OK
- Boyd, G. E., Adamson, A. W., and Myers, Jr. L. S. The exchange adsorption of ions from aqueous solutions by organic zeolites II. Kinetics, J. Am. Chem. Soc., 69(1947), 2836-2848
- Copeland, J. P., C. L. Henderson, and J. M. Marchellow. Influence of resin selectivity on film-diffusion controlled ion exchange. AIChE J., 13(1967), 449-452
- Chowdiah, V. N. Liquid-film diffusion controlled ion-exchange modeling: Study of weak electrolyte mass transport and film mass-transfer kinetics, PhD. Dissertation(1996), Oklahoma State University, Stillwater, OK
- Chowdiah, Vikram N.; Foutch, Gary L.; Lee, Gang-Choon. Binary Liquid-Phase Mass Transport in Mixed-Bed Ion Exchange at Low Solute Concentration. Industrial & Engineering Chemistry Research (2003), 42(7), 1485-1494.
- Divekar, S. V., Foutch, G. L., and Haub, C. E.. Mixed-bed ion exchange at concentrations approaching the dissociation of water: Temperature effects. Ind. Eng. Chem. Res., 26(9)(1987), 1906-1909
- Dwivedi, P. N. and Upadhyay, S. N. Particle-Fluid Mass Transfer in Fixed and Fluidized Beds. Ind. Eng. Chem., Process Des. Dev., 16(2) (1977), 157-165
- Franzreb, M., Holl, W. H., and Sontheimer, H. Liquid-side mass transfer in multicomponent ion exchange: I. System without chemical reactions in the film, Reactive Polymer, 21(1993), 117-133
- Gear, C.W. (1971). Numerical Initial Value Problems in Ordinary Differential Equations. Englewood Cliffs, New Jersey, Prentice Hall.
- Gerald, C.F., Wheatley, P.O. (1989). Applied Numerical Analysis. Reading, Massachusetts, Addison-Wesley Publishing Company.

- Glaski, F.A., J.S. Dranoff (1963). Ion Exchange Kinetics: A Comparison of Models, AICHE J., 9, 426-431.
- Haub, C. E. and Foutch, G. L. Mixed-bed ion exchange at concentrations approaching the dissociation of Water: 2. Column model applications. Ind. Eng. Chem. Fund., 25(1986b), 381-385
- Helfferich, F. G. (1962). Ion Exchange. New York, McGraw Hill.
- Helfferich, F. G. Models and physical reality in ion-exchange kinetics. Reactive Polymers, 13(1990), 191-194
- Helfferich, F. G. Ion exchange kinetics: V. Ion exchange accompanied by reactions, J. Phys. Chem., 69(1965), 1178-1187
- Hussey, D. F. Development of a generalized multicomponent ion exchange reaction equilibrium model, MS Thesis(1996), Oklahoma State University, Stillwater, OK
- Jansen, M. L., Hofland, et al. (1996). Effect of pH and concentration on column dynamics of weak electrolyte ion exchange, AICHE. J., 42(7), 1925-1937
- Jansen, M. L., Straathof, et al. (1996). Rigorous Model for Ion Exchange Equilibria of Strong and Weak Electrolytes, AICHE. J., 42(7), 1911-1924
- Jansen, M. L., Houwers, et al. (1997). Effect of Dissociation Equilibria on Ion-exchange Processes of Weak Electrolytes, AICHE. J., 43(1), 73-82
- Kataoka, T., Sato, M., and Ueyama, K. (1968). Effective liquid phase diffusivity in ion exchange, J. Chem. Eng. Jpn., 1, 38-42
- Kataoka, T., M. Sato, and K. Ueyama (1971) Influence of a noncounterion valence on liquid phase diffusion in ion exchange, Kogyo Kagaku Zasshi, 74, 1052-1058
- Kataoka, T., H. Yoshida, and T. Yamada (1973) Liquid phase mass transfer in ion exchange based on the hydraulic radius model, J. Chem. Eng. Jpn., 6, 172-177
- Kataoka, T., H. Yoshida, and Y. Shidahara (1976). Liquid phase mass transfer in exchange accompanied by chemical reactions, J. Chem. Eng. Jpn., 9, 130-136
- Kataoka, T., Yoshida, H. and Uemura, T. (1987). Liquid-side ion exchange mass transfer in a ternary system. AICHE J., 33, 202-210
- Koon, J. H. and Kaufman, W. J. (1975). Ammonia removal from municipal wastewaters by ion exchange. J. Water Pollut. Control Fed., 47(3), 448-465

- Kunin, R. and Myers R. J. (1950). Ion Exchange Resins, John Wiley & Sons, New York
- Kunin, R. (1960). Elements of Ion Exchange, Reinhold Publishing Co., New York
- Lou, J. (1997). Modeling of Boron Sorption Equilibrium and Kinetics Studies of Ion Exchange with Boron Solution. M.S. Thesis, Oklahoma State University, Stillwater, OK.
- Newman, J. Electrochemical Systems, Prentice-Hall, Inc., Englewood Cliff, New Jersey, 1973.
- Noh, B. IL. (1992). Effects of step change in feed concentration and incomplete mixing of anion and cation resin on the performance of mixed-bed ion exchange. PhD dissertation, Oklahoma State University, Stillwater, OK
- Omatete, O. O., Vermeulen, T. and Clazie, R. N. (1980a). Column dynamics of ternary ion exchange. Part I. Diffusion and mass transfer relations. Chem. Eng. J., 19, 229-240
- Omatete, O. O., Vermeulen, T. and Clazie, R. N. (1980b). Column dynamics of ternary ion exchange. Part II. Diffusion and mass transfer relations. Chem. Eng. J., 19, 241-250
- Pamarthy, S. (1995). Development of a column model to predict silica breakthrough in a mixed-bed ion exchanger, MS Thesis, Oklahoma State University, Stillwater, ok
- Pate, K. T. (1991). Control of dissolved silica in High-purity systems. Ultrapure Water Journal, 8(4), 35-43
- Pleijel, H. (1910). Die Potentialdifferenz zwischen zwei elektrolytischen Lösungen, Z. Phys. Chem., 72, 1-37
- Pondugula, S. K. (1994). Mixed bed ion exchange modeling for divalent ions in a ternary system. MS Thesis, Oklahoma State University, Stillwater, OK
- Porteous, A. (1975). Saline Water Distillation Process, Longman, London
- Rahman, K. (1979). Film diffusion controlled kinetics in ternary ion exchange: Development of the basic equations. Chem. Eng. Res. Bull., 3, 27-30
- Reid, R. C., Parusnitz, J. M. and Sherwook, T. K. (1987). The Properties of Gases and Liquids, 4th Ed, McGraw-Hill, New York
- Rimstidt, J. D. and Barnes, H. L. (1980). The kinetics of silica-water reactions, Geochim. Cosmochim. Acta, 44, 1683-1699

- Sadler, M. A. (1993). Developments in the Production and Control of Ultrapure Water, Ion Exchange Processes: Advances and Applications, A. Dyer, M. J. Hudson, and P. A. Williams, Editors, The Royal Society of Chemistry, Cambridge, UK, 15-28
- Sahin, S. (1996). Mathematical model for adsorption of boric acid on a boron-specific ion exchanger. Bull. Chem. Soc. Jpn, 69, 1917-1920
- Samuelson, O. (1963). Ion Exchange Separations in Analytical Chemistry, John Wiley And Sons, New York
- Schlögl, R. (1954). Elektrodifffusion in freier Lösung und geladenen membranen, Z. Phys. Chem., 1, 305-339
- Schlögl, R. and Helfferich, F. (1957). Comment on the significance of diffusion potentials in ion exchange kinetics, J. Chem. Phys., 26, 5-7
- Smith, T. G. and J. S. Dranoff (1964). Film-diffusion controlled kinetics of binary ion exchange. Ind. Eng. Chem. Fundam., 3, 195-200
- Spiegler, K. S. and Laird, A. D. K. (1980). Principles of Desalination, Part B, pp577, Academic Press, New York
- Streat, M. (1995). The Waters were made sweet: Advances in ion exchange technology, Ind. Eng. Chem., 34, 2841-2848
- Stumm, W., Huper, H., and Champlin R. L. (1967). Formation of polysilicates as determined by coagulation effects, Environmental Sci. Tech., 1(3), 221-227
- Sunkavalli, S. K. V. (1996). Development of generalized equilibrium and rate models to predict ion exchange column performance, MS Thesis, Oklahoma State University, Stillwater, OK
- Thompson, H. S. (1850). On the adsorbent power of soils, Journal of the Royal Agricultural Society of England, 11, 68-74
- Turner, J. C. R., and Snowdon, C. B. (1968). Liquid-side mass transfer in ion exchange: An examination of the Nernst-Planck model, Chem. Eng. Sci., 23, 221-230
- Van Lier, J. A. (1960). The solubility of quartz, Drukkerij en Uitgeversmij v/h Kemink en Zoon n.v. Dom Plein, Utrecht, Netherlands
- Vermeulen, T. and Hiester, N. K. (1954). Ion exchange and adsorption column kinetics with uniform partial presaturation. J. Chem. Phys., 22, 96-101

- Wachinski, A. M. (1997). Environmental Ion Exchange: principles and design, CRC/Lewis Publisher, Boca Raton, Florida
- Wagner, J. D. and Dranoff, J. S. (1967). The kinetics of ion exchange accompanied by irreversible Reaction. III. Film diffusion controlled neutralization of a strong acid exchanger by a weak base. J. Phys. Chem., 71(13), 4551-4553
- Way, J. T. (1850). Influence of time on the absorptive properties of soils, Journal of the Royal Agricultural Society of England, 25, 313-379
- Wegmann, E. (1912). Ancient and modern water works, Eng. Rec., Vol. 65, June
- Wildhagen, G. R. S., Qassim, R. Y., Rajagopal, K. and Rahman, K. (1985). Effective liquid-phase diffusivity in ion exchange, Ind. Eng. Chem. Fundam., 24, 423-432
- Wong Y. and J. L. Niedawiecki (1982) A simplified model four multicomponent fixed bed adsorption, AIChE. Sym. Ser. 78 (219), 120-126
- Yoon, T. K. (1990). The effect of cation to anion ratio on mixed-bed ion exchange performance at ultra-low concentrations, PhD Thesis, Oklahoma State University, Stillwater, OK
- Yoshida, H. and Kataoka, T. (1987). Adsorption of amines on H⁺-form ion exchanger, Chem. Eng. Sci., 42(7), 1805-1814
- Yoshida, H., Shimizu, K. and Kataota, T. (1990). Adsorption of amine and paints on H-form resin from electrodeposition wastewater. AIChE. J. 36(12), 1815-1821
- Yu, Q. and Wang, N.-H. L. Computer simulations of the dynamics of multicomponent ion exchange and adsorption in fixed beds: Gradient-directed moving finite element method. Computers Chem. Eng., 13(8) (1989), 915-926
- Zecchini, E. J. (1990). Solutions to selected problems in multicomponent mixed bed ion exchange modeling, Ph.D. Dissertation, Oklahoma State University, Stillwater, OK
- Zecchini, E. J. and Foutch, G. L (1991). Mixed bed ion exchange modeling with amine form cation resins, Ind. Eng. Chem. Res., 30(8), 1886-1892
- Zoccolante, G. V. (1990). Produce ultrapure process water, Chem. Eng. Progress, 86(12), 69-72

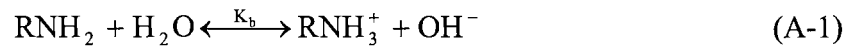
APPENDIX A

EQUILIBRIUM RELATIONSHIPS

I. DISSOCIATION EQUILIBRIUM FOR TYPE I DISSOCIATIVE SPECIES

Type I dissociative species has the characteristic of one-step dissociation equilibrium. Monovalent amine is a typical type I dissociative species. Chowdiah (1996) and Sunkavalli (1996) reviewed the dissociation equilibrium for monovalent amines. Based on their derivations, a generalized dissociation equilibrium for type I species can be generated.

As we know, for monovalent amines,



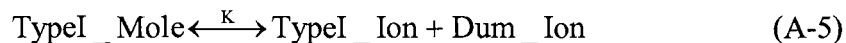
$$K_b = \frac{[\text{RNH}_3^+][\text{OH}^-]}{[\text{RNH}_2]} \quad (\text{A-2})$$

and for monovalent organic acids,



$$K_a = \frac{[\text{RCOO}^-][\text{H}^+]}{[\text{RCOOH}]} \quad (\text{A-4})$$

Eq (A-2) and Eq (A-4) are the same form. Therefore, we can generalize the dissociation equilibrium for the type I species as



$$K = \frac{[\text{TypeI_Ion}][\text{Dum_Ion}]}{[\text{TypeI_Mole}]} \quad (\text{A-6})$$

where, the Dum_Ion could be H⁺ or OH⁻, depending the type I species is acid or base.

If the total concentration of type I species is defined as

$$C_{\text{TDI}} = [\text{TypeI_Mole}] + [\text{TypeI_Ion}] \quad (\text{A-7})$$

then from equations (A-6) and (A-7), we can derive the relationship between [TypeI_Ion] and [Dum_Ion], that is

$$[\text{TypeI_Ion}] = \frac{K C_{\text{TDI}}}{K + [\text{Dum_Ion}]} \quad (\text{A-8})$$

This relation is used to eliminate [TypeI_Ion] from the charge balance equation, so that the charge balance equation contains only one unknown [Dum_Ion] for solving.

II. DISSOCIATION EQUILIBRIUM FOR TYPE II DISSOCIATIVE SPECIES

Type II dissociative species has the characteristics of two-step dissociation.

Carbonate is a typical type II dissociative species. Bulusu (1994) and Sunkavalli (1996) reviewed the water chemistry of carbonates, and the following dissociation equilibrium equations were presented:



$$K_1 = \frac{[\text{H}^+][\text{HCO}_3^-]}{[\text{H}_2\text{CO}_3^*]} \quad (\text{A-13})$$

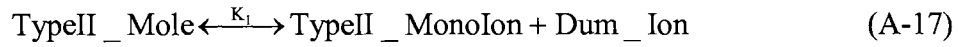
$$K_2 = \frac{[H^+][CO_3^{2-}]}{[HCO_3^-]} \quad (A-14)$$

$$K_w = [H^+][OH^-] \quad (A-15)$$

where

$$[H_2CO_3^*] = [H_2CO_3] + [CO_2] \quad (A-16)$$

In general, for the type II species, we can generalized its dissociation equilibrium as



$$K_1 = \frac{[\text{TypeII_MonoIon}][\text{Dum_Ion}]}{[\text{TypeII_Mole}]} \quad (A-19)$$

$$K_2 = \frac{[\text{TypeII_DiIon}][\text{Dum_Ion}]}{[\text{TypeII_MonoIon}]} \quad (A-20)$$

Where, Dum_Ion is a dummy ion, which could be H⁺ or OH⁻ depending the type II species is acid or base.

Given the total concentration C_{TDII} for the type II dissociative species, that is

$$C_{TDII} = [\text{TypeII_Mole}] + [\text{TypeII_MonoIon}] + [\text{TypeII_DiIon}] \quad (A-21)$$

the concentrations for monovalent ion [TypeII_MonoIon] and divalent Ion [TypeII_DiIon] can be determined.

From Eq (A-19) and Eq (A-20), we have

$$[\text{TypeII_Mole}] = \frac{[\text{Dum_Ion}][\text{TypeII_MonoIon}]}{K_1} \quad (A-22)$$

$$[\text{TypeII_DiIon}] = \frac{K_2[\text{TypeII_MonoIon}]}{[\text{Dum_Ion}]} \quad (\text{A-23})$$

Substituting Eq (A-22) and Eq (A-23) into Eq (A-21) would lead to

$$C_{\text{TDII}} = \frac{[\text{Dum_Ion}][\text{TypeII_MonoIon}]}{K_1} + [\text{TypeII_MonoIon}] + \frac{K_2[\text{TypeII_MonoIon}]}{[\text{Dum_Ion}]} \quad (\text{A-24})$$

Then the concentration of monovalent ion of typeII species can be written as:

$$[\text{TypeII_MonoIon}] = \frac{C_{\text{TDII}}}{X} \quad (\text{A-25})$$

where

$$X = \frac{[\text{Dum_Ion}]}{K_1} + \frac{K_2}{[\text{Dum_Ion}]} + 1 \quad (\text{A-26})$$

The expressions for the concentrations of other type II species can be written as:

$$[\text{TypeII_Mole}] = \frac{[\text{Dum_Ion}]C_{\text{TDII}}}{K_1 X} \quad (\text{A-27})$$

$$[\text{TypeII_DiIon}] = \frac{K_2 C_{\text{TDII}}}{[\text{Dum_Ion}]X} \quad (\text{A-28})$$

The above relations Eq (A-25), (A-27) and (A-28) are used to express the concentrations of various forms of type II species in terms of the concentration of Dummy ion (H^+ or OH^-) in the charge balance equation, so that only one unknown $[\text{Dum_Ion}]$ exists in the equation. Therefore, the charge balance equation can be solved.

III. DISSOCIATION EQUILIBRIUM FOR TYPE III DISSOCIATIVE SPECIES

Type III species has the characteristics of three-step dissociations. For instance, triprotic acid – phosphate is a typical type III dissociation species. The dissociation equilibrium relationships for phosphate (Fast, 1984) are

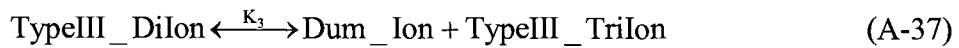
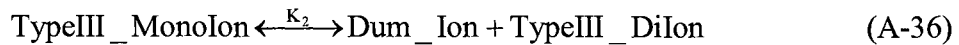
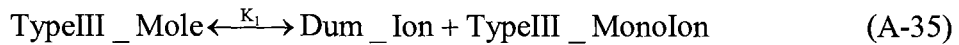


$$K_1 = \frac{[\text{H}^+][\text{H}_2\text{PO}_4^-]}{[\text{H}_3\text{PO}_4]} \quad (\text{A-32})$$

$$K_2 = \frac{[\text{H}^+][\text{HPO}_4^{2-}]}{[\text{H}_2\text{PO}_4^-]} \quad (\text{A-33})$$

$$K_3 = \frac{[\text{H}^+][\text{PO}_4^{3-}]}{[\text{HPO}_4^{2-}]} \quad (\text{A-34})$$

Based on the above, we can generalize the dissociation equilibriums for type III species as



$$K_1 = \frac{[\text{Dum_Ion}][\text{TypeIII_MonoIon}]}{[\text{TypeIII_Mole}]} \quad (\text{A-38})$$

$$K_2 = \frac{[\text{Dum_Ion}][\text{TypeIII_DiIon}]}{[\text{TypeIII_MonoIon}]} \quad (\text{A-39})$$

$$K_3 = \frac{[\text{Dum_Ion}][\text{TypeIII_TriIon}]}{[\text{TypeIII_DiIon}]} \quad (\text{A-40})$$

Where, Dum_Ion is a dummy ion, which could be H⁺ or OH⁻ depending the type III species is acid or base.

If the total concentration of type III species is given, that is

$$C_{\text{TDIII}} = [\text{TypeIII_Mole}] + [\text{TypeIII_MonoIon}] + [\text{TypeIII_DiIon}] \\ + [\text{TypeIII_TriIon}] \quad (\text{A-41})$$

then the concentration for each type III species can be determined.

From Eq (A-38), (A-39) and (A-40), we have

$$[\text{TypeIII_MonoIon}] = \frac{K_1[\text{TypeIII_Mole}]}{[\text{Dum_Ion}]} \quad (\text{A-42})$$

$$[\text{TypeIII_DiIon}] = \frac{K_2[\text{TypeIII_MonoIon}]}{[\text{Dum_Ion}]} = \frac{K_1K_2[\text{TypeIII_Mole}]}{[\text{Dum_Ion}]^2} \quad (\text{A-43})$$

$$[\text{TypeIII_TriIon}] = \frac{K_3[\text{TypeIII_DiIon}]}{[\text{Dum_Ion}]} = \frac{K_1K_2K_3[\text{TypeIII_Mole}]}{[\text{Dum_Ion}]^3} \quad (\text{A-44})$$

Substituting Eq (A-42), (A-43) and (A-44) into Eq (A-41) leads to

$$C_{\text{TDIII}} = [\text{TypeIII_Mole}] + \frac{K_1[\text{TypeIII_Mole}]}{[\text{Dum_Ion}]} + \frac{K_1K_2[\text{TypeIII_Mole}]}{[\text{Dum_Ion}]^2} \\ + \frac{K_1K_2K_3[\text{TypeIII_Mole}]}{[\text{Dum_Ion}]^3} \quad (\text{A-45})$$

Solve for [TypeIII_Mole], we get

$$[\text{TypeIII_Mole}] = \frac{C_{\text{TDIII}}}{X} \quad (\text{A-46})$$

where

$$X = 1 + \frac{K_1}{[\text{Dum_Ion}]} + \frac{K_1 K_2}{[\text{Dum_Ion}]^2} + \frac{K_1 K_2 K_3}{[\text{Dum_Ion}]^3} \quad (\text{A-47})$$

Therefore, the expressions for other ionic forms of type III species are

$$[\text{TypeIII_MonoIon}] = \frac{K_1}{[\text{Dum_Ion}]} \frac{C_{\text{TDIII}}}{X} \quad (\text{A-48})$$

$$[\text{TypeIII_DiIon}] = \frac{K_1 K_2}{[\text{Dum_Ion}]^2} \frac{C_{\text{TDIII}}}{X} \quad (\text{A-49})$$

$$[\text{TypeIII_TriIon}] = \frac{K_1 K_2 K_3}{[\text{Dum_Ion}]^3} \frac{C_{\text{TDIII}}}{X} \quad (\text{A-50})$$

Equations (A-48), (A-49) and (A-50) are used to express various forms of type III species in terms of the concentration of Dummy ion (H^+ or OH^-) in the charge balance equation, so that only one unknown exists in charge balance equation. This way the charge balance can be solved.

APPENDIX B

THE EFFLUENT CONCENTRATION PROFILES

Effluent concentration profile for KAPL Lithium column

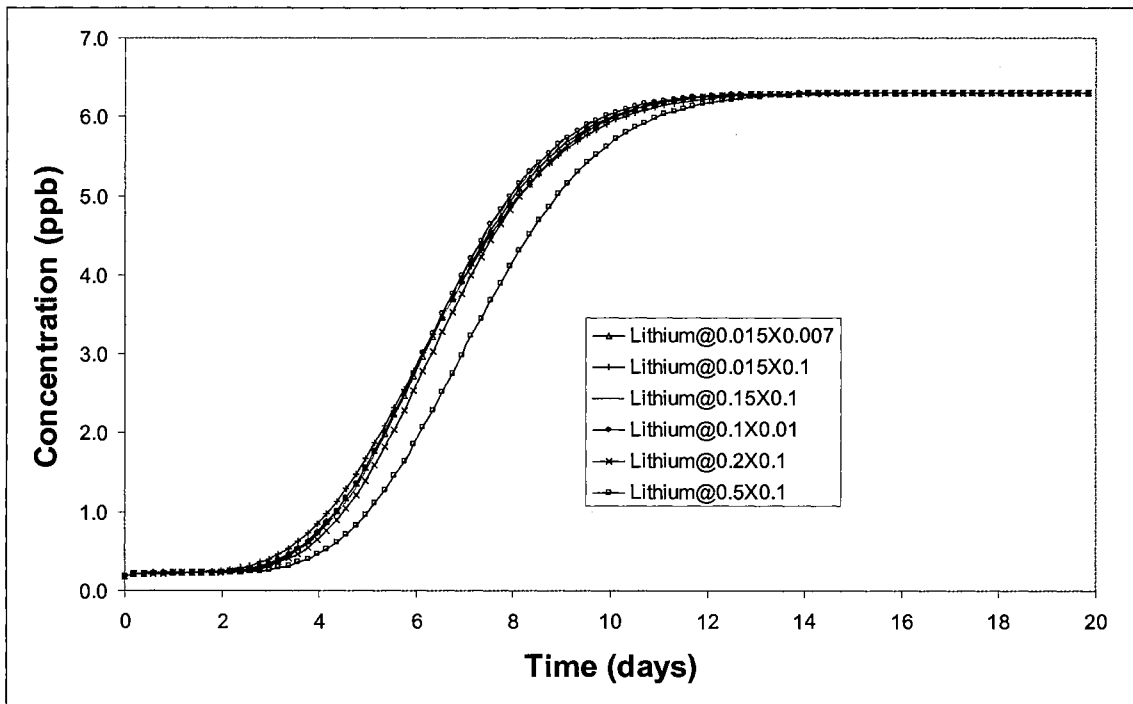


Figure B-1 Lithium breakthrough profile with various different time and distance steps

Effluent concentration profile for Dow regenerated column

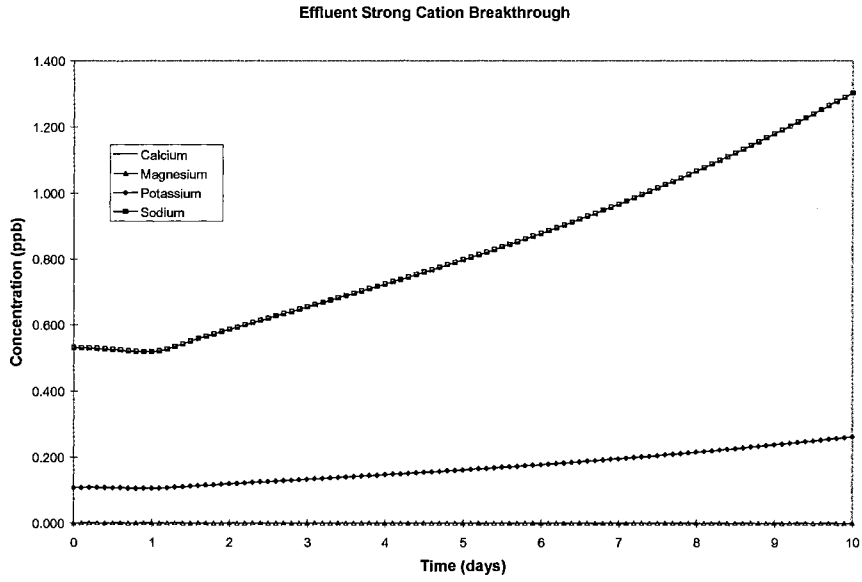


Figure B-2 Strong Cation breakthrough profile for Dow column @0.01X0.01

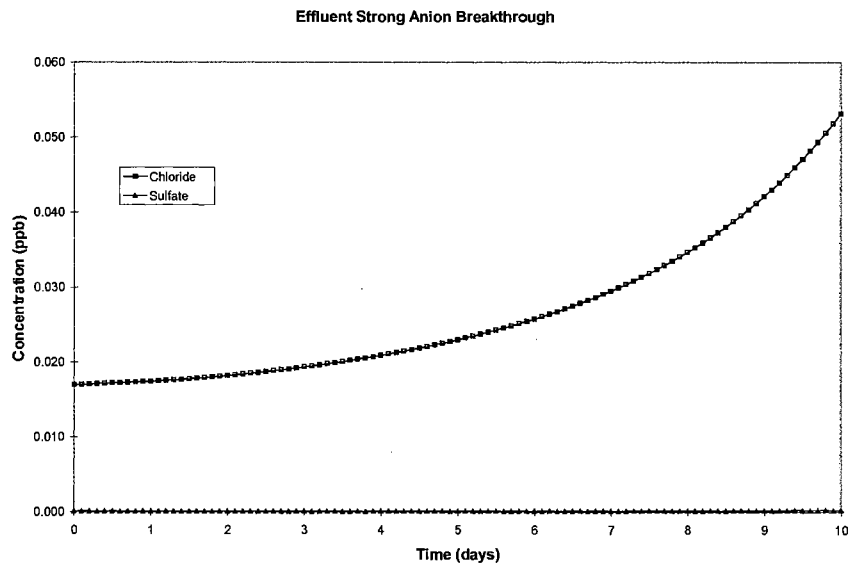


Figure B-3 Strong Anion breakthrough profile for Dow column @0.01X0.01

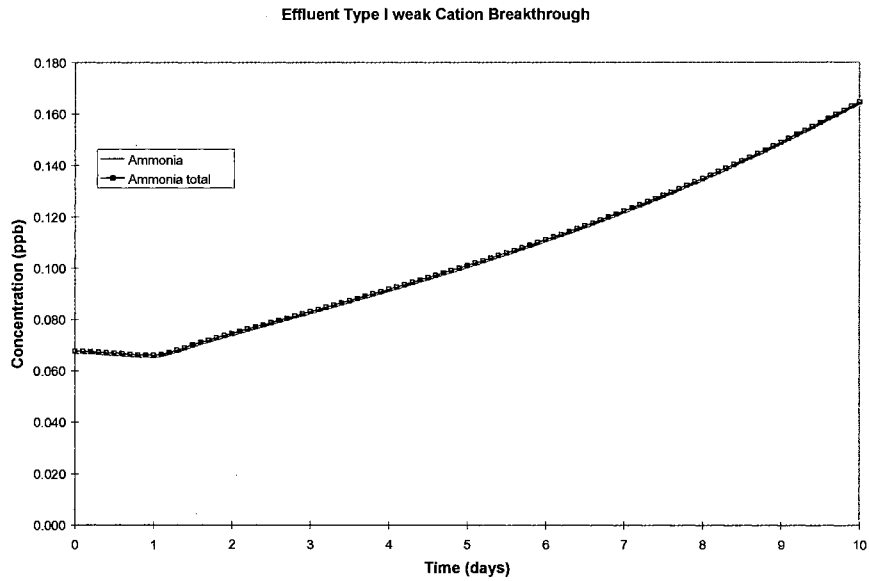


Figure B-4 Type I weak cation breakthrough profile for Dow column @0.01X0.01

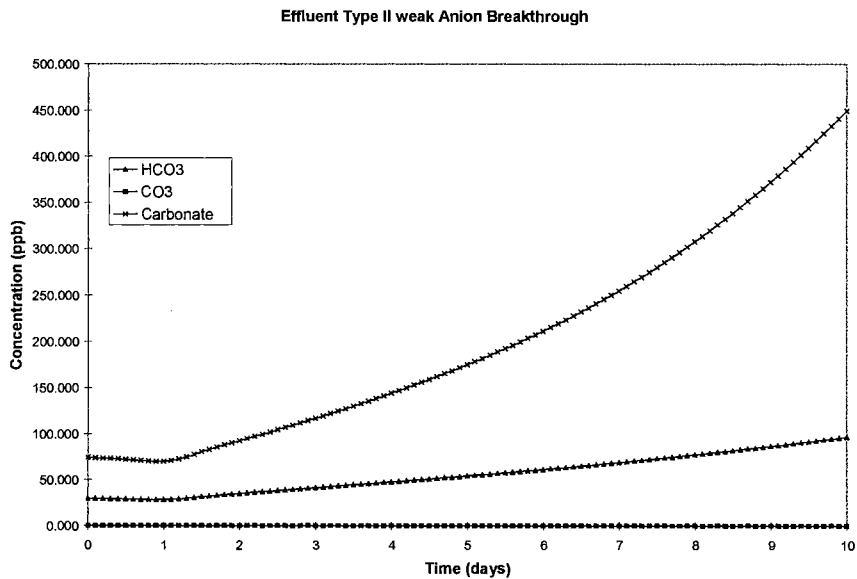


Figure B-5 Type I weak anion breakthrough profile for Dow column @0.01X0.01

Effluent concentration profile for Surry columns analysis

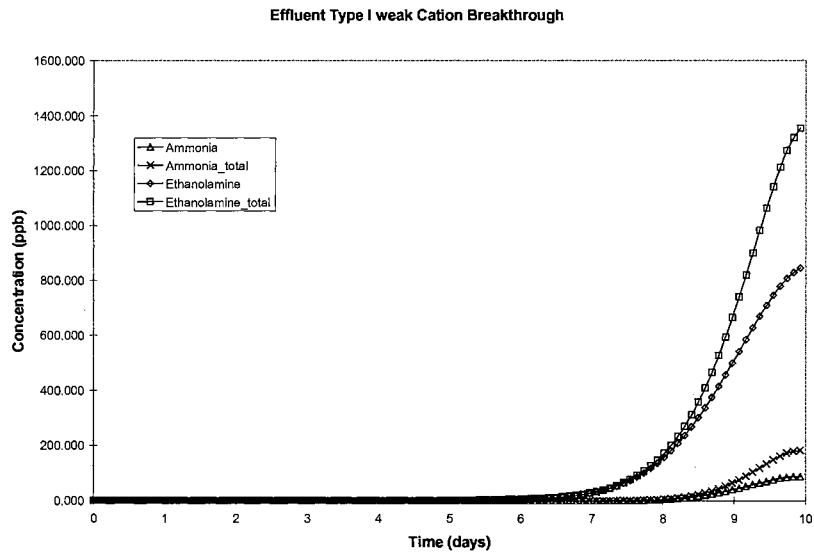


Figure B-6 Surry A column Effluent type I weak cation without adsorption

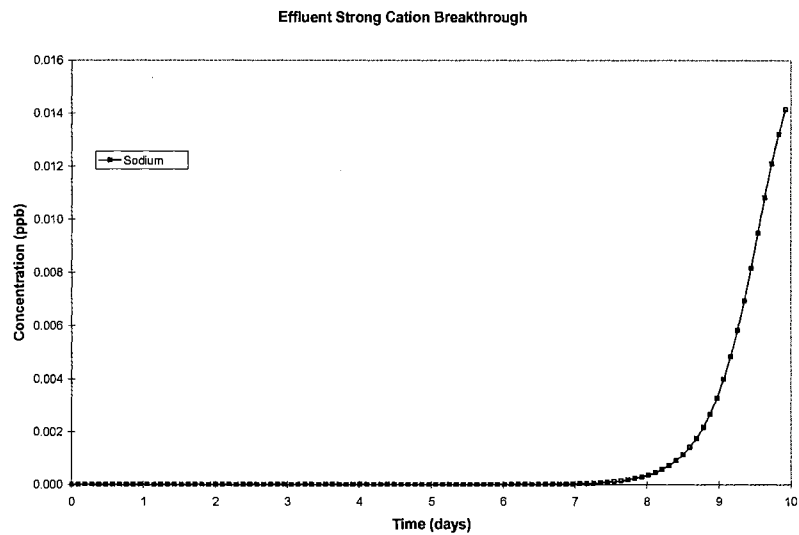


Figure B-7 Surry A column Effluent strong cation without adsorption

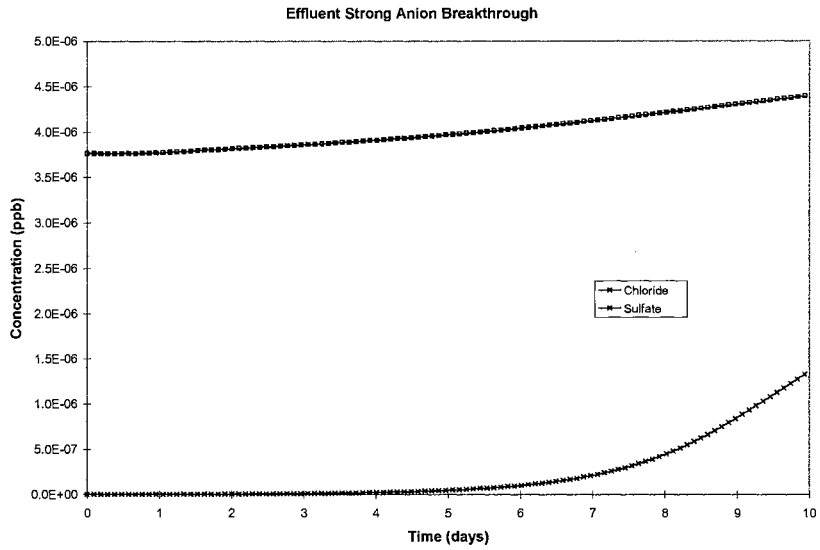


Figure B-8 Surry A Effluent strong anion without adsorption

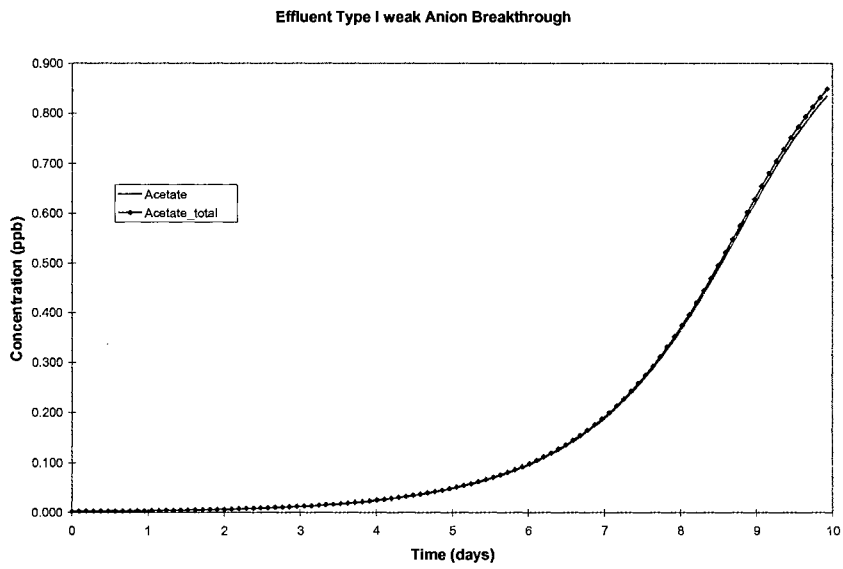


Figure B-9 Surry A Effluent type I weak anion without adsorption

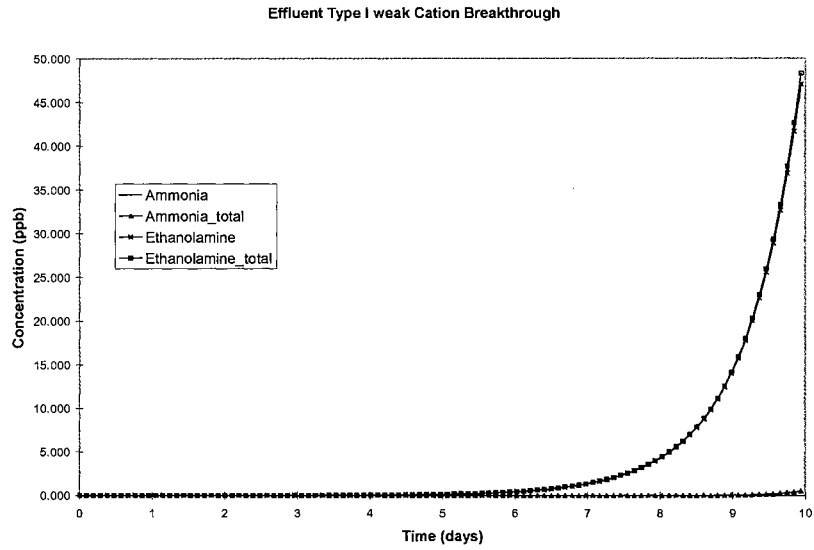


Figure B-10 Surry A Effluent type I weak cation with 30% ETA adsorption

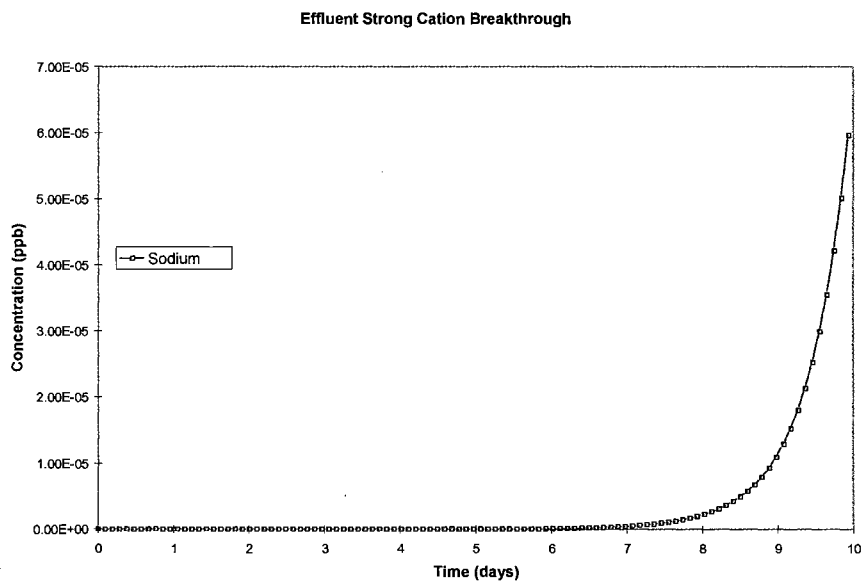


Figure B-11 Surry A Effluent strong cation with 30% ETA adsorption

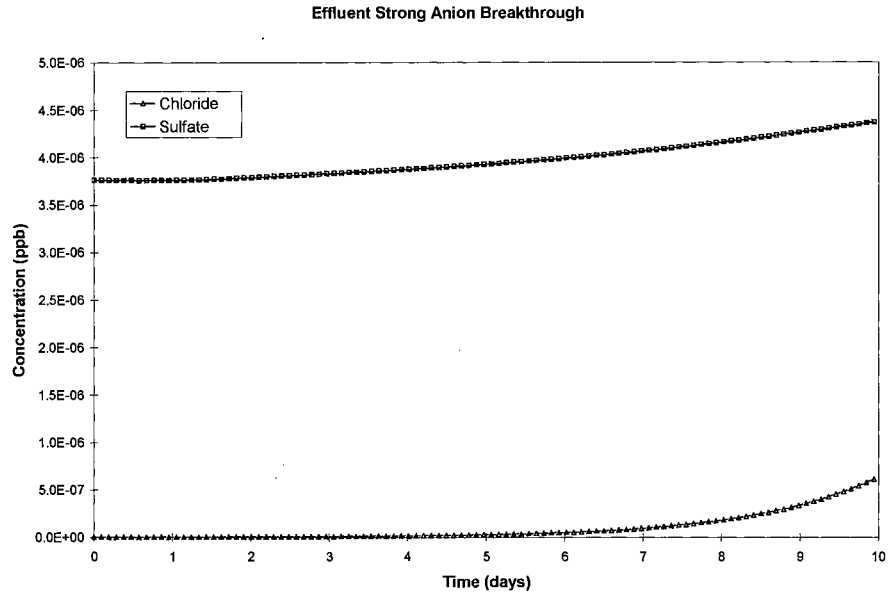


Figure B-12 Surry A Effluent strong anion with 30% ETA adsorption

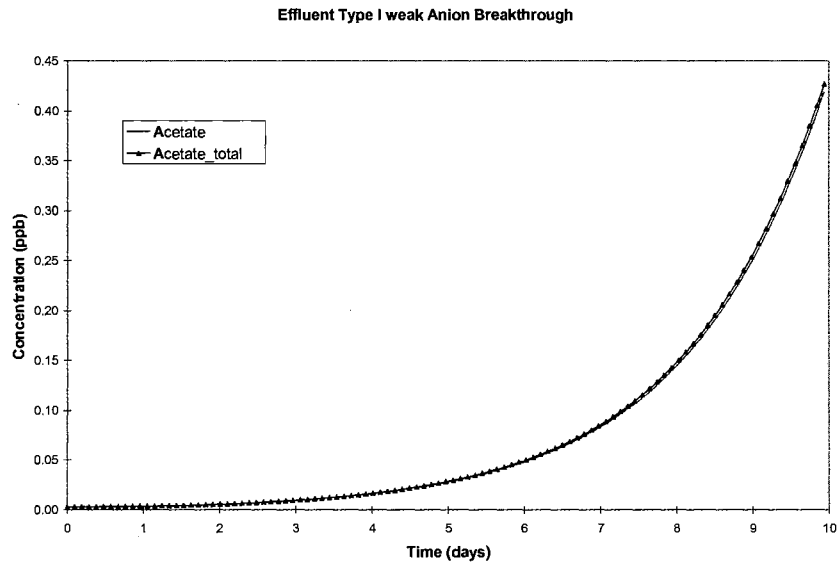


Figure B-13 Surry A Effluent type I weak anion with 30% ETA adsorption

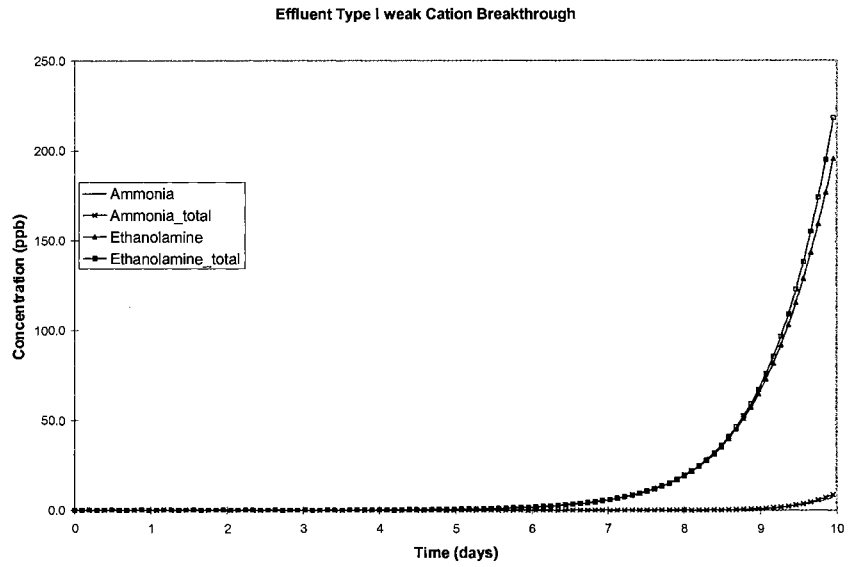


Figure B-14 Surry B column Effluent type I weak cation without adsorption

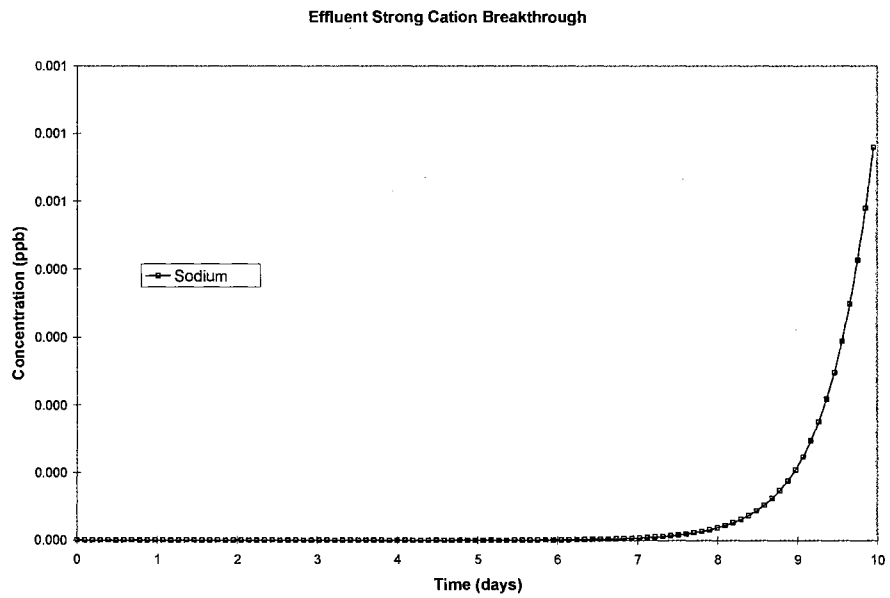


Figure B-15 Surry B column Effluent strong cation without adsorption

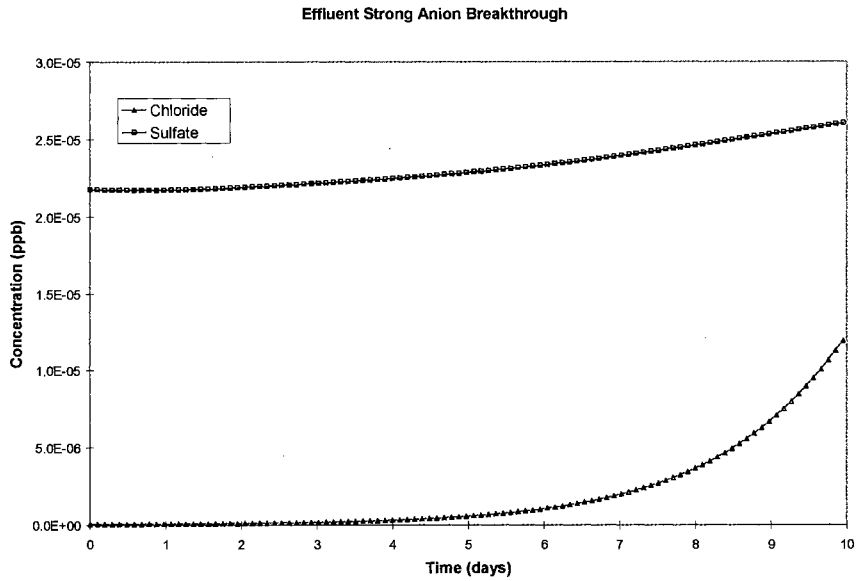


Figure B-16 Surry B Effluent strong anion without adsorption

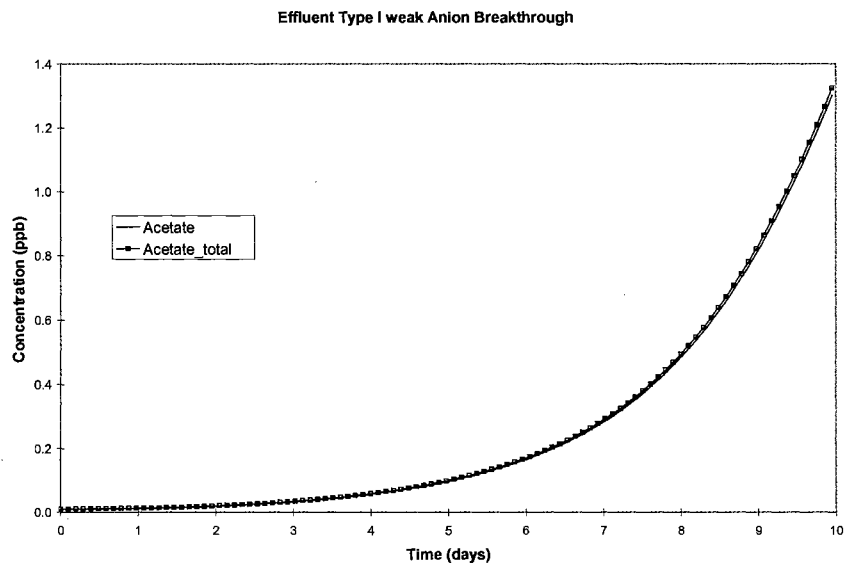


Figure B-17 Surry B Effluent type I weak anion without adsorption

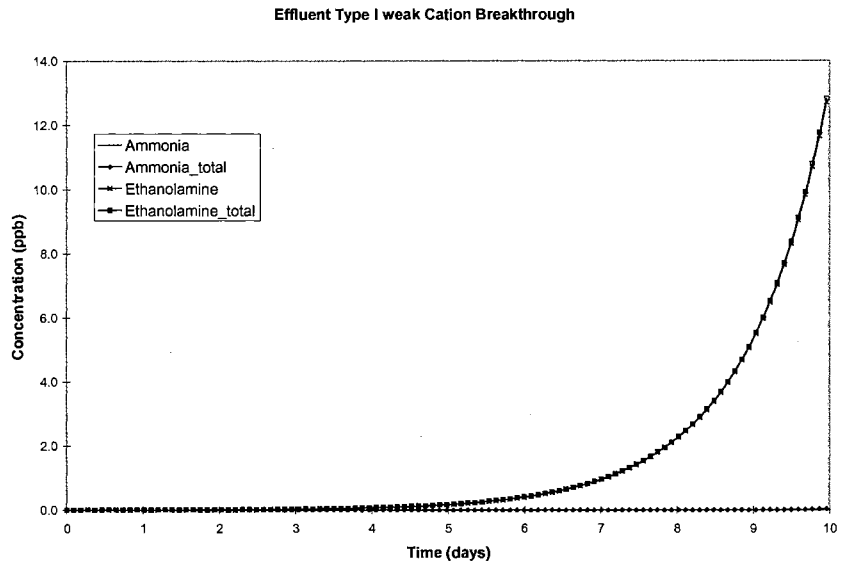


Figure B-18 Surry B Effluent type I weak cation with 30% ETA adsorption

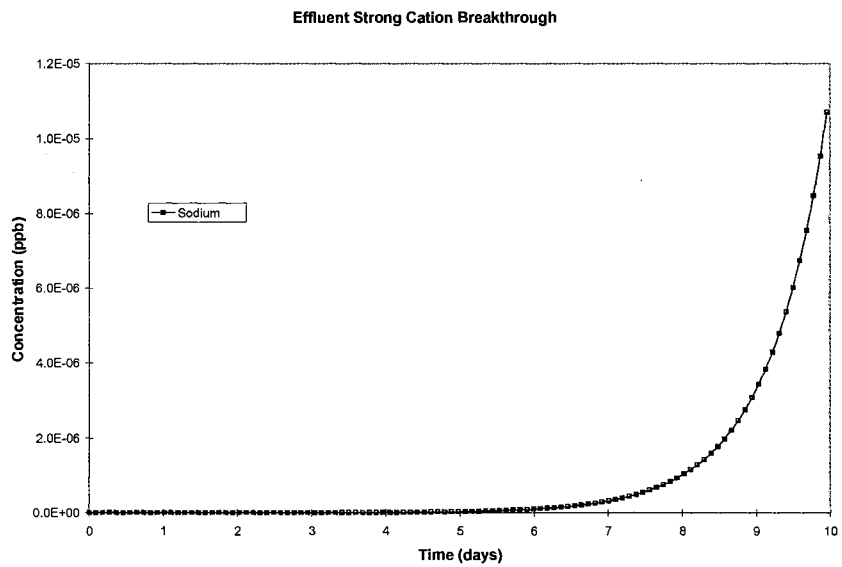


Figure B-19 Surry B Effluent strong cation with 30% ETA adsorption

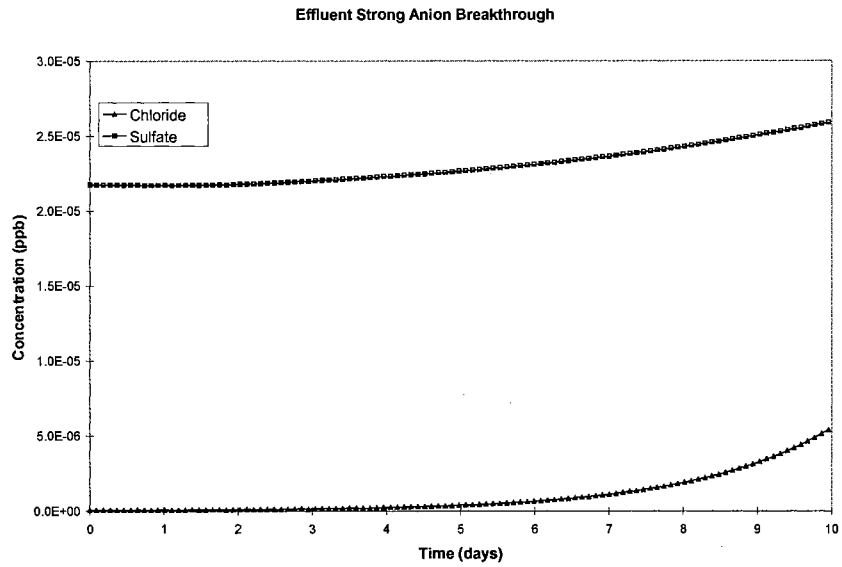


Figure B-20 Surry B Effluent strong anion with 30% ETA adsorption

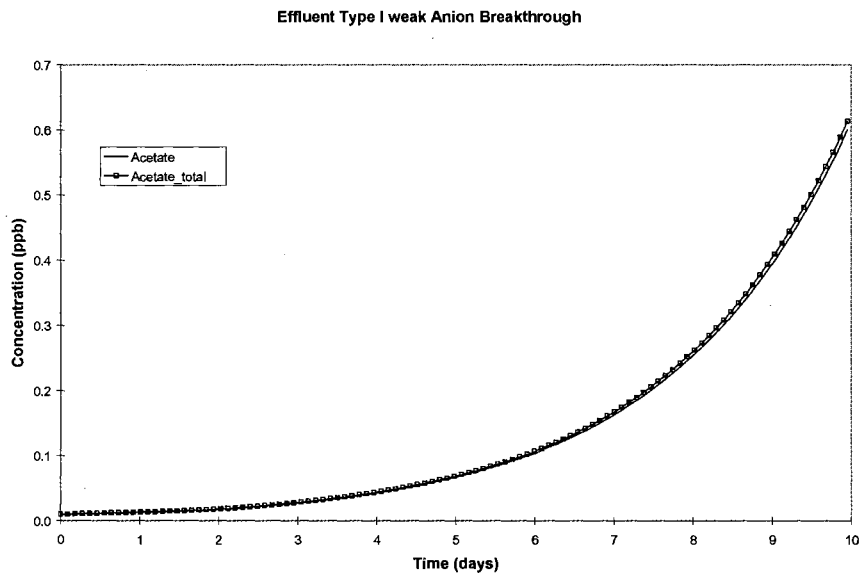


Figure B-21 Surry B Effluent type I weak anion with 30% ETA adsorption

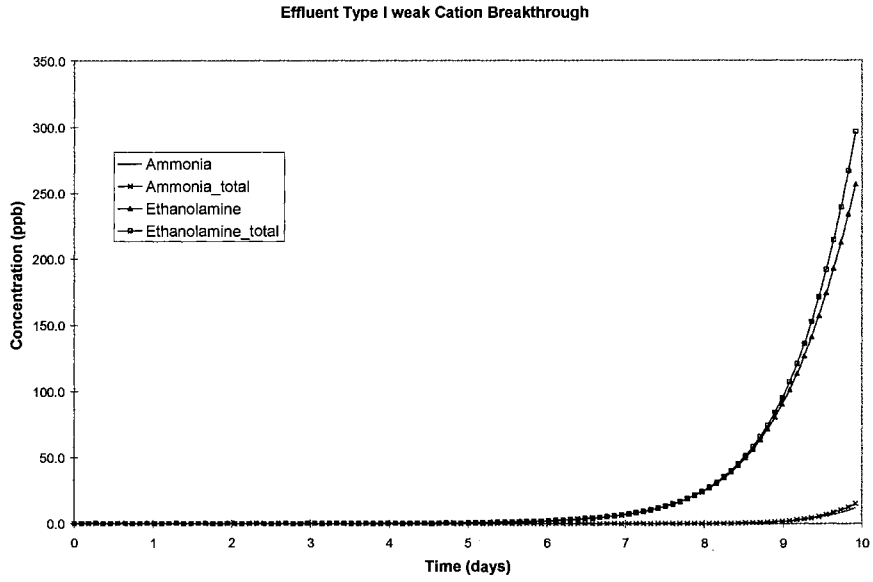


Figure B-22 Surry C column Effluent type I weak cation without adsorption

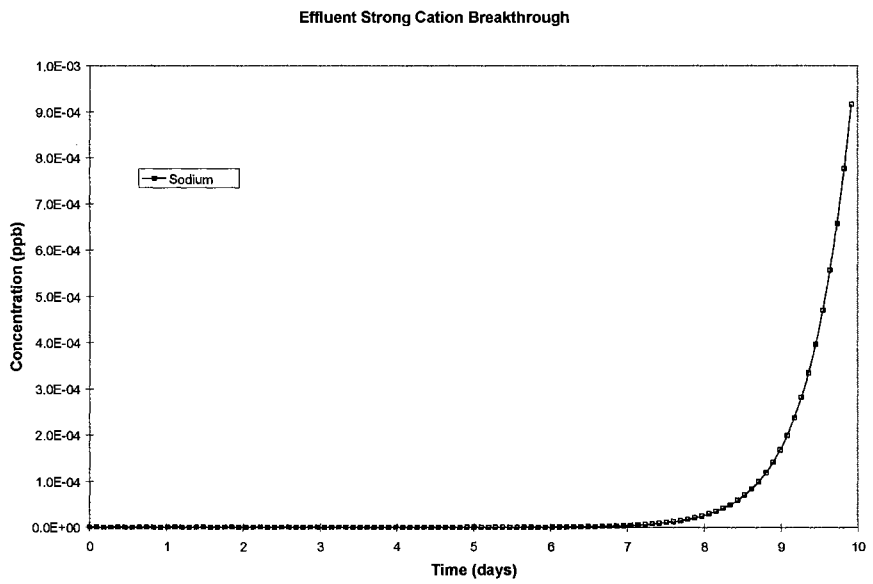


Figure B-23 Surry C column Effluent strong cation without adsorption

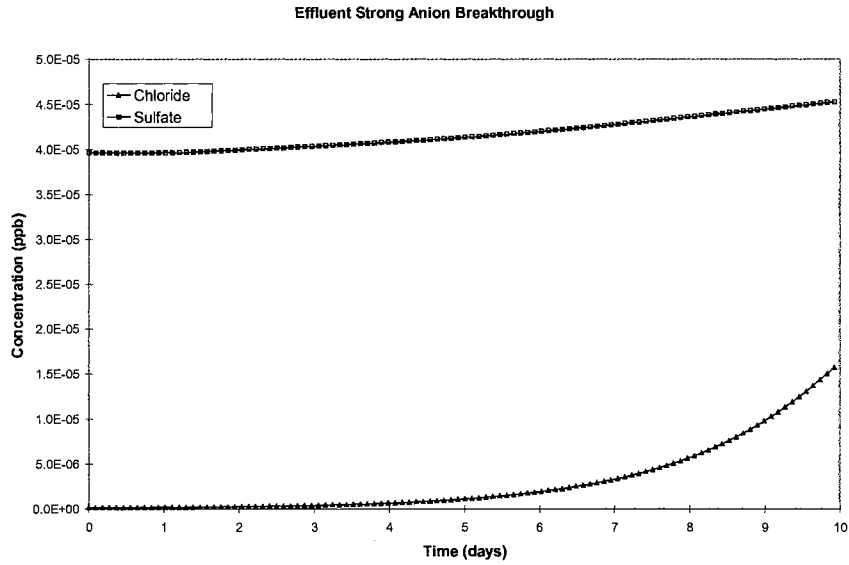


Figure B-24 Surry C Effluent strong anion without adsorption

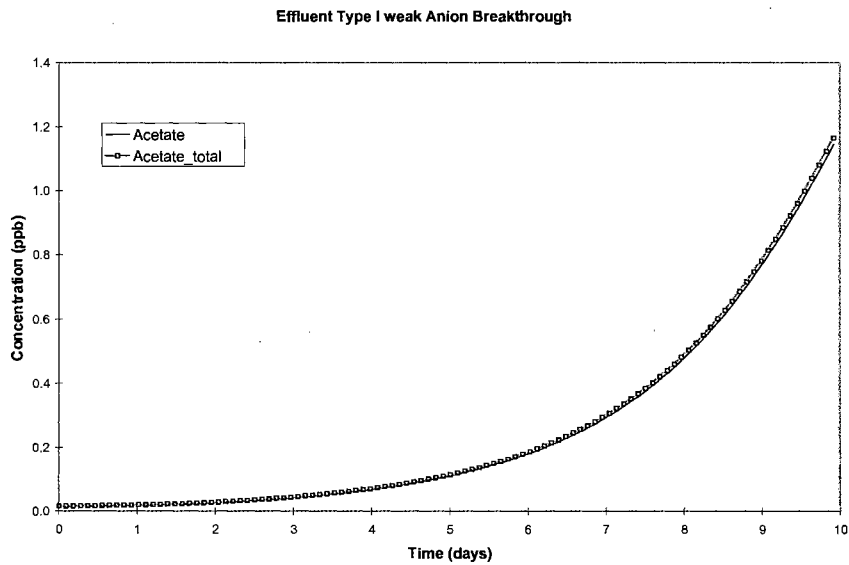


Figure B-25 Surry C Effluent type I weak anion without adsorption

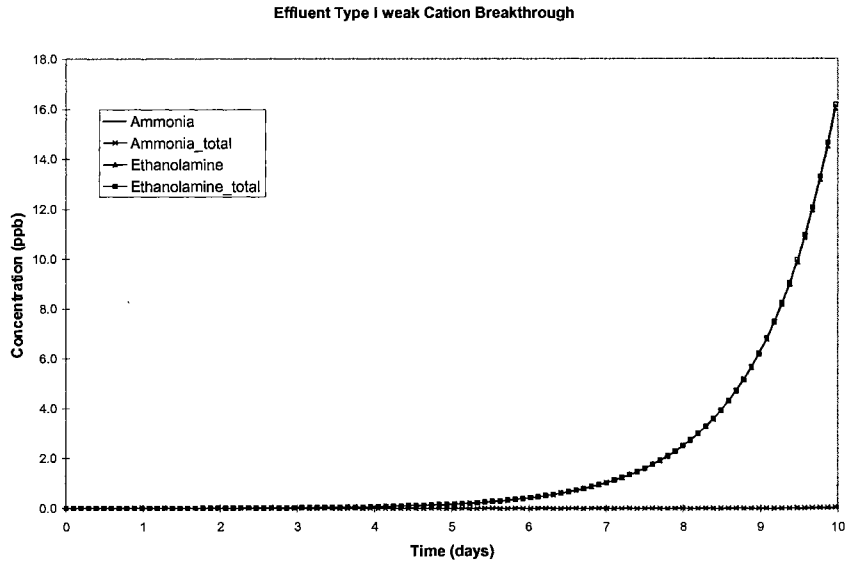


Figure B-26 Surry C Effluent type I weak cation with 30% ETA adsorption

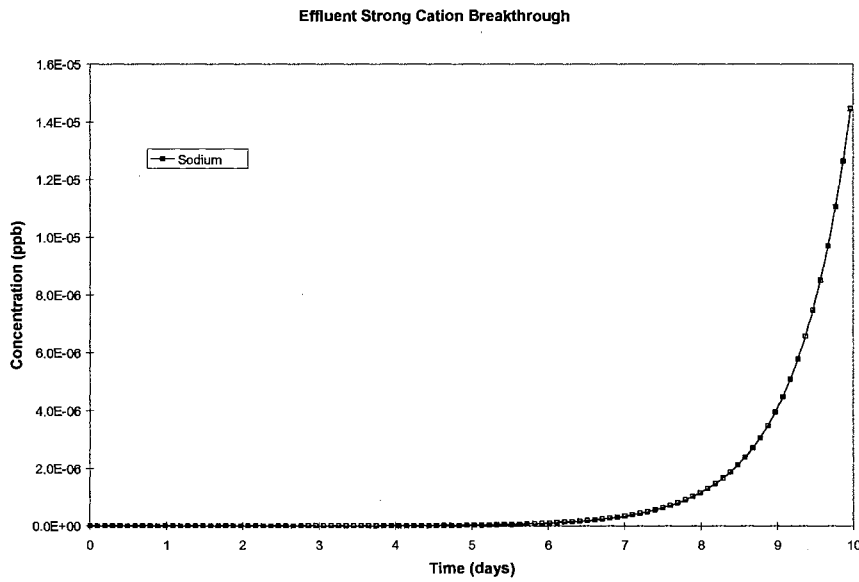


Figure B-27 Surry C Effluent strong cation with 30% ETA adsorption

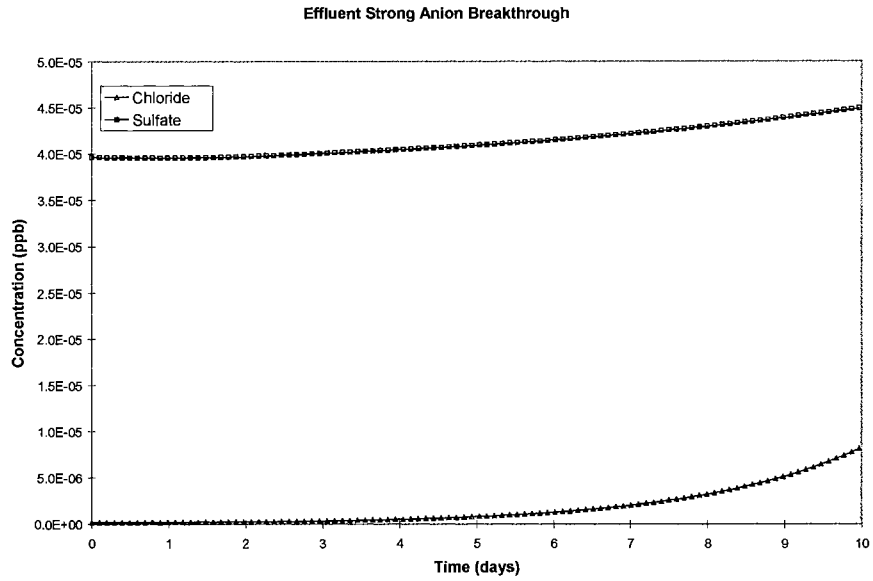


Figure B-28 Surry C Effluent strong anion with 30% ETA adsorption

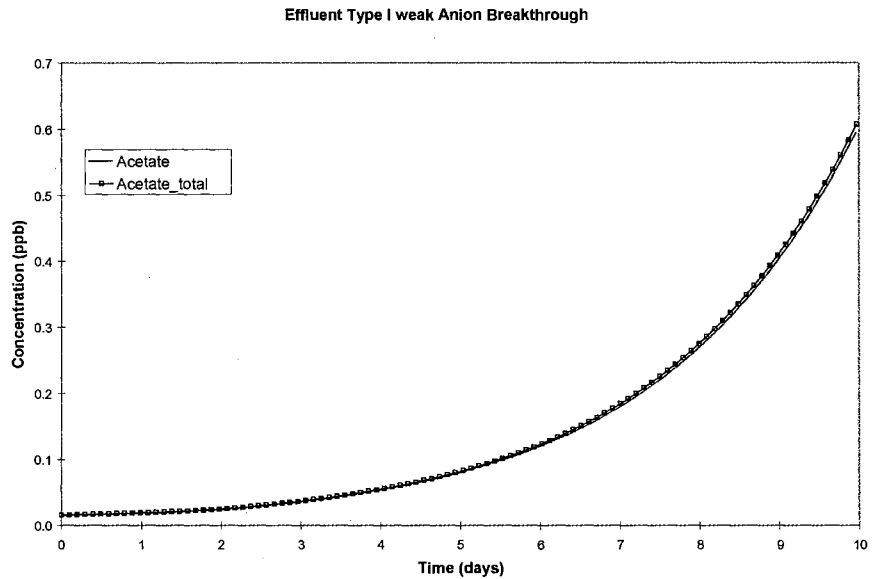


Figure B-29 Surry C Effluent type I weak anion with 30% ETA adsorption

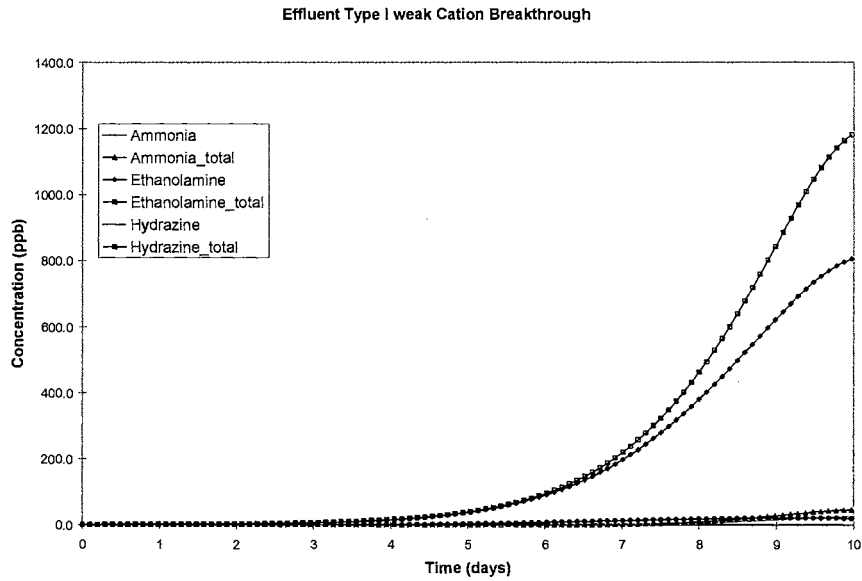


Figure B-30- Millstone column Effluent type I weak cation without adsorption

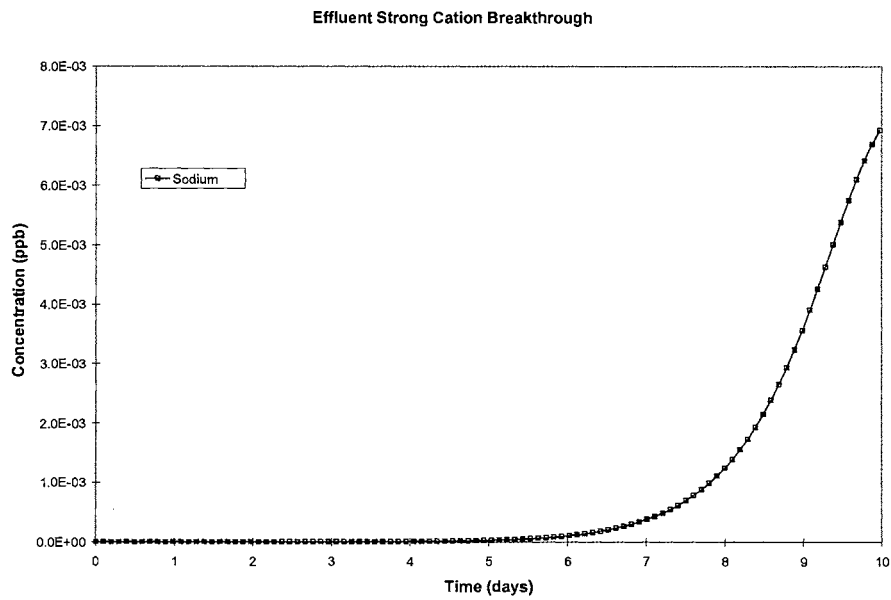


Figure B-31 Millstone column Effluent strong cation without adsorption

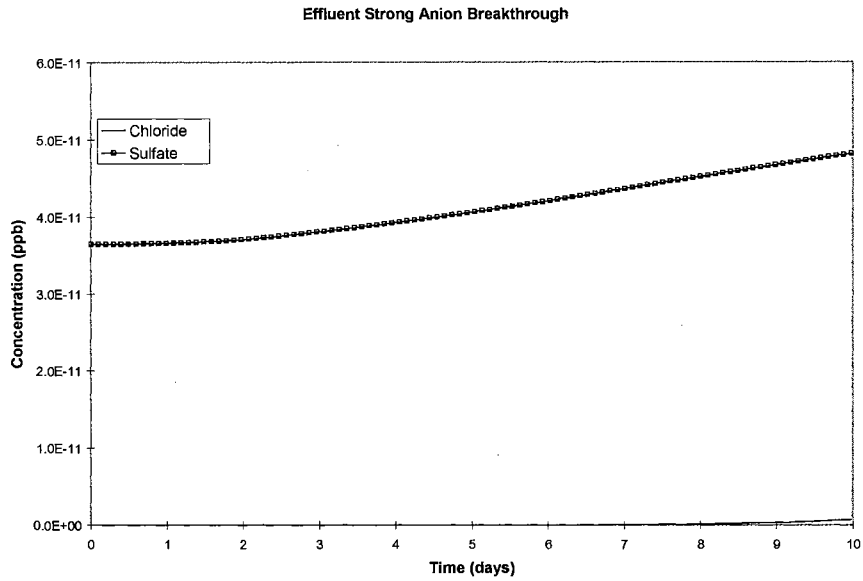


Figure B-32 Millstone Effluent strong anion without adsorption

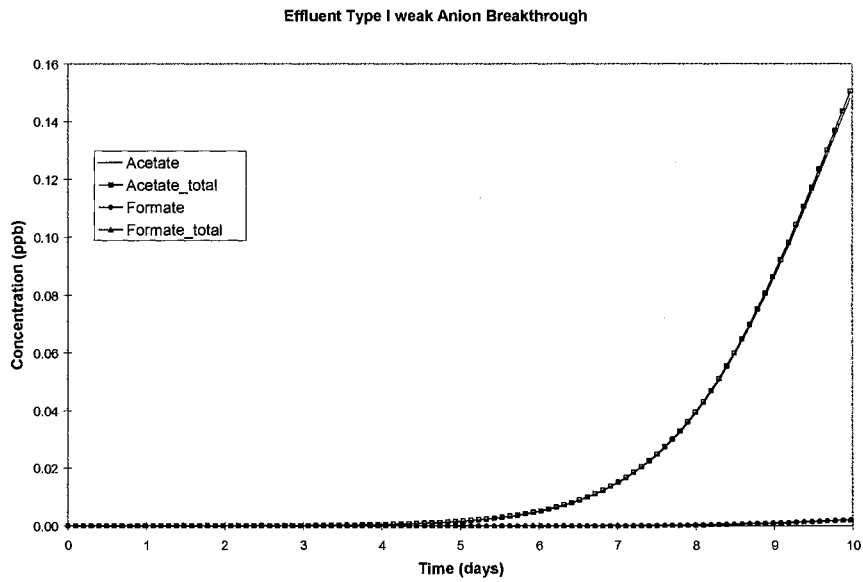


Figure B-33 Millstone Effluent type I weak anion without adsorption

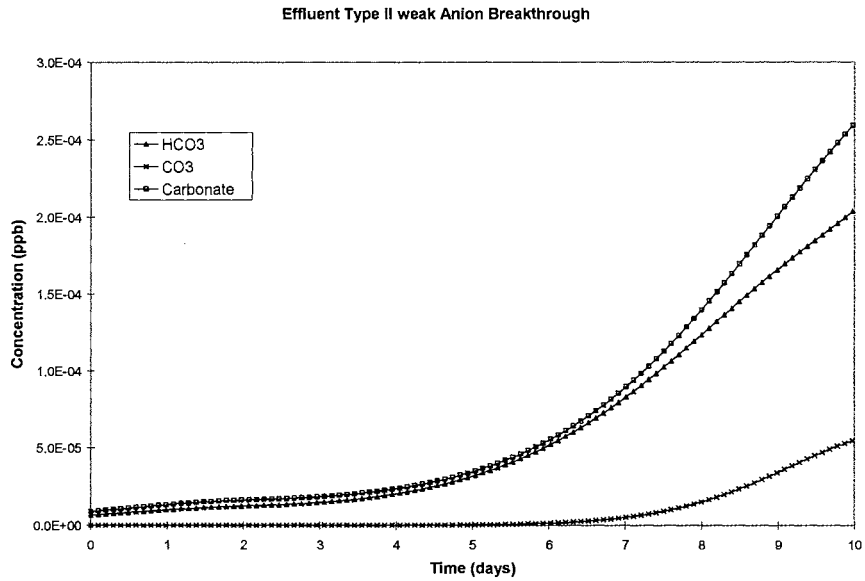


Figure B-34 Millstone Effluent type II weak anion without adsorption

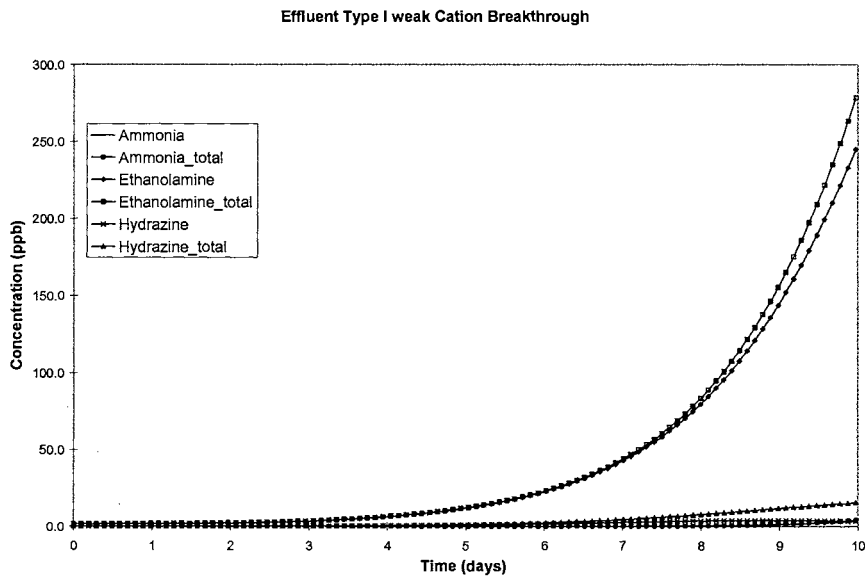


Figure B-35 Millstone Effluent type I weak cation with 30% ETA adsorption

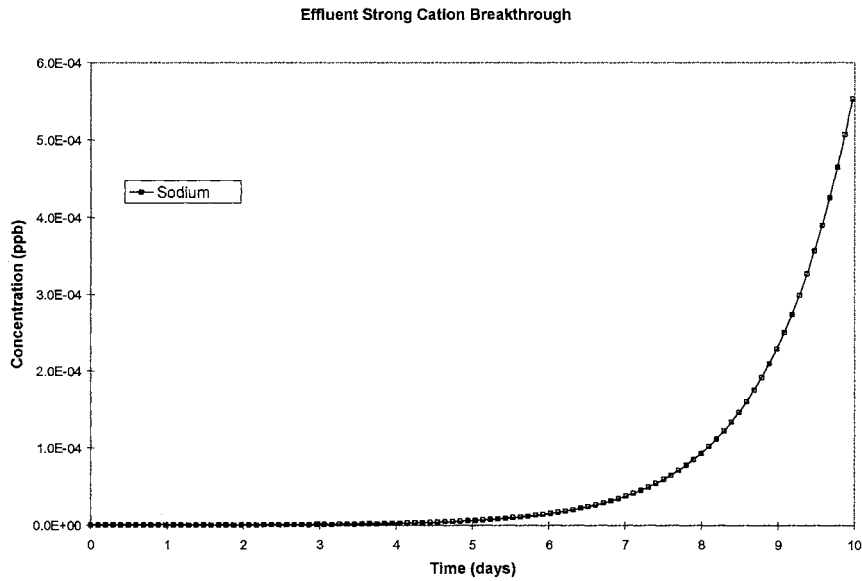


Figure B-36 Millstone Effluent strong cation with 30% ETA adsorption

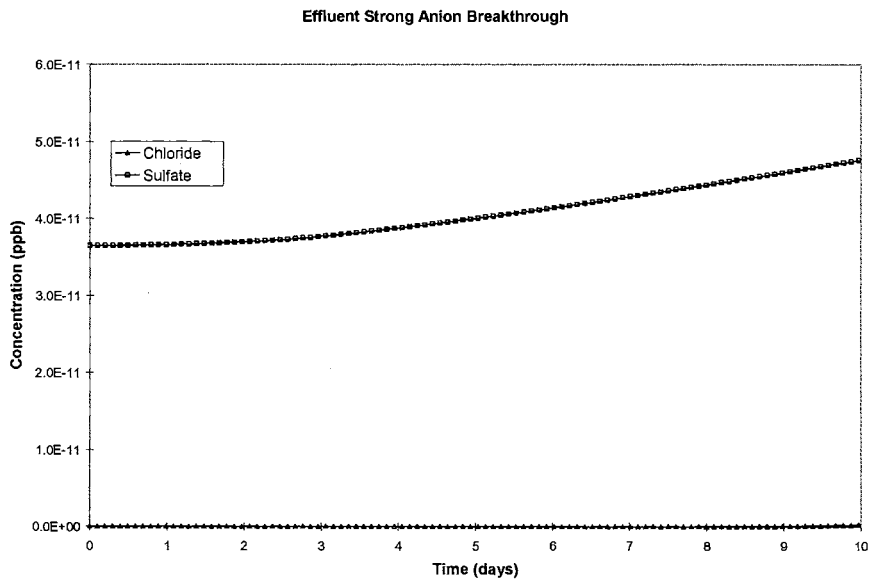


Figure B-37 Millstone C Effluent strong anion with 30% ETA adsorption

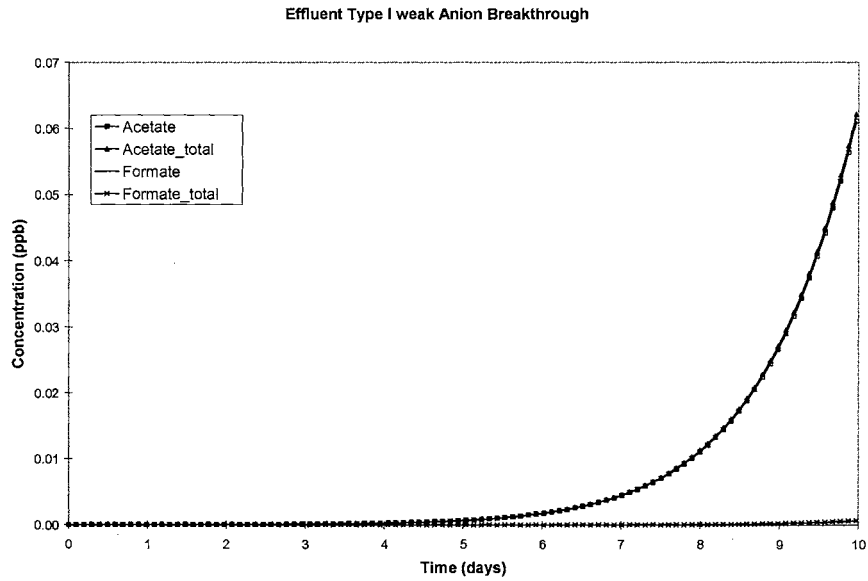


Figure B-38 Millstone Effluent type I weak anion with 30% ETA adsorption

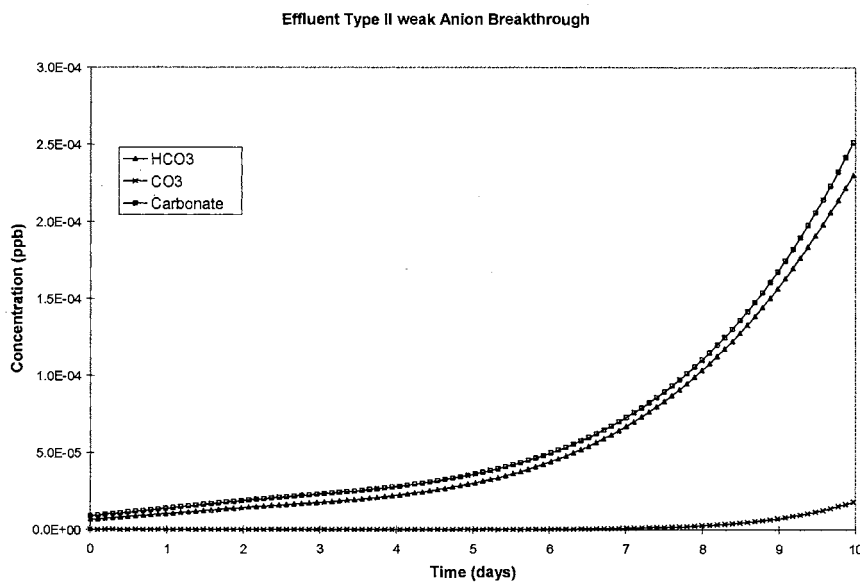


Figure B-39 Millstone Effluent type II weak anion with 30% ETA adsorption

APPENDIX C

COLUMN MATERIAL BALANCE

Neglecting axial and radial dispersion, the overall column material balance for species 'i' in an ion exchange column can be expressed as

$$\frac{\partial C_i^T}{\partial t} + \frac{u}{\varepsilon} \frac{\partial C_i^T}{\partial z} + (FR) \frac{1-\varepsilon}{\varepsilon} \frac{\partial q_i^T}{\partial t} = 0 \quad (C.1)$$

where u_s = superficial velocity, and ε = void fraction. The total constituent capacity is equal to the sum of the equivalents (or moles) of all sub-species.

$$C_i^T = \sum_{k=1}^n C_{ik} + C_i^* \quad (C.2)$$

where C_{ik} is the concentration of the ionic species of a constituent molecule in mol/l (equivalents are used in most of the solution calculations), k is the index of the ionic sub-species, n is the total number of ionic species of a dissociative species type (e.g. for carbonic acid, n equals two for bicarbonate and carbonate), C_i^* is the molecular species concentration, and C_i^f is the total constituent feed concentration.

The resin phase total constituent concentration has a similar definition

$$q_i^T = \sum_{k=1}^n q_{ik} + q_i^* \quad (C.3)$$

It is desirable to normalize the initial and final concentrations to 1.0 in numerical calculations because in cases where one constituent concentration is much greater or less

than another, the values of the numbers may be subject to round-off error. The following dimensionless variables are used to normalize the solution concentrations and resin concentrations to 1.0.

$$x_i = \frac{\sum_{k=1}^n C_{ik} + C_i^*}{C_i^f} = \frac{C_i^T}{C_i^f} \quad (C.4)$$

$$y_i = \frac{q_i^T}{q_i^e} = \frac{\sum_{k=1}^n q_{ik}}{q_i^e} \quad (C.5)$$

Dividing Equation (C.1) by $\frac{C_i^f q_i^e}{q_i^e}$ yields,

$$\frac{\partial x_i}{\partial t} + \frac{u}{\varepsilon} \frac{\partial x_i}{\partial z} + (FR) q_i^e \frac{1-\varepsilon}{\varepsilon} \frac{\partial y_i}{\partial t} = 0 \quad (C.6)$$

The method of characteristics is applied to reduce the order of the equations from third to second. The method combines the variation of one variable with two axes by selecting appropriate dimensionless variables and applying the chain rule. The dimensionless time and distance are defined as,

$$\tau_i = \frac{k_i C_i^f}{q_i^e \varepsilon} \left(t - \frac{z\varepsilon}{u} \right) \quad (C.7)$$

$$\xi_i = \frac{k_i (1-\varepsilon) z}{d_{p,i} u} \quad (C.8)$$

k_i is the non-ionic mass transfer coefficient for species i , $d_{p,i}$ is the particle diameter for the exchanging species resin type, q_i^e is the equilibrium resin capacity and C_i^f is the total cationic feed concentration. The above expressions are differentiated with respect to time and distance respectively to yield:

$$\frac{\partial \xi_i}{\partial z} = \frac{k_i(1-\varepsilon)}{u_s d_{p,i}} \quad (C.9)$$

$$\frac{\partial \tau_i}{\partial z} = \frac{-k_i C_i^f \varepsilon}{d_{p,i} q_i^e u_s} \quad (C.10)$$

$$\frac{\partial \xi_i}{\partial t} = 0 \quad (C.11)$$

$$\frac{\partial \tau_i}{\partial t} = \frac{k_i C_i^f}{d_{p,i} q_i^e} \quad (C.12)$$

Applying the chain rule to each differential term of Equation (C.1) changes the integration axes.

$$\frac{\partial x_i}{\partial z} = \frac{\partial x_i}{\partial \xi_i} \frac{\partial \xi_i}{\partial z} + \frac{\partial x_i}{\partial \tau_i} \frac{\partial \tau_i}{\partial z} \quad (C.13)$$

$$\frac{\partial x_i}{\partial t} = \frac{\partial x_i}{\partial \xi_i} \frac{\partial \xi_i}{\partial t} + \frac{\partial x_i}{\partial \tau_i} \frac{\partial \tau_i}{\partial t} \quad (C.14)$$

$$\frac{\partial y_i}{\partial t} = \frac{\partial y_i}{\partial \xi_i} \frac{\partial \xi_i}{\partial t} + \frac{\partial y_i}{\partial \tau_i} \frac{\partial \tau_i}{\partial t} \quad (C.15)$$

Inserting Equations (C.9) to (C.12) into Equations (C.13) to (C.15)

$$\frac{\partial x_i}{\partial t} = \frac{\partial x_i}{\partial \xi} (0) + \frac{\partial x_i}{\partial \tau} \left(\frac{k_i C_i^f}{d_{p,i} q_i^e} \right) = \frac{k_i C_i^f}{d_{p,i} q_i^e} \frac{\partial x_i}{\partial \tau} \quad (C.16)$$

$$\frac{\partial x_i}{\partial z} = \frac{\partial x_i}{\partial \xi_i} \left(\frac{k_i(1-\varepsilon)}{u_s d_{p,i}} \right) + \frac{\partial x_i}{\partial \tau_i} \left(\frac{-k_i C_i^f \varepsilon}{d_{p,i} q_i^e u_s} \right) \quad (C.17)$$

$$\frac{\partial y_i}{\partial t} = \frac{\partial y_i}{\partial \xi_i} (0) + \frac{\partial y_i}{\partial \tau} \left(\frac{k_i C_i^f}{d_{p,i} q_i^e} \right) \quad (C.18)$$

Substituting Equations (C.16) to (C.18) into Equation (C.6),

$$\left[\frac{k_i C_i^f}{d_{p,i} q_i^e} \frac{\partial x}{\partial t} \right] + \frac{u_s}{\varepsilon} \left[\frac{\partial x_i}{\partial \xi_i} \left(\frac{k_i (1-\varepsilon)}{u_s d_{p,i}} \right) + \frac{\partial x_i}{\partial \tau_i} \left(\frac{-k_i C_i^f \varepsilon}{d_{p,i} q_i^e u_s} \right) \right] +$$

$$(FR) q_i^e \frac{(1-\varepsilon)}{\varepsilon} \left[\frac{\partial y_i}{\partial \tau} \frac{k_i C_i^f}{d_{p,i} q_i^e} \right] = 0 \quad (C.19)$$

Equation (C.19) collapses to,

$$\frac{\partial x_i}{\partial \xi_i} + (FR) \frac{\partial y_i}{\partial \tau_i} = 0 \quad (C.20)$$

This expression is still a partial differential equation, but it is now only a second order equation. If the two terms are equated by subtracting the change in resin loading differential from both sides, the observation is made that at any given point in time and space the two differentials are equal to a constant that varies with time and space.

$$\frac{\partial x_i}{\partial \xi_i} = -(FR) \frac{\partial y_i}{\partial \tau_i} = R_i^T(\tau, \xi) \quad (C.21)$$

The constant is the constituent exchange rate. Analytical solutions exist when the exchange rate does not vary with time and space; however, in our system the only times the rates are constant is when they are at equilibrium with the resin, and the value is zero.

Each element of the differential equation system represents a constituent; and each constituent has its own dimensionless time and distance variable definitions. The elements of the differential equation system are changed to common reference axes by choosing a reference constituent and applying the chain rule to each element of the equation system. The reference constituent is the constituent with the largest value of τ , and the reference constituent is denoted with the subscript 'r.'

$$\frac{\partial x_i}{\partial \xi_r} = \frac{\partial x_i}{\partial \xi_i} \frac{\partial \xi_i}{\partial \xi_r} \quad (C.22)$$

$$\frac{\partial y_i}{\partial \tau_r} = \frac{\partial y_i}{\partial \tau_i} \frac{\partial \tau_i}{\partial \tau_r} \quad (\text{C.23})$$

Inserting the chain rule definitions, Equations (C.9) through (C.12) into Equations (C.22) and (C.23)

$$\frac{\partial \xi_i}{\partial \xi_r} = \frac{\xi_i}{\xi_r} = \frac{\frac{k_i(1-\varepsilon)z}{u_s d_{p,i}}}{\frac{k_r(1-\varepsilon)z}{u_s d_{p,r}}} = \frac{k_i d_{p,r}}{k_r d_{p,i}} \quad (\text{C.24})$$

$$\frac{\partial \tau_i}{\partial \tau_r} = \frac{\tau_i}{\tau_r} = \frac{\frac{k_i C_i^f}{d_{p,i} q_i^e} \left(t - \frac{z}{u_s} \varepsilon \right)}{\frac{k_r C_r^f}{d_{p,r} q_r^e} \left(t - \frac{z}{u_s} \varepsilon \right)} = \frac{k_i C_i^f d_{p,r} q_r^e}{k_r C_r^f d_{p,i} q_i^e} \quad (\text{C.25})$$

Inserting Equations (C.24) and (C.25) into Equation (C.21),

$$\frac{\partial x_i}{\partial \xi_r} \left(\frac{k_r d_{p,i}}{k_i d_{p,r}} \right) + (\text{FR}) \frac{\partial y_i}{\partial \tau_r} \left(\frac{k_r C_r^f d_{p,i} q_i^e}{k_i C_i^f d_{p,r} q_r^e} \right) = 0 \quad (\text{C.26})$$

$$\frac{\partial x_i}{\partial \xi_r} + (\text{FR}) \frac{C_r^f q_i^e}{C_i^f q_r^e} \frac{\partial y_i}{\partial \tau_r} = 0 \quad (\text{C.27})$$

The constant $\frac{C_r^f q_i^e}{C_i^f q_r^e}$ is encountered frequently, for brevity it is assigned to the

constant array α_i .

$$\alpha = \frac{C_r^f q_i^e}{C_i^f q_r^e} \quad (\text{C.28})$$

The column material balance is then written for an arbitrary constituent 'i,'

$$\frac{\partial x_i}{\partial \xi_r} = -(\text{FR}) \alpha \frac{\partial y_i}{\partial \tau_r} = R_i^T \quad (\text{C.29})$$

The differential equation system has been defined, but an expression relating the ionic fluxes to R_i^T . From the base assumption that the mass flow rate per unit area of a constituent is equal to the sum of its ionic species fluxes plus the molecular flux, the constituent flux is defined below.

$$J_i^T = \sum_{k=1}^m J_{ik} + J_i^* \quad (C.30)$$

The constituent flux is incorporated into the column material balance by relating the change in constituent capacity with respect to time to the product of the constituent flux and the specific surface area.

$$\frac{dq_i^T}{dt} = -J_i^T a_s \quad (C.31)$$

The variable a_s is the specific surface area per unit volume. For spherical particles in film diffusion, only the external surface area of the sphere is considered.

$$a_s d_{p,i} = \left(\frac{4\pi r^2}{\frac{4}{3}\pi r^3} \right) (2r) = 6 \quad (C.32)$$

The change in loading ratio with respect to time is found by dividing Equation (C.31) by q_i^e , and substituting Equation (C.32).

$$\frac{dy_i}{dt} = \frac{-6J_i^T}{q_i^e d_{p,i}} \quad (C.33)$$

In order to include the particle rate into the column material balance, the dt differential must be changed to a $\partial\tau_r$ differential by successive applications of the chain rule.

$$\frac{\partial y_i}{\partial \tau_r} = \frac{\partial y_i}{\partial t} \frac{\partial t}{\partial \tau_i} \frac{\partial \tau_i}{\partial \tau_r} \quad (\text{C.34})$$

Substituting Equations (C.12) and (C.25) into Equation (C.34),

$$\frac{\partial y_i}{\partial \tau_r} = \left(\frac{-6J_i^T}{q_i^e d_{p,i}} \right) \left(\frac{d_{p,i} q_i^e}{k_i C_i^f} \right) \left(\frac{k_i C_i^f d_{p,r} q_r^e}{k_r C_r^f d_{p,i} q_i^e} \right) \quad (\text{C.35})$$

and reducing yields the change in the constituent loading ratio with respect to time.

$$\frac{\partial y_i}{\partial \tau_r} = -\frac{6J_i^T}{C_i^f k_i} \left(\frac{d_{pr} q_r^e k_i}{d_{pi} q_i^e k_r} \right) \quad (\text{C.36})$$

The loading profiles are changed by relating the differential $\partial y_i / \partial \tau_r$ and R_i^T to the loading profile Y_i . Note y_i is the ratio of species ‘i’ capacity to its equilibrium capacity, while Y_i is the fraction of the total capacity. These quantities are related according to Equation (C.37).

$$Y_i = y_i \frac{q_i^e}{Q_i} = y_i Y_i^e \quad (\text{C.37})$$

Differentiating Equation (C.37) with respect to y_i yields

$$\frac{dY_i}{dy_i} = Y_i^e \quad (\text{C.38})$$

The differential is then used in the chain rule to relate the total rate to the change in resin equivalent fraction, as shown in Equation (C.39).

$$\frac{dY_i}{d\tau_r} = \frac{1}{\alpha} \frac{dy_i}{d\tau_r} \frac{dY_i}{dy_i} = Y_i^e \frac{C_i^f}{q_i^e} \frac{q_r^e}{C_r^f} R_i^T \quad (\text{C.39})$$

The author notes that in spite of the large number of equations used to derive these expressions, Equations (C.29) and (C.39) are the equations applied in the model for

the change in solution ratio with respect to distance and the resin fraction with respect to time.

APPENDIX D

APPROXIMATION OF TWO-BED APPROXIMATION OF AN UNEVEN RESIN BED

Calculation procedure for Surry column:

Flow rate is assumed to be proportional to average velocity times crossing area.

The original bed is spitted to two beds with same total volume.

(1). Dimension:

Given Bed 1 diameter half that of the original bed, 8 ft. And Bed 1 is 16 inches higher than Bed 2.

$$V_1 + V_2 = V_{\text{total}} \text{ OR}$$

$$\pi 2^2 (h + 1.33) + \pi (4^2 - 2^2) h = \pi 4^2 4$$

$$\text{Solve } h = 3.667 \text{ ft}$$

Bed 2:

$$\pi (4^2 - 2^2) h = \pi r^2 h \quad r = 3.46 \text{ ft}$$

The dimensions are summarized in below table

| Column | bed depth (ft) | bed diameter (ft) |
|--------|----------------|-------------------|
| 1 | 5 | 4 |
| 2 | 3.667 | 6.92 |

(2). Flow rate calculation: Use the Ergun equation:

$$\frac{\Delta p}{L} = \frac{150V_0\mu(1-\varepsilon)^2}{g_c\Phi_s^2D_p^2\varepsilon^3} + \frac{1.75V_0\rho(1-\varepsilon)}{g_c\Phi_sD_p\varepsilon^3}$$

$\Delta p : 50\text{psi}$

$\mu : 0.001\text{N.s/m}$

$g_c : 9.8 \quad D_p : 0.0006$

$\Phi_s : 1 \text{ (sphericity)} \quad \varepsilon : 0.35$

Solve V_0 in Mathcad

$V_{01}=0.156 \text{ m/s}; V_{02}=0.189 \text{ m/s}$

APPENDIX E

FLUX EXPRESSIONS AND PARTICLE RATE

Flux expressions for ions in multicomponent ion exchange are usually derived using Nernst-Planck model and basic principles of ion exchange. Haub and Foutch (1984), Zecchini and Foutch (1990) had successfully applied Nernst-Planck model to describe film diffusion-controlled mixed-bed ion exchange fluxes for monovalent ions (binary or ternary systems). In addition, Pondugula (1994) further developed the flux expressions for divalent systems. But to handle multicomponent multivalent MBIE systems, generalized expression is required. In this work, the method proposed by Franzreb et al. (1993) is used to derive the flux expressions for multicomponent, multivalent systems.

If neglecting the curvature of film, the Nernst-Planck equation can be expressed as

$$J_i = -D_i \left[\frac{\partial C_i}{\partial r} + \frac{C_i z_i F}{RT} \frac{\partial \phi}{\partial r} \right] \quad (\text{E.1})$$

where ϕ is the electric potential and z_i is the ion valence. Assuming pseudo steady state allows us to replace the partial derivatives by ordinary derivatives. The flux expressions derived in this model are based on bulk-phase neutralization.

The conditions that must be satisfied within the film surrounding the resin are:

$$\sum z_i C_i = \sum z_j C_j \quad (\text{Electroneutrality, charge balance}) \quad (\text{E.2})$$

where 'i' stands for counterions and 'j' represents coions.

$$z_j J_j = 0 \quad (\text{No coion flux}) \quad (\text{E.3})$$

$$\sum z_i J_i = \sum z_j J_j \quad (\text{No net current flow}) \quad (\text{E.4})$$

From Eq (E.3) and Eq (E.4)

$$\sum z_i J_i = 0 \quad (\text{No net current flow}) \quad (\text{E.5})$$

The total equivalent ion concentration can be defined as:

$$C_T = \omega \sum_{i=1}^n z_i C_i = \omega_j \sum_{j=1}^m z_j C_j \quad (\text{E.6})$$

where, n is the number of counterions, m is the number of coions. And $\omega = +1$ for cations and -1 for anions.

Using the no coion flux condition – Eq (E.3),

$$\frac{d\phi}{dr} = -\frac{RT}{F} \frac{z_j \frac{dC_j}{dr}}{z_j^2 C_j} \quad (\text{E.7})$$

From the no coion flux condition we have that the sum of the coion fluxes in the film is also zero. Now the electric potential term in the Nernst-Planck equation can be eliminated in terms of the total equivalent concentration as:

$$\frac{d\phi}{dr} = -\frac{RT}{F} \frac{\sum_{j=1}^m z_j \frac{dC_j}{dr}}{\sum_{j=1}^m z_j^2 C_j} \quad (\text{E.8})$$

Introducing a mean coion valence defined as

$$z_Y = \frac{\sum_{j=1}^m z_j^2 C_j}{\sum_{j=1}^m z_j C_j} \quad (\text{E.9})$$

and combining with the definition for total concentration – Eq (E.6), the Eq (E.8) can be reduced to

$$\frac{d\phi}{dr} = \frac{-RT}{z_Y F} \frac{1}{C_T} \frac{dC_T}{dr} \quad (\text{E.10})$$

Now the Nernst-Planck expression for counterions can be written as:

$$J_i = -D_i \left(\frac{dC_i}{dr} - \frac{C_i z_i}{C_T z_Y} \frac{dC_T}{dr} \right) \quad (\text{E.11})$$

Applying the no net current flow condition - Eq (E.5) to Eq (E.11),

$$\sum_{i=1}^n z_i D_i \frac{dC_i}{dr} + \sum_{i=1}^n z_i D_i N_i \frac{C_i}{C_T} \frac{dC_T}{dr} = 0 \quad (\text{E.12})$$

where, $N_i = -\frac{z_i}{z_Y}$. (E.13)

For monovalent system of ions or equal valence system of ions, the above equation could be easily integrated to obtain a relation between C_i and C_T . This is not possible in the case of arbitrary valences. At this point the method proposed by Franzreb (1993) is used to proceed further. In this method, Eq (E.11) is differentiated to eliminate the unknown J_i . This leads to a homogeneous second order differential equation:

$$\frac{d^2 C_i}{dr^2} + \frac{N_i}{C_T} \frac{dC_i}{dr} \frac{dC_T}{dr} + N_i \frac{C_i}{C_T} \left(\frac{d^2 C_T}{dr^2} - \frac{1}{C_T} \left(\frac{dC_T}{dr} \right)^2 \right) = 0 \quad (\text{E.14})$$

This method leads to an exact solution for the case of equal valences and only an approximation for the case of arbitrary valences. For counterions of equal valences, summation of Eq (E.14) for all the ions leads to

$$\sum_{i=1}^n \frac{d^2 C_i}{dr^2} + \frac{1}{C_T} \frac{dC_T}{dr} \sum_{i=1}^n N_i \frac{dC_i}{dr} + \frac{1}{C_T} \frac{d^2 C_T}{dr^2} \sum_{i=1}^n N_i C_i - \frac{1}{C_T^2} \left(\frac{dC_T}{dr} \right)^2 \sum_{i=1}^n N_i C_i = 0 \quad (\text{E.15})$$

Substituting Eq (E.6) and its derivatives in the above leads to

$$\frac{d^2 C_T}{dr^2} = 0 \quad (\text{E.16})$$

From the above equation it can be understood that for the case of counterions of equal valences, the profile of the total concentration in the film is linear. Zecchini and Foutch (1990) arrived at the same conclusion in their model for univalent ternary ions. The above equation combined with Eq (E.6) can be used to obtain relationships between the derivatives of C_i and C_T . Substitution of all these derivatives in Eq (E.15) leads to

$$\frac{d^2 C_i}{dC_T^2} + \frac{N_i}{C_T} \frac{dC_i}{dC_T} - \frac{N_i C_i}{C_T^2} = 0 \quad (\text{E.17})$$

This is the Euler's differential equation the solution of which is

$$z_i C_i = A_i C_T + B_i C_T^{-P} \quad (\text{E.18})$$

For the case of equal valences, we have $P = N_i$. Using the boundary conditions

$$r = 0, C_T = C_T^* \quad (\text{E.19})$$

$$r = \delta, C_T = C_T^o \quad (\text{E.20})$$

the values of the parameters A_i and B_i can be determined as follows:

$$A_i = \frac{1}{C_T^0} \left(z_i C_i^0 - B_i (C_T^0)^{-P} \right) \quad (\text{E.21})$$

and

$$B_i = \omega \frac{X_i^* - X_i^0}{(C_T^*)^{-P-1} - (C_T^0)^{-P-1}} \quad (\text{E.22})$$

Eq (E.18) gives us a relation between the individual ion concentrations, C_i and the total equivalent concentration, C_T . Substituting for C_i and its derivative in the modified Nernst-Planck Equation (E.11), we get the following flux expression:

$$J_i = -\frac{D_i}{z_i} \frac{dC_T}{dr} \left[\left(A_i - P B_i C_T^{-P-1} \right) + N_i \left(A_i + B_i C_T^{-P-1} \right) \right] \quad (\text{E.23})$$

For the case of arbitrary valences, Eq (E.18) is only an approximation. In this case however, N_i is not the same for all the counterions and hence, P cannot be equal to N_i . Combining the above equation with the condition of no net current flow (E.5) results in

$$\left(\sum_{i=1}^n D_i A_i + \sum_{i=1}^n N_i D_i A_i \right) + \left(\sum_{i=1}^n N_i D_i B_i - P \sum_{i=1}^n D_i B_i \right) C_T^{-P-1} = 0 \quad (\text{E.24})$$

The only way the above equation can hold true is when both the terms are equal to zero. That leads to

$$\sum_{i=1}^n (1 + N_i) D_i A_i = 0 \quad (\text{E.25})$$

Substitution of A_i Eq (E.21) into the above and with some mathematical manipulations give the desired expression for total interfacial concentration, C_T^* :

$$C_T^* = \left(\frac{\sum_{i=1}^n (1 + N_i) D_i X_i^0}{\sum_{i=1}^n (1 + N_i) D_i X_i^*} \right)^{1/P+1} C_T^b \quad (\text{E.26})$$

Equating the second parentheses term to zero and substitution of B_i would give us the expression for the exponent P as:

$$P = \frac{\sum_{i=1}^n N_i D_i (X_i^* - X_i^0)}{\sum_{i=1}^n D_i (X_i^* - X_i^0)} \quad (\text{E.27})$$

In an equal valance case, P is equal to N_i and in an arbitrary case, it would be in the neighborhood of N_i . The concentrations involved in this work are very low and lead to lot of numerical errors and instability. Because of numerical discrepancies, sometimes the value of P computed in the code is unusually high and leads to problems in further computations. Hence the expression for P (Eq E.27) is modified as follows:

$$P = \frac{\sum_{i=1}^n N_i D_i |X_i^* - X_i^0|}{\sum_{i=1}^n D_i |X_i^* - X_i^0|} \quad (\text{E.28})$$

Once again, substituting the above equations into Eq (E.11) and integrating between the boundary conditions given earlier, we would get the final desired form of the ionic flux expression:

$$J_i = \frac{D_i}{\delta} \left(\left(1 - \frac{N_i}{P}\right) (C_i^* - C_i^b) + N_i A_i \left(1 + \frac{1}{P}\right) (C_T^* - C_T^b) \right) \quad (\text{E.29})$$

Particle Rates

The rate of exchange is related to the flux of the species by

$$\frac{dq_i}{dt} = -J_i a_s \quad (\text{E.30})$$

The resin phase concentration q_i can be represented as:

$$q_i = y_i Q \quad (\text{E.31})$$

Now Eq can be written as

$$\frac{dy_i}{dt} = \frac{-J_i a_s}{Q} \quad (\text{E.32})$$

The rate of ion loadings in to the resin can be determined using the above equation once the individual ionic fluxes are known.

The effective diffusivity is defined as:

$$D_e = \frac{\sum_{i=1}^n |J_i \delta|}{\sum_{i=1}^n |C_i^* - C_i^o|} \quad (\text{E.33})$$

The film thickness in Eq (E.28) is eliminated using the relation

$$\delta = D_e / K \quad (\text{E.34})$$

where K is a mass transfer coefficient found from Dwivedi and Upadhyay's correlation (1979)

$$K = \frac{D_i}{d_p} Sc^{1/3} Re \left[\frac{0.765}{(\epsilon Re)^{0.82}} + \frac{0.365}{(\epsilon Re)^{0.386}} \right] \quad (\text{E.35})$$

In the above Equation, D_i is the diffusivity of ion 'i', d_p is the particle diameter, Re is Reynolds number, Sc is Schmidt number and ϵ is void fraction.

Schmidt number (Sc) is defined using the effective diffusivity as

$$Sc = \frac{\mu}{\rho D_e} \quad (E.36)$$

Substituting Eq (E.32) in the flux expression Eq. (E.29), we get

$$\frac{J_i}{K} = \frac{D_i}{D_e} \left(\left(1 - \frac{N_i}{P}\right)(C_i^* - C_i^b) + N_i A_i \left(1 + \frac{1}{P}\right)(C_T^* - C_T^b) \right) \quad (E.37)$$

This J_i/K is computed for each of the ions in the subroutines and returned to the main program in the computer code developed for this model.

Flux expressions for non-ionic species

The fluxes of nonionic (molecular) form species are usually described by Fick's second law, that is

$$J_i^m = -D_i^m \frac{dC_i^m}{dz} \quad (E.38)$$

Integrating Eq (E.37) yields

$$J_i^m = \frac{D_i^m}{\delta} (C_i^{mb} - C_i^{m*}) = k_i^m (C_i^{mb} - C_i^{m*}) \quad (E.39)$$

where, $k_{Mol,i} = \frac{D_{Mol,i}}{\delta}$ is molecular mass transfer coefficient. Frequently in a

multicomponent system with dissociative species, the concentration of molecular form is much greater than that of ionic form, so that the effect of molecular concentration on the total mass transfer rate has to be taken into account (Jansen, 1996b). To account for this effect, an enhancement factor is introduced in this work to determine the flux for the nonionic form species, that is

$$\alpha = \text{Log} \left(\frac{D_{\text{Mol}} C_{\text{Mol}}}{D_{\text{Ion}} C_{\text{Ion}}} \right) \quad (\text{E.40})$$

where D_{Mol} and C_{Mol} are the diffusivity and concentration of the molecular form, and D_{Ion} and C_{Ion} are the diffusivity and concentration of the ionic form.

Therefore, the flux for the nonionic (molecular) form of weak electrolyte is

$$J_i^m = (1 + \alpha) \frac{D_i^m}{\delta} (C_i^{\text{mb}} - C_i^{\text{m}*}) \quad (\text{E.41})$$

As soon as the flux of nonionic form is determined by Eq (E.41), the mass transfer rate for the nonionic form can be calculated using Eq (E.30).

VITA 

Yi Jia

Candidate for the Degree of

Doctor of Philosophy

Thesis: DEVELOPMENT OF A TRUE MULTICOMPONENT FILM DIFFUSION
CONTROLLED MIXED-BED ION-EXCHANGE MODEL AND EXPANDED
TO INCLUDE RADIOACTIVE ISOTOPES

Major Field: Chemical Engineering

Biographical:

Personal Data: Born in Yangquan, Shanxi, China in Sept 12, 1975

Education: Graduated from Yangquan Kuangwuju First High School, Shanxi, China in 1993; received Bachelor of Science degree in Chemical Engineering from Tsinghua University, Beijing, China in 1998; completed the requirements for the Doctor of Philosophy degree with a major in Chemical Engineering at Oklahoma State University in December 2004.

Professional Experience: Employed by Institute of Process Engineering, Chinese Academy of Sciences as a research assistant, 1998 to 2000; employed by Oklahoma State University, School of Chemical Engineering as a research and teaching assistant, 2000 to 2004.